INFLUENCE OF DISLOCATIONS AND SECOND PHASES ON THE MAGNETOSTRICTIVE BEHAVIOR OF IRON-GALLIUM AND OTHER IRON ALLOY SINGLE CRYSTALS

by

Biswadeep Saha

A dissertation submitted to the faculty of
The University of Utah
in partial fulfillment of the requirements for the degree of

Doctor of Philosophy

Department of Metallurgical Engineering

The University of Utah

August 2012

The University of Utah Graduate School

STATEMENT OF DISSERTATION APPROVAL

The following faculty members served as the supervisory committee chair and members for the dissertation of Biswadeep Saha. Dates at right indicate the members' approval of the dissertation.

Sivaraman Guruswamy, Chair	04/06/2012 Date Approved
Michael K. McCarter, Member	04/06/2012 Date Approved
Raj K. Rajamani, Member	04/06/2012 Date Approved
Zhigang Z. Fang, Member	04/06/2012 Date Approved
Michael S. Moats, Member	04/06/2012 Date Approved

The dissertation has also been approved by Jan D. Miller

Chair of the Department/School/College of Metallurgical Engineering

and by Charles A. Wight, Dean of The Graduate School.

ABSTRACT

Rare-earth-free Fe-Ga magnetostrictive alloys exhibit an excellent combination of large low-field magnetostriction, strength, ductility, wide operating temperature range, and low cost. Various observations in these and other α-Fe-based magnetostrictive alloys suggest that lattice strain modulations that are influenced by solute elements, near neighbor atomic environments around Fe atoms, coherent and incoherent precipitates, and structural defects such as dislocations likely play an important role in their magnetostrictive behavior.

In the first part, the effect of dislocations on the magnetostriction of Fe-Ga single crystals was examined. The [001]- and [126]-oriented Fe-20 at.% Ga single crystal samples were deformed in a controlled way to introduce dislocation arrays with two different array geometries. Magnetostriction values showed a much lower decrease after deformation for the case of a [001]-oriented crystal, where eight different slip systems were operative and consequently eight different sets of dislocation arrays are expected. A drastic drop in magnetostriction measured along the sample axis is observed in the sample subjected to a small strain by deformation of a [126]-oriented crystal during which slip occurred on only one slip system. The nature of strain modulation introduced in this case was spatially asymmetric. The [126] deformation was accompanied by an acoustic emission during the formation of slip band.

Transmission electron microscopy was carried out to examine the nature of dislocation distribution. The results show that the nature of strain modulation introduced by the dislocation arrays has a strong influence on the magnetostrictive behavior of magnetostrictive alloys.

In the second part of this research, the effect of Mo addition to Fe was examined in detail. Addition of Mo to Fe increased the magnetostriction $(3/2)\lambda_{100}$ Fe very rapidly to 137 ppm at 10 at.% Mo, the highest value observed in these alloys. Further Mo additions decreased the magnetostriction. Magnetization data show a drastic drop in magnetization to 63 emu/gm for Fe-20 at.% Mo from 176 emu/gm for Fe-10 at.% Mo suggesting the formation large amounts of nonmagnetic second phase and reduction in total Fe content of the alloy. The drop in magnetostriction at higher Mo contents is associated with the formation of a second phase.

To my parents Binoy Kumar Saha and Chhanda Saha

TABLE OF CONTENTS

LIST OF TABLES

LIST OF FIGURES

ACKNOWLEDGEMENTS

I would like to express my sincere gratitude to my advisor Professor Sivaraman Guruswamy for his guidance, support and encouragement throughout the research period. I am grateful to him for giving me the opportunity to work in his very dynamic research group. This is a great opportunity for me to work with him and learn not only about magnetism and experimental methods but also broaden my research vision. I would also like to thank my supervisory committee, Professor Michael K. McCarter, Professor Raj K. Rajamani, Professor Zhigang Z. Fang, and Associate Professor Michael S. Moats, for their valuable time and advice.

I would like to thank my Lab mates Chai Ren, Meenakshisundaram Ramanathan and Gavin Garside for their active support. I am also thankful to Mrs. Karen Haynes, Mrs. Kay Argyle, and Mrs. Evelyn Wells for their help in my general work.

I gratefully acknowledge the financial support for this work to the National Science Foundation under DMR Award 0854166.

The electron microscopy was accomplished at the Electron Microscopy Center for Materials Research at the Argonne National Laboratory a U.S. Department of Energy, Office of Science Laboratory operated under Contract No DE – AC02_06CH11357 by University of Chicago, Argonne, LLC.

Finally I express my gratitude to my parents Binoy Kumar Saha and Chhanda Saha, my brother and his family Biswarup, Mithu and Bidita, and sister Jayeeta and her family for their love, support and encouragement through these years of study abroad.

CHAPTER 1

INTRODUCTION

Magnetostrictive materials exhibit reversible strains and changes in elastic properties in the presence of an applied magnetic field or the reciprocal effect of changes in the magnetic properties with the application of stress [1]. The discovery of large enhancement in low-field magnetostriction in Fe with the addition of Ga to Fe and good mechanical properties (high strength, good ductility, and high elastic modulus) that are superior to those observed in the brittle Terfenol-D and Ni_2MnGa intermetallic alloys make these alloys very attractive in a wide range of actuator, sensor and active device applications [2-3]. This discovery opened up the possibility of obtaining larger low-field magnetostriction values in other low-cost ductile non-rare-earth containing α-Fe phase based alloys with alloying additives that are less expensive than rare-earths such as Tb and Dy.

Ordering, second phases and defects can influence the magnetostrictive behavior in Fe-Ga and other Fe-based magnetostrictive alloys [4-17]. Studies in Fe-Ga and other α-Fe-based magnetostrictive alloys such as Fe-Mo and Fe-W alloys [10-16] show that extensive drops in magnetostriction for certain compositions and thermal histories are associated with the presence of a two phase structure consisting of long-range ordered phase regions and the disordered bcc phase regions. The coherency strains in

this two-phase structure modulate the local atomic spacing and this could be origin of the strong influence on magnetostriction as the magnetoelastic coupling in the lattice strongly depends on the interatomic spacing. These observations suggest that strain modulations arising from (i) local atomic environment described by the near-neighbor distances and the co-ordination number and type of neighboring atoms and species, and (ii) coherent- and incoherent- second phases and other structural imperfections likely play a large role in determining magnetostriction.

Dislocation is a major structural imperfection in materials. Dislocations introduce an asymmetric strain distribution and its magnitude decreases rapidly with distance from the dislocation core [18-19]. The strain fields of the dislocations can have a direct influence on the magnetostriction as well as an indirect effect through the interaction of the strain field with the solute atoms [18]. Substitutional solute elements tend to introduce more spherically symmetric strains whereas interstitial solutes, dislocations, short range ordering and clustering, and coherent precipitates could introduce asymmetric local strains in the lattice in which they are present. In this work the influence of well-defined dislocation arrays on magnetostriction in a single crystal bcc Fe based solid solution phase has been examined.

The dislocation type and spatial distributions will differ as a function of deformation strain level and crystal orientation. In this work, the influence of strain modulations arising from dislocations introduced through controlled deformation on magnetostriction in [001]- and [126]-oriented Fe-20% Ga alloy single crystals has been examined. Fe-20 at.% Ga shows the highest magnetostriction among all other known α-Fe based alloys and it has less propensity of forming second phases during cooling from

high temperature. For these reasons, this alloy is chosen for the deformation study. The [126] crystal is oriented such that a single slip system $(101)[\bar{1}\,1\,1]$ will operate during the initial plastic deformation along the long axis of the crystal that is parallel to the [126] direction. Dislocations in the array formed will have Burgers vectors of the type ½<111> and move on {110} planes. While a [123] orientation will allow a maximum possible plastic deformation by single slip, [126]-orientation was chosen due to limitation on the size of the single crystals that could be grown. In [001]-oriented crystals, eight different slip systems will be operational during initial deformation and eight distinct dislocation arrays will be present after the crystal deformation. Dislocations will have Burgers vector of the ½<111> type and they are expected to operate on {110}<111> slip systems [18]. Magnetostrictive behavior of plastically deformed [001]- and [126]-oriented Fe-20 at.% Ga single crystals are compared. Acoustic emission measurements were also carried out during plastic deformation. TEM examinations of annealed and deformed single crystals were carried out to examine the nature of dislocation arrays formed.

Until this time, there is no accepted theory on why the addition of Ga increases the magnetostriction of Fe dramatically. Fundamental understanding of magnetostriction in Fe and the influence of alloying elements on magnetostriction in Fe is essential for future development of new low cost rare earth free α-Fe based magnetostrictive alloys. In recent years, the study on magnetostriction of Fe-based alloys with alloying additions having various ground state electronic configurations has been initiated [10-11, 20-21]. Thuanboon et al. [10] examined the influence of the addition of elements W and Mo with half-filled d-shell in the ground state electronic

configuration to Fe. Both W and Mo additions to Fe were found to significantly enhance the magnetostriction and magnetoelastic coupling constants. Addition of W to Fe was found to increase the magnetostriction of Fe very rapidly until 4.4 at.% W and then the rate of increase with W addition is much slower [13]. The slow increase above 4.4 at.% is related to the increased propensity of forming second phase regions on cooling in these alloys. Magnetization measurements on the Fe-W alloys showed that the addition of W to Fe decreases magnetization more rapidly than that observed in Fe-Ga alloys. This also indicates the presence of large amounts of nonmagnetic second phase in Fe-W alloys [1, 22-23]. This study also showed that Fe-15 at.% Mo [001]-oriented annealed single crystal sample shows the highest magnetostriction value of 123 x 10^{-6}, which is a six times increase in the magnetostriction of Fe. Fe-17.5 at.% Mo shows a much lower magnetostriction as compared to the Fe-15 at.% Mo. This behavior arises from the higher propensity for the formation of second phase in higher Mo content alloys as Mo has much less solubility (<3 at.%) in Fe at room temperature. This study of magnetostriction in Fe-Mo system was limited to two compositions and to measurements of only (3/2) λ_{100}. Mo is more abundant and less expensive than Ga, and identification of Fe-Mo alloys with high magnetostriction can have a greater impact in the future. In this study, a more detailed examination of Fe-Mo alloys was therefore carried out to study the effect of solute content and second phase on magnetostriction. Single crystals of Fe-Mo alloys with varying Mo contents were grown and their magnetic and magnetostriction behaviors were examined in detail.

In summary, this work will therefore examine (i) magnetostriction observed in Fe-20 at.% Ga [001]- and [126]-oriented single crystal before and after plastic

deformation and (ii) the influence of Mo addition to Fe on the magnetostriction. The work carried out involved crystal growth, crystal orientation, oriented sample preparation for deformation and magnetostriction studies, deformation of sample, acoustic signal collection during deformation, magnetization measurements using vibrating sample magnetometry, and magnetostriction measurements.

CHAPTER 2

BACKGROUND

This chapter will present definitions or descriptions of various terms used in magnetism and magnetostriction that are relevant to the current work, and a background literature survey on the developments in Fe-Ga and Fe-Mo magnetostrictive alloys, and identify the issues that the current work intends to address.

2.1 Magnetism

The classical theory of electromagnetism states that due to the rotation of negatively charged electrons around the nucleus, a magnetic field is produced, and it changes their motion in response to an external magnetic field. Electron orbiting around the nucleus has a magnetic dipole moment associated with it. Imbalances in the orbital magnetic moments produce a net magnetic moment for the atom [1, 24].

2.1.1 Magnetic Poles and Magnetic Field

In a bar magnet, the regions near the ends appear to be the locations from where magnetic forces originate. The end of a freely moving bar magnet that approximately points towards the geographic North Pole of the earth is called the north-seeking pole or north pole and the other end which approximately points towards the South Pole of the

earth is called south-seeking pole or south pole. Similar poles repel each other and opposite poles attract each other. The force, F between two poles having pole strength p_1 and p_2 is proportional to their pole strengths and inversely proportional to the square of the distance, d, between them. This force F can be expressed by the equation

$$F = k \frac{p_1 \ p_2}{d^2} \tag{2.1}$$

A magnetic pole creates a magnetic field around it, and this field produces a force on the nearby second pole. The force produced by the pole is directly proportional to the product of pole strength, p and the intensity of field or field strength, H. This relationship is expressed by the equation

$$F = k \ p \ H \tag{2.2}$$

Due to the capability to magnetize other magnetic materials, this field strength, *H,* is also called as the magnetizing force. Equations 2.1 and 2.2 combine to give the equation

$$H = \frac{p}{d^2} \tag{2.3}$$

Moving electrons and ions can produce a magnetic field. The magnetic field generated by a steady current *I* is described by the Biot–Savart law as described by the equation 2.4 [24].

$$dB = k_m \frac{I \; dS \; \hat{r}}{d^2} \tag{2.4}$$

where dS is the element of cross-section of the conductor, $\hat{r}$ is unit vector in the direction of r and k_m is a constant.

In the case of a solenoid, the field along its axis at the midpoint is given by the equation [1].

$$H = \frac{4 \; \pi \; n \; i}{10 \; L} \tag{2.5}$$

where H is in Oe, n is the number of turns, L is the length in units of cm and i is the current in amperes.

When a piece of ferromagnetic material is placed in an applied magnetic field H, the material will be magnetized with an intensity of magnetization M and $4\pi M$ lines will be added to the applied field, H. This results in a magnetic induction, B, expressed by the equation

$$B = H + 4 \; \pi \; M \tag{2.6}$$

2.1.2 Magnetic Moment

A bar magnet having pole strengths $+p$ and $-p$ separated by a constant distance l is placed at an angle θ to a uniform applied magnetic field, H. This magnet will be subjected to a torque and this torque will try to line up the bar magnet parallel to the field direction. A schematic of this action is shown in Figure 2.1.

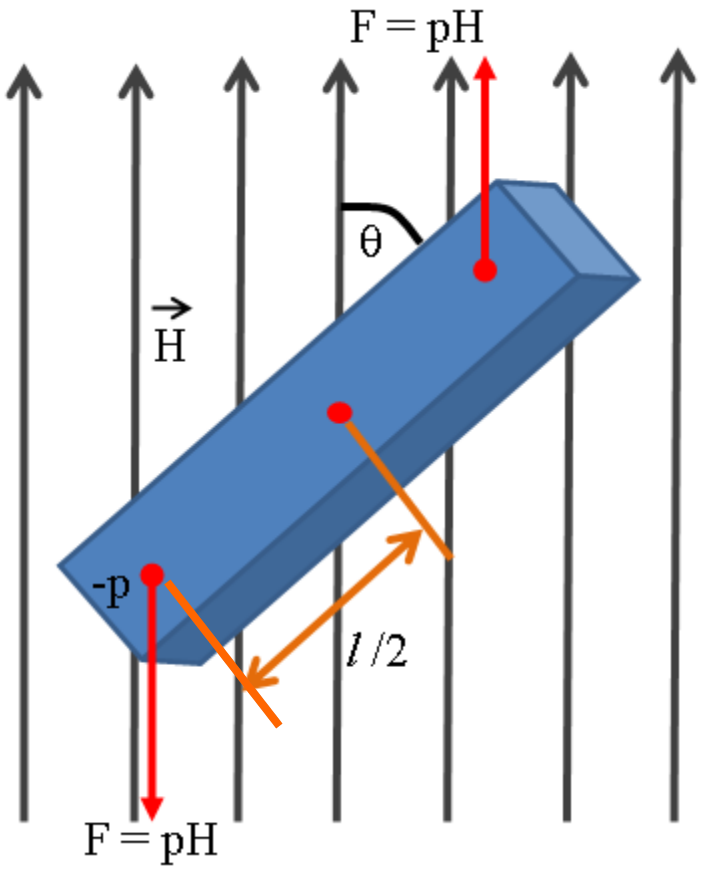

Figure 2.1 A bar magnet in a uniform field for calculating the moment.

The magnitude of the torque on the magnet is given by the equation,

$$(p\ H\ sin\theta)\left(\frac{l}{2}\right) + (p\ H\ sin\theta)\left(\frac{l}{2}\right) = p\ H\ l\ sin\theta \qquad (2.7)$$

When H = 1 Oe and θ=900, the torque has a unique value equal to the product of pole strength and length of the magnet. This value is defined as the magnetic moment "m". This relationship is defined by the equation,

$$m = p\ l \qquad (2.8)$$

The torque on the bar magnet is given by the product of the magnetic moment $\vec{m}$ and field $\vec{H}$.

$$\tau = \vec{m} \times \vec{H} \qquad (2.9)$$

The magnet has a certain potential energy, $E_{p,}$ when the magnet is not aligned along the field direction. The potential energy, E_{p}, is the energy used to turn the bar through an angle θ against the field, and is given by the Equation 2.10 [1].

$$E_p = \int_{90^0}^{\theta} m\ H\ sin\theta\ d\theta$$

$$= -\ m\ H\ cos\theta \qquad (2.10)$$

2.1.3 Magnetization

Magnetization *M* of a material can be defined as the dipole moment, *m* per unit volume of the material. This is described by the equation,

$$M = \frac{m}{v} \tag{2.11}$$

where v is the volume of the material [1]. An alternative definition of magnetization, pole strength per unit area of cross section, can be obtained if all the magnetic moments of the dipoles present align themselves along the field direction (Equation 2.12) [1]

$$M = \frac{p\ l}{v} = \frac{p}{a} \tag{2.12}$$

where a is the cross-sectional area of the magnet normal to the field direction. It is sometimes more convenient to refer to the magnetization per unit mass (specific magnetization), σ rather than per unit volume (Equation 2.13) [1].

$$\sigma = \frac{m}{w} = \frac{m}{v\ \rho} = \frac{M}{\rho} \tag{2.13}$$

where *w* is the mass and ρ is the density of the material. *M* can be expressed in terms of emu/cm^3 and emu/g unit.

2.1.4 Domains and Hysteresis

Magnetic materials are composed of small regions called magnetic domains. In each magnetic domain, the magnetic moments of all the atoms are all oriented in a specific direction that is parallel to one of the easy magnetization directions in the crystal. On the application of an external magnetic field, H, the domain boundary (domain wall) motion followed by coherent and/or incoherent moment rotation processes lead to the rotation of the moments within the domain towards the applied magnetic field. When each grain becomes a single domain and moments are aligned parallel to the applied magnetic field, the magnetization reaches the saturation level, M_s. Generally, the removal of the external magnetic field does not reduce the magnetization to zero. In this case, M lags behind the applied field H and a hysteresis is produced. This residual magnetization is called remnant magnetization, M_r. A reverse field called as coercive field, H_{ci}, needs to be applied in a direction opposite to the previously applied magnetic field direction to bring the magnetization to zero. Further increase in filed in the opposite direction will lead to saturation magnetization - M_s in the opposite direction. A reversal of the above mentioned steps leads to a symmetric loop known as hysteresis loop as shown in Figure 2.2.

2.1.5 Magnetic Anisotropy

Magnetic anisotropy refers to the dependence of magnetic properties with direction in the sample. There are three main sources of magnetic anisotropy, namely: crystal structure (magnetocrystaline), crystal shape, and stress. In addition, magnetic anisotropy can also be induced by magnetic annealing, deformation, or irradiation. All

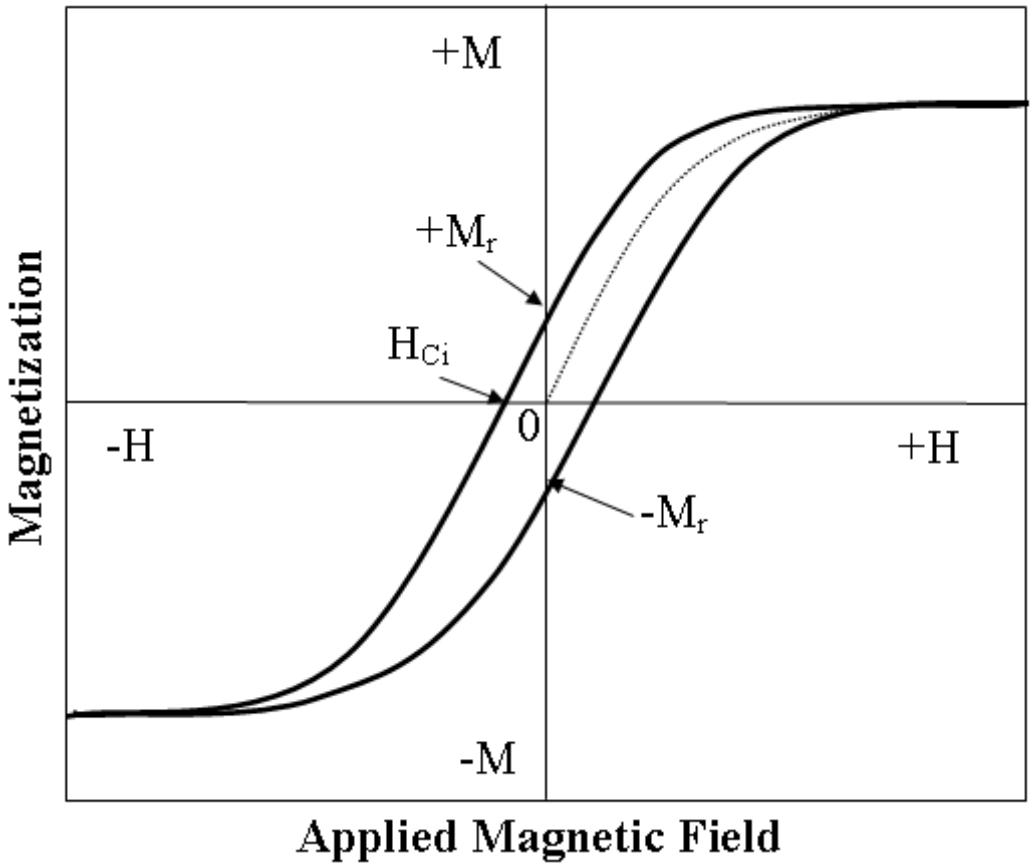

Figure 2.2 Schematic diagram of magnetization curve and hysteresis loop.

of these treatments introduce defect distributions that introduce anisotropic internal lattice strain. In this work, anisotropy in cubic crystal is of prime interest.

The saturation magnetization of iron can be achieved at a low field when the magnetic field is applied along one of the <100> directions. This direction is called the easy direction of magnetization. In the demagnetized state of a ferromagnetic material, spontaneous magnetization in the various domains is along one of these directions [1]. Magnetic materials like iron contain tens or hundreds of domains in a 1 cm^3 volume [1]. When a magnetic field is applied, the domains that have their magnetic moment direction close to the applied magnetic field direction will grow in volume by domain-wall motion as the magnetic potential energy of the crystal is lowered by this domain-wall motion. Crystal anisotropy field refers to a force that tends to align the magnetization of the domain to certain specific crystallographic direction in the crystal. The anisotropy force can be overcome by applying an external magnetic field that will turn the magnetization vector away from the easy direction. The associated stored energy is called the crystal anisotropy energy, E. For cubic materials this can be expressed as (Equation 2.14) [1]

$$E = K_0 + K_1\left(\alpha_1^2\alpha_2^2 + \alpha_2^2\alpha_3^2 + \alpha_3^2\alpha_1^2\right) + K_2\left(\alpha_1^2\alpha_2^2\alpha_3^2\right) + \ldots. \quad (2.14)$$

where K_i's are the anisotropic constants of the material and α_i's are the direction cosines of field direction of the axis along which the magnetic moment is saturated with respect to the crystal axes. Higher powers are generally not needed and as K_2 is very small the terms involved with K_2 are also neglected. The first term K_0 is angle independent and is

generally ignored due to interest mainly in the change in energy when the M_s vector rotates from one direction to another. Easy magnetization moment rotation is possible in the systems where crystal anisotropy energy is small. For iron, $E_{100}<E_{110}<E_{111}$, and the easy direction is <100>.

2.1.6 Classification of Magnetic Materials

2.1.6.1 Diamagnetic Material

A diamagnetic is a substance that has no net magnetic moment in the absence of applied magnetic field and exhibits a small or very weak negative moment proportional to the applied field. The explanation of this behavior was given by French physicist Paul Langevin [1]. When an external field is applied, is applied on a orbit, the effective current associated with a single electron orbit is reduced and this produces a magnetic moment opposite to the applied magnetic field. This effect is summed over all the electrons in the atom, and the substance shows a weak magnetism that opposes the applied magnetic field. The susceptibility of the diamagnetic material is independent of temperature and has a negative value. This can be expressed by the equation 2.15 [1],

$$\chi = \frac{M}{H} \tag{2.15}$$

Diamagnetic contribution is present in all materials. In paramagnetic and ferromagnetic materials, a diamagnetic contribution to the total magnetic moment is present. But, it is small compared to the paramagnetic or ferromagnetic contribution. Copper, gold, bismuth and beryllium are the examples of diamagnetic materials.

2.1.6.2 Paramagnetic Material

Paramagnetic materials show a positive response to an applied magnetic field and this response is very weak in nature. This is a temperature dependent property and varies inversely with temperature. Susceptibility of the paramagnetic material can be expressed as (Equation 2.16) [1].

$$\chi = \frac{C}{T} \tag{2.16}$$

where C is the Curie constant per gram. This relationship is also known as Curie's Law. This behavior was explained by Langevin. He assumed that there is no interaction between moments associated with atoms and stated that paramagnetism occurs due to the fact that spin and orbital moments of electrons in the atom do not cancel out in the presence of a magnetic field. In the absence of an applied magnetic field, the random orientations of the atomic moments results in zero net magnetic moment. When a magnetic field is applied, the atomic moments deviate from the random distribution with a net magnetic moment in the direction to the applied magnetic field. Susceptibility of the material decreases with increasing temperature due to randomizing effect of thermal excitation [1]. As there are many paramagnetic materials that do not obey Curie's law, Weiss modified Langevin's theory by considering the interaction of the magnetic moments of the atoms. He expressed this phenomenon in terms of a fictitious internal field called molecular field (H_m) and this is proportional to the magnetization as shown in Equation 2.17 [1].

$$H_m = \gamma M \tag{2.17}$$

where γ is the molecular field constant. Total magnetic field acting on the materials is

$$H_t = H + H_m$$
$$H_t = H + \gamma M \tag{2.18}$$

where H with H_t in Equation 2.18 leads to the Curie-Weiss law. Curie-Weiss law is described below by the equation 2.19 [1].

$$\chi = \frac{M}{H} = \frac{C}{T - C\gamma} = \frac{C}{T - \theta} \tag{2.19}$$

where θ is a measure of the strength of the interaction. The parameter θ is proportional to the molecular field constant γ. If θ is positive, the susceptibility value will increase and the molecular field aids the applied magnetic field. This tends to make elementary magnetic moments parallel to one another. Molecular field opposes the applied magnetic field and decreases the susceptibility value when θ is negative.

2.1.6.3 Ferromagnetic Material

Ferromagnetic materials are attracted to the permanent magnet and can be permanent magnets themselves. Iron, nickel and cobalt come under this category. In a more scientific description, these materials exhibit long range ordering of their magnetic moments in absence of an external field. Susceptibility of these materials follows the

Curie–Weiss law above T_c and become paramagnetic above a temperature with a value of θ close to T_c. At temperatures above T_c, the thermal energy becomes dominant and overcoming the exchange interactions and the magnetic moments become disordered. Weiss stated that molecular field acts in ferromagnetic materials below Curie temperature, and that this field is so strong that it can magnetize the ferromagnetic material to saturation even in the absence of an applied field [1]. The material is then self-saturating, or "spontaneously magnetized." The magnetic moments are aligned parallel in small regions called domains. These domains are separated by domain walls. The saturation magnetization directions of each domain are such that, as a whole, the material has no magnetization. When a field is applied, the domains grow by domain wall migration, and in case of a single crystal, the multidomain structure converts to a single domain in the direction of the applied magnetic field.

2.1.6.4 Antiferromagnetic Material

Antiferromagnetic materials have a very small positive susceptibility at all temperatures and hence they are very weak magnets. The theory of antiferromagnetism was developed chiefly by Ne´el [1]. With a decrease in temperature, susceptibility increases and is a maximum at a critical temperature called the Ne´el temperature T_N, and then susceptibility decrease with decreasing temperature. Above T_N, these materials are paramagnetic and below T_N they are antiferromagnetic. Below T_N due to the negative exchange interaction between neighboring atoms, the atomic moments arrange themselves in an antiparallel way. That leads to net zero magnetization of the material.

In most of the cases, T_N lies far below room temperature. These materials also follow the Curie-Weiss law but with a negative value for θ as shown in Equation 2.20 [1].

$$\chi = \frac{C}{T-\theta} \tag{2.20}$$

2.1.6.5 Ferrimagnetic Material

Ferrimagnetic materials are like ferromagnetic materials and show spontaneous magnetization at room temperature. These materials have magnetically saturated domains and exhibit the phenomena of magnetic saturation and hysteresis. Above Curie temperature, they become paramagnetic and loose the order. The magnetic moments of these materials are aligned antiparallel but with different magnitude in each of the sublattices. The most important ferrimagnetic materials are certain double oxides of iron and another metal. They are called ferrites. Cubic ferrites are $MO.Fe_2O_3$, where M is a divalent metal ion, like Mn, Ni, Fe, Co, or Mg and hexagonal ferrites are $BaO.6\ Fe_2O_3$ and $SrO.6\ Fe_2O_3$.

2.2 Magnetostriction

Magnetostrictive materials exhibit reversible strains and changes in elastic properties in the presence of an applied magnetic field or the reciprocal effect of changes in the magnetic properties with the application of stress [1]. A linear change in length per unit length is called Joule magnetostriction and a volume change by equal expansion or contraction in all direction per unit volume is called volume magnetostriction. The energy required for volume magnetostriction is high and hence it

has less practical importance compared to Joule magnetostriction. Joule magnetostriction λ is given by the equation,

$$\lambda = \frac{\Delta l}{l} \tag{2.21}$$

where Δl is the change is length due to applied magnetic field l is the length of the material.

The source of magnetostrictive strain is magnetoelastic coupling, which is defined as the tendency of neighboring ions to shift their positions in response to the rotation of the magnetic moment, and the change in elastic energy associated with this specific rotation of the magnetic moment [15]. Saturation magnetostriction, λ_{Si} is referred as the magnetostriction measured at magnetic saturation. Figure 2.3 shows a schematic for Joule magnetostriction and magnetostriction curve.

The saturation magnetostriction values, λ_{Si}, in a cubic crystal are usually measured in the directions of <100> and <111>. The saturation magnetostriction in a direction "i" can be written in terms of λ_{100} and λ_{111} as shown in Equation 2.22 [1].

$$\begin{aligned}\lambda_{Si} = \left(\frac{3}{2}\right)\lambda_{100}\left(\alpha_1^2\alpha_2^2 + \alpha_2^2\alpha_3^2 + \alpha_3^2\alpha_1^2 - \frac{1}{3}\right) \\ + 3\,\lambda_{111}\left(\alpha_1\alpha_2\beta_1\beta_2 + \alpha_2\alpha_3\beta_2\beta_3 + \alpha_3\alpha_1\beta_3\beta_1\right)\end{aligned} \tag{2.22}$$

Here the α_i's are the cosines of angles between the magnetization and the three crystal axes and the β_i's are the cosines of the angles between direction of the relative

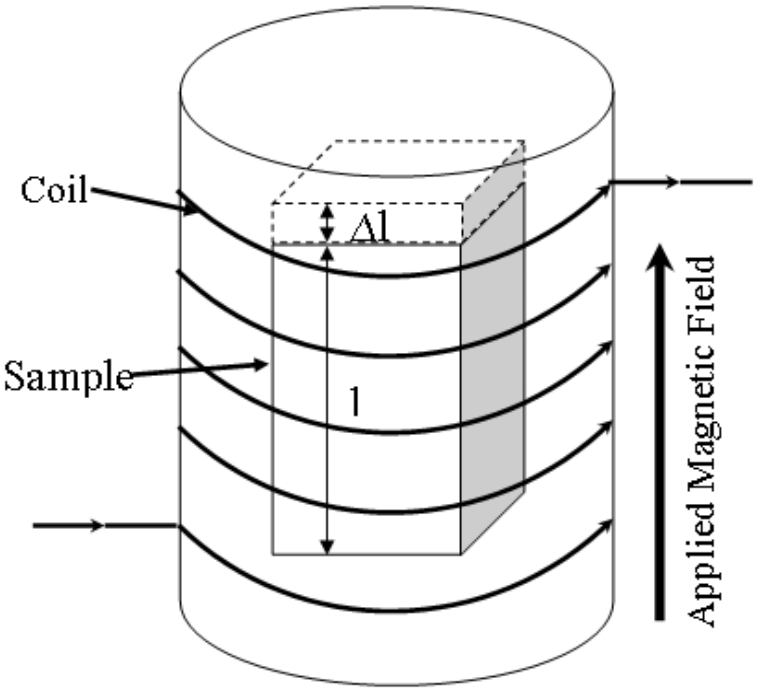

(a)

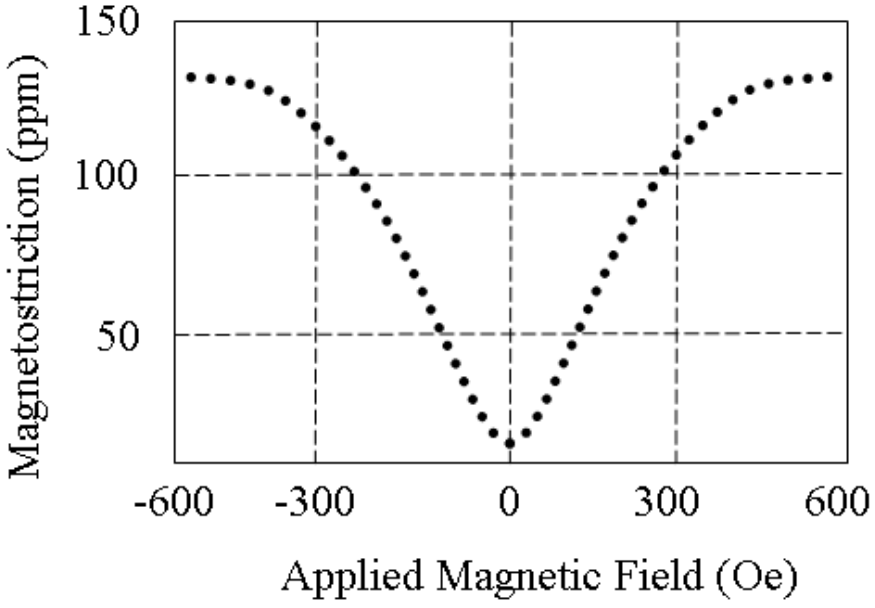

(b)

Figure 2.3 Schematic diagram for (a) Joule magnetostriction and (b) magnetostriction curve.

change the <100> and <111> crystal directions and these values are of length and the crystal axes. If the strain is measured in the same direction as the magnetization then, β_i = α_i and Equation 2.22 becomes

$$\lambda_{Si} = \left(\frac{3}{2}\right) \lambda_{100}\left(\alpha_1^4 + \alpha_2^4 + \alpha_3^4 - \frac{1}{3}\right) + 3\ \lambda_{111}\left(\alpha_1^2\alpha_2^2 + \alpha_2^2\alpha_3^2 + \alpha_3^2\alpha_1^2\right) \qquad (2.23)$$

Using the relationship among α_i as shown in Equation 2.24 [1].

$$\left(\alpha_1^2 + \alpha_2^2 + \alpha_3^2\right)^2 = \left(\alpha_1^4 + \alpha_2^4 + \alpha_3^4\right) + 2\left(\alpha_1^2\alpha_2^2 + \alpha_2^2\alpha_3^2 + \alpha_3^2\alpha_1^2\right) = 1 \qquad (2.24)$$

Equation 2.23 can be further reduced to

$$\lambda_{\mathrm{Si}} = \lambda_{100} + 3\ (\lambda_{111} - \lambda_{100})\ \left(\alpha_1^2\alpha_2^2 + \alpha_2^2\alpha_3^2 + \alpha_3^2\alpha_1^2\right) \qquad (2.25)$$

The λ_{Si} is measured from the ideal demagnetized state. The λ_{100} and λ_{111} are also λ_{Si} values measured in constants of the material. In case of specimen having a particular, nonideal demagnetized state the quantity λ_S is highly structure sensitive and it depends on the mechanical, thermal, and magnetic history of the specimen. When the magnetic field is removed, the specimen may not reach an ideal demagnetized state, i.e., all possible domains are not present in equal volumes, λ_S is measured is a property only of that particular specimen. To avoid this problem, measurements are made with magnetic field applied in the directions parallel and perpendicular to the strain measurement direction.

2.3 Deformation by Slip

2.3.1 Burgers Vectors

Burgers vector, **b** is the dislocation displacement vector. A Burger circuit is any atom to atom path taken in the crystal containing one or few dislocations and forms a closed loop [25]. The Burgers circuit is shown in Figure 2.4a as the ABCDE path. If the same circuit is made in a dislocation free crystal then the circuit does not close and the vector required to close the circuit is called Burgers vector (Figure 2.4b). In a simple cubic crystal, Burgers vector is the shortest lattice translation vector which joins two points in the lattice. The Burgers vector of an edge dislocation is normal to the line of the dislocation and a screw dislocation is parallel to the line of the dislocation [25]. As in most cases, the dislocations are of mixed type and the dislocation line lies at an arbitrary angle to its Burgers vector. A Burgers vector of a single dislocation has a fixed length and direction, and is independent of the position and the orientation of the dislocation line [25].

2.3.2 Slip Planes and Slip Directions

The most common mode of plastic deformation in metals is slip. This can be described as sliding of one part of crystal over another along a definite crystallographic plane. These planes are called slip planes and the defined direction of movement is called the slip direction. Figure 2.5 shows the schematic of classical idea of slip [26]. The process is started with polished top surface of the crystal. In Figure 2.5a, shear stress is applied to the crystal and when it exceeds a certain value, slip occurs long the slip plane. Atoms move an integral number of atomic distances along the slip direction

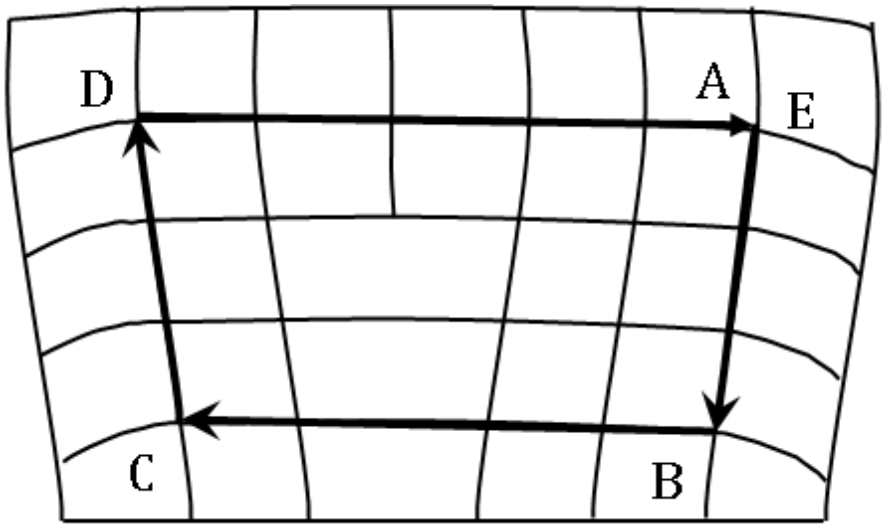

(a)

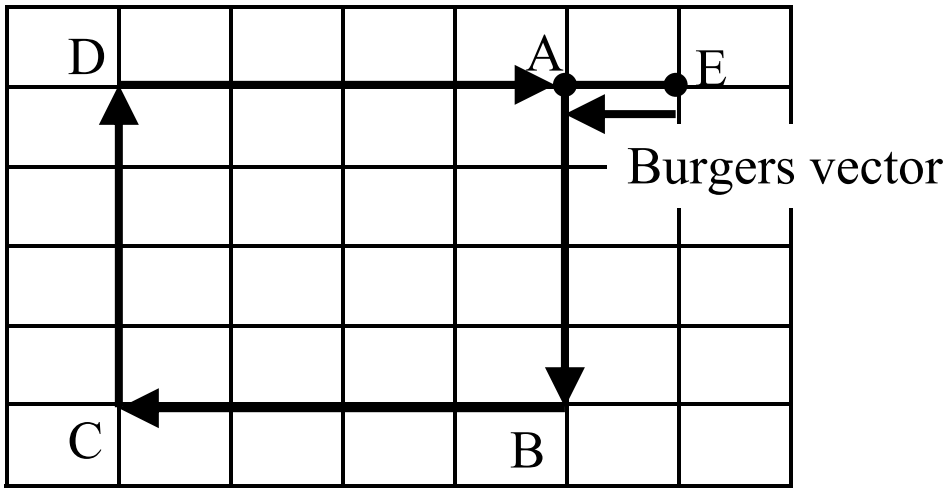

(b)

Figure 2.4 Schematic diagram for (a) Burger circuit around an edge dislocation and (b) same circuit in a perfect crystal; the closure failure is Burgers vector.

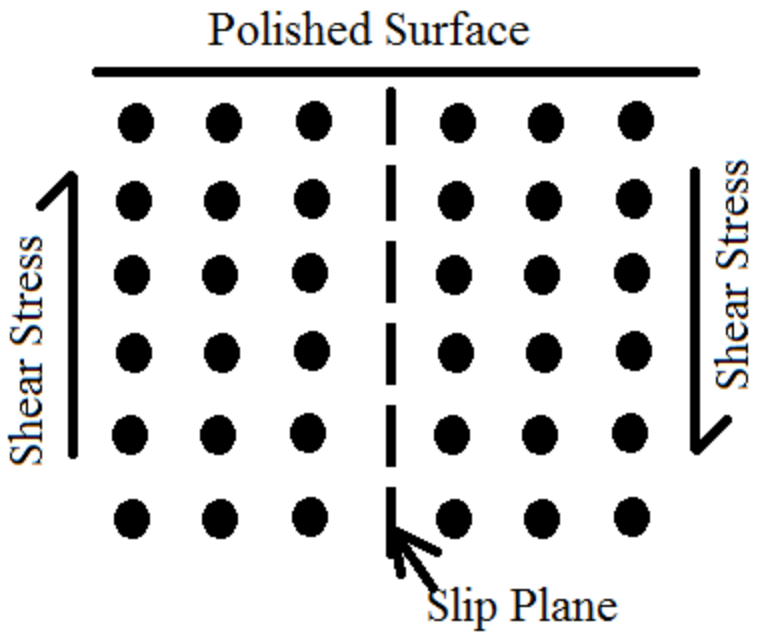

(a)

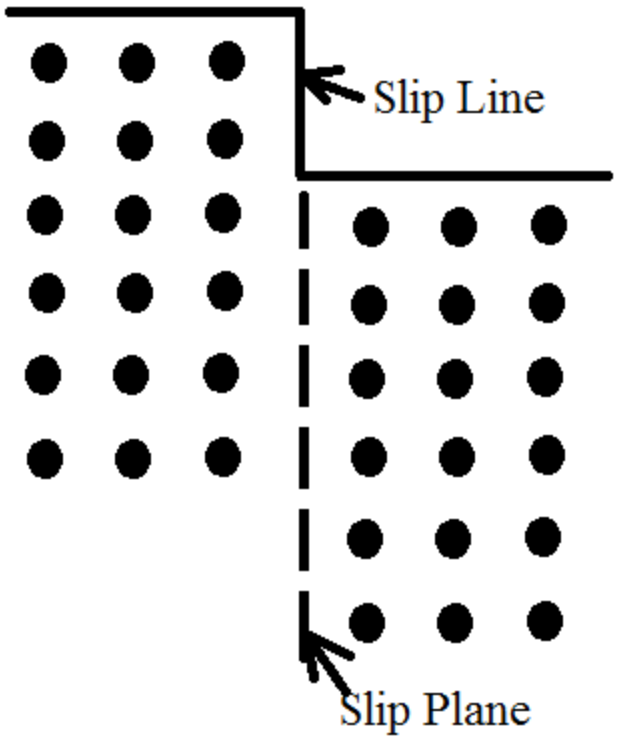

(b)

Figure 2.5 Schematic drawing of classical idea of slip.

on the slip plane and a step is produced. The step is viewed from the top of the polished surface as a line and this is called a slip line (Figure 2.5b). A single crystal deforms by slip in close-packed directions and on planes which are close-packed planes in general [20]. Slip lines are produced by sets of dislocations with same Burgers vector.

2.3.3 Slip Systems in BCC Crystals

According to the dislocation theory only a few low index glide planes and directions are important in deformation by slip of a crystal. For bcc crystal structure, Burgers vectors of perfect dislocations responsible for slip is ½ <111> [11]. Although the most densely packed planes are {110}, slip is observed to occur on several slip planes depending on the temperature and strain rate in bcc metals. Experimental evidence suggests that the order of operative slip planes with increasing temperature (T/Tm) is {110}, {112}, {123} and {hkl} [11].

At low temperature and high strain rates, {110} is the predominant slip plane and at high temperatures and low strain rates, {112} is the predominant slip plane. In summary, at low temperature the most common slip system in bcc materials is {110} <111>. With the combinations of these planes and directions, there are a total of twelve different possible slip systems. Table 2.1 shows the twelve possible slip systems in a bcc crystal.

2.3.4 Critical Resolved Shear Stress

Slip in a single crystal will occur only after the applied stress reaches a certain minimum value. This stress depends on the orientation of the active slip plane with

Table 2.1

Slip systems in BCC crystal

Plane	Direction
(110)	$[1\,\bar{1}\,1]$
(110)	$[\bar{1}\,1\,1]$
(011)	$[\bar{1}\,\bar{1}\,1]$
(011)	$[1\,\bar{1}\,1]$
(101)	$[\bar{1}\,1\,1]$
(101)	$[\bar{1}\,\bar{1}\,1]$
$(\bar{1}\,0\,1)$	[111]
$(\bar{1}\,0\,1)$	$[1\,\bar{1}\,1]$
$(0\,\bar{1}\,1)$	[111]
$(0\,\bar{1}\,1)$	$[\bar{1}\,1\,1]$
$(1\,\bar{1}\,0)$	[111]
$(1\,\bar{1}\,0)$	$[\bar{1}\,\bar{1}\,1]$

respect to the load axis and the geometry of the crystal. Slip begins when the shear stress on the slip plane in the slip direction reaches a threshold value and this shear stress resolved on the slip plane in the slip direction is called critical resolved shear stress, τ_R. For the requirement of exceeding the critical resolved shear stress for slip to occur, different tensile loads are required to produce slip in a single crystal of different orientations. Critical resolved shear stress can be expressed by the equation [26].

$$\tau_R = \frac{P}{A} \cos\phi \cos\lambda \qquad 2.26$$

where P is the load, A is the cross-sectional area of the sample, ϕ is the angle between the normal to the slip plane and the tensile axis, and λ is the angle between the slip direction and tensile axis (Figure 2.6). This was first recognized by Schmid [26] and the multiplication factor, m = $\cos\phi \cos\lambda$ is called Schmid factor. Shear stress is maximum when $\phi = \lambda = 45°$ and maximum value of m is 0.5. There will be no slip if the tensile axis is parallel to the slip plane ($\phi = 90°$) or perpendicular to the slip plane ($\lambda = 90°$). In that case resolved shear stress is zero.

2.3.5 Acoustic Emission During Deformation

Acoustic emission is a stress wave generated in a material and it can be generated from variety of sources like dislocation motion, precipitate fracture, strain-induced phase transformation, cracking, twining, etc. During the deformation of single

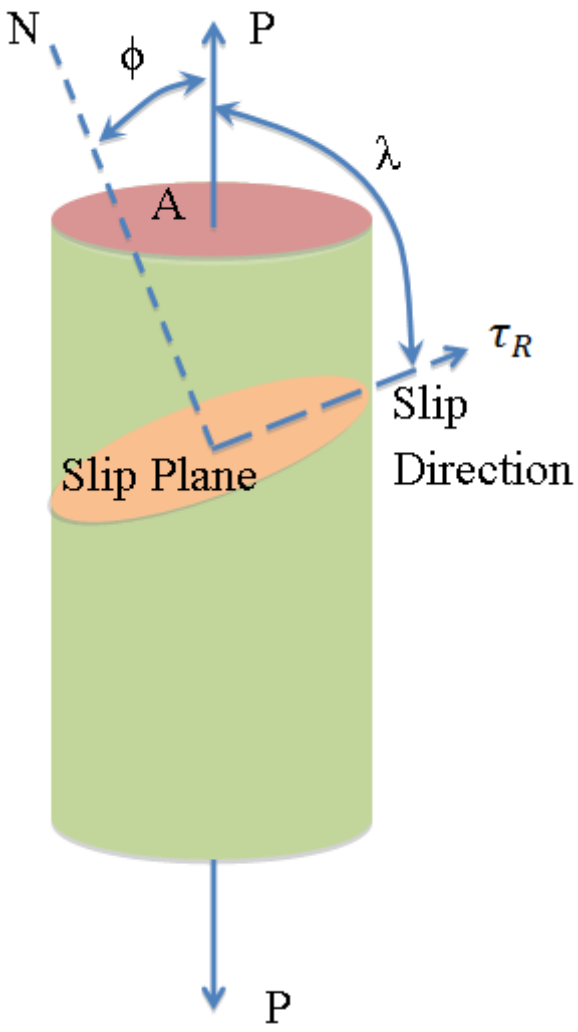

Figure 2.6 Schematic diagram for critical resolved shear stress calculation.

crystal, large elastic waves can be produced from dislocation motion when they move simultaneously or nearly simultaneously within a small volume of material. To produce a detectable acoustic emission, packets of dislocations have to move rapidly and far distances. In general, the conditions are satisfied simultaneously. Only a small fraction of energy associated with dislocation motion is released in the acoustic emission process and the rest is dissipated as heat.

Acoustic emission generation due to dislocation movement can be described by various models and these concentrate on one or more of the factors that affect the dislocation movement [27-28]. One of the models considers the pileup of the dislocation on the various pinning points. Once the stress exceeds the limit, there is a sudden release of the dislocations that generates stress waves which helps in unpinning of surrounding dislocations that results in an avalanche of dislocation motion within a short period of time. This theory is applicable for polycrystalline materials. Another model considers that the elastic acoustic waves are generated from the energy radiated by accelerating dislocation rather than elastic stress relaxation. The radiant energy is supplied by the force acting on the dislocation. As the dislocation moves through the lattice the core structure also changes and that also leads to the energy radiation and combination of all these energy radiations from the dislocation movement produces the acoustic emission [29]. This model describes well the acoustic emission during the deformation of a single crystal.

The acoustic signal captured during the deformation varies greatly with the measurement and machine condition. A machine having abnormal vibration and mechanical play will produce artifacts in the captured acoustic signal and it will be hard

to separate the actual acoustic emission signal from these artifacts. This also varies based on the testing method, nature of stress (compressive or tensile) and material type. For example, beryllium produces a larger signal during deformation as compared to stainless steel. Lower system noise (generated due to both testing machine condition and electrical connections for capturing the emitted signal) is desirable for the test.

2.4 Rare Earth Free Fe-Based Magnetostrictive Alloys

2.4.1 Fe-Ga Alloys

Large magnetostriction at a low saturation field is of prime interest in actuator and sensor applications. Tb_xDy_{1-x} shows very high magnetostriction (λ= ~10,000 ppm) at a saturation field of 16.3 kOe [30, 31]. Very low Curie temperature (~ -200 °C) restricts the use of these materials in cryogenic applications [30]. Terfenol-D with a composition $Dy_{0.7}Tb_{0.3}Fe_2$ is a widely used Fe based rare-earth material for sensor and actuator applications. This alloy has a Curie temperature near room temperature but requires high saturation field (~2 kOe). Other than a high saturation field requirement, this alloy has low mechanical strength and high associated material cost due to presence of rare-earth elements. Magnetostrictive materials with high mechanical strength, good ductility, large magnetostriction at low saturation field and lower cost are of prime interest. Due to strength and cost consideration, the search for alternative alloys started with identifying an α-Fe based alloy phase that has cubic structure and shows enhanced magnetostriction with low hysteresis.

Addition of Al increases the magnetostriction of Fe [32-33]. Fe-15 at.% Al shows a magnetostriction of 140 $x10^{-6}$ in the [001] direction. Al and Be both enhance the magnetostriction of Fe [31] and lead to dilation in lattice spacing but in opposite directions [34]. Both these elements do not have d-shell electrons in their structure. A hypothesis was made by Guruswamy et al. [2] that addition of nonmagnetic elements, in which the d-shell is empty or the d-shell is full, could be used to modify the magnetic coupling of Fe atoms to enhance the magnetostriction of iron if the elements have appreciable solubility in Fe.

The Ga atom is similar to Fe with respect to its atomic size and valence electron structure. Professor Guruswamy and coworkers hypothesized that Ga addition to Fe would result in large magnetostriction and experimentally observed that the addition of Ga to Fe dramatically increases the magnetostriction of Fe [2]. This work shows that (110) textured polycrystalline Fe-Ga alloy has a magnetostriction value of 110 $x10^{-6}$ along the specimen axis and that is a many fold increase in the magnetostriction of pure Fe [2]. In later work, it is also shown that the addition of Ga increases the magnetostriction of Fe and reaches a peak at Fe-20 at.% Ga. Reported saturation magnetostriction for various Fe-Ga alloys are shown in Table 2.2 [5]. The highest magnetostriction in Fe-20 at.% Ga LTA single crystal sample is 379 ppm which clearly illustrates that the magnetostrictive behavior of Fe-Ga alloys is far superior to the Ni, Ni-based alloys, Fe-Al, and Fe-Be alloys. Although this value is much lower than the Terfenol-D alloy, the Fe-Ga alloys have several advantages over the rare-earth based alloys: (a) Fe-Ga alloys are relatively less expensive compared to Terfenol-D alloy, (b) they have higher strength and ductility than Terfenol-D alloy due to presence of only

Table 2.2

λ_{100} for Fe–Ga single crystals

Alloy	Heat treatment condition	Magnetostriction, λ_{100} ($x10^{-6}$)
Fe-15 at.% Ga	As-directionally grown crystal (DG)	196
Fe-15 at.% Ga	LTA: Annealed at 1250 °C for 70 days	258
Fe-20 at.% Ga	As-directionally grown crystal (DG)	297
Fe-20 at.% Ga	LTA: Annealed at 1250 °C for 70 days	379
Fe-22.5 at.% Ga	LTA: Annealed at 1250 °C for 70 days	195
Fe-27.5 at.% Ga	As-directionally grown crystal (DG)	193
Fe-27.5 at.% Ga	LTA: Annealed at 1100 °C for 70 days	340
Fe-27.5 at.% Ga	ORD: Given DO_3 long-range ordering treatment	305

*Source of data: Guruswamy et al. [5]

simple body centre cubic (bcc) solid solution phase, and (c) they exhibit negligible hysteresis and have low saturation field.

Low saturation field requirement (<100 Oe) eliminates a need of massive field generation coils and cooling systems in Fe-Ga alloys. Small hysteresis characterized by intrinsic coercivities of less than 5 Oe leads to low energy loss/cycle. Curie temperature for Fe-Ga alloys are in the range of 650-780 °C and their magnetic and magnetostrictive behavior is therefore much less temperature sensitive. This behavior enables these alloys to operate in a broad range of temperature from cryogenic temperatures to as high as 600 °C.

In the last decade, extensive research work has been carried out to understand the various aspects of the Fe-Ga alloys. Considerable efforts have been initiated to (a) study the effect of solute content on the magnetostrictive behavior of the Fe-Ga alloy systems in both single crystal and polycrystalline materials [2-4,6-7,17,30,36-38]; (b) study the effect of heat treatment of various alloys on the magnetostriction and relationship between the structure changes and magnetostriction [3-4, 6-9]; (c) study the effect of partial substitution of Ga with various other elements (Al, W, Mo, Ni, Sn etc.) [3, 12, 14-16, 20, 35]; (d) study the mechanical properties of single crystals and polycrystalline Fe-Ga alloys [20, 39-42]; and (e) study the sensing and transduction behavior of these alloys [43-44].

The iron-rich portion of Fe-Ga phase diagram is shown in Figure 2.7 [35]. Fe-Ga alloy can exist as single-phase solid solutions with A2 structure over a large composition and temperature range. The solubility of Ga in Fe at 1037 °C is 36 at.% and at room temperature is 11 at.%. For Fe-20 at.% Ga, there is much less propensity

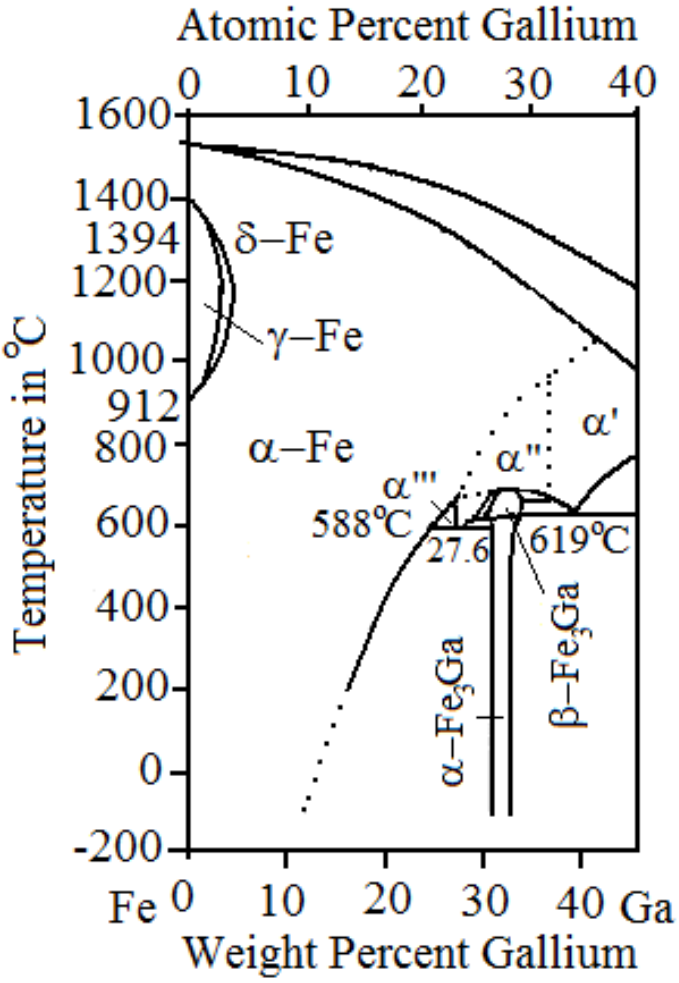

Figure 2.7 Fe rich portion of Fe-Ga phase diagram [35].

(Used with the kind permission of ASM International)

for forming ordered α' (DO_3 structure), α" (B2 structure), β (DO_{19} structure), and single phase α-Fe_3Ga ($L1_2$ structure) while cooling the alloys from high temperature. Rapid quenching from high temperature leads to the retention of the A2 structure in Fe-20 at.% Ga alloy at room temperature.

The formation of different ordered phases would require long term annealing at a high temperature in the stable phase region of desired ordered phase. As the solute content increases in the Fe-Ga alloy, the magnetostriction value also increases as shown in Table 2.2. The highest magnetostriction value is obtained for Fe-20 at.% Ga and then it again decreases with increase in Ga content. This decrease in magnetostriction is associated with the presence of ordered second phase in higher Ga content alloys.

Guruswamy et al. [2] show that the presence of 1% NbC in 99% Fe-20 at.% Ga reduces the magnetostriction coefficient from 115 x 10^{-6} to 88 x 10^{-6}. This suggests that strain generated by the NbC precipitate has an influence on the magnetostriction. Guruswamy et al. [5] showed a comparison of short range order and the magnetostriction in Fe-20 at. % Ga and Fe-27.5 at. % Ga alloys with two thermal histories. A (200) x-ray diffraction peak in the theta-2 theta scan corresponding to an as-grown Fe-27.5 at. % Ga single crystal in their work showed a split in the peak that indicates the presence of two regions, one with a lattice dimension closer to the sample, given the ordering treatment, and the other with a lattice dimension closer to the LTA and quenched sample. From Table 2.2, it is also clear that the annealed and quenched samples show higher magnetostriction as compared to as-grown samples having the same solute content.

Studies on the effect of quenching on the magnetostriction of Fe-Ga alloys [5-7] reveals that slow cooling from high temperature increases the formation of various second phases with various structures (DO_3, B2, $L1_2$) and that these structural changes lead to a reduction of magnetostriction. Magnetostriction of a directionally solidified Fe-27.5 at.% Ga polycrystalline sample having disordered A2 phase increases as the as-cast rods are annealed to homogenize and stress relieve while it decreases after DO_3 ordering treatment [4,5]. The magnetostriction decreases close to zero or small negative value after DO_{19} and $L1_2$ ordering treatment [4]. Lograsso et al. [7] also suggested local SRO and the presence of Ga pairs in the [001] directions in Fe-19 at.% Ga alloy single crystals. Another study by Xing et al. [45] suggests that the decrease in magnetostriction of Fe-29 at.% Ga related to the presence of A2, B2 and DO_3 phases. These results suggest that strain generated due to the presence of precipitate or ordered second phase has an influence on magnetostriction.

The substitution of Ga with various other elements like Al, W, Mo, V, Cr, Co, Rh, Ni, and Sn have also been investigated in recent years [12-15, 36]. It is found that substitution of Ga with these elements in Fe-(20-x) at.% Ga- x at.% Y (x=2.5 to 10 and Y = W, Mo, Al) always leads to a decrease in magnetostrictive and magnetic properties [12-13, 36].

Srisukhumbowornchai et al. [17] showed that $(Fe_{85}Ga_{15})_{99}(NbC)_1$ rolled alloy, warm rolled and then annealed at 700 °C for 1 h , has a tensile strength of about 580 MPa, yield strength of about 475 MPa and elongation of about 29%. Mungsantisuk et al. [20] studied elastic properties of various Fe-Ga polycrystalline samples and the Young's modulus and shear modulus they reported are shown in Table 2.3 [20, 36]. A

Table 2.3

Elastic properties of polycrystalline Fe–x at.% Ga alloys

Alloys	Young's Modulus (GPa)	Shear Modulus (GPa)
Fe-15 at.% Ga	170	74
Fe-20 at.% Ga	125	60
Fe-27.5 at.% Ga	117	46
Fe-32.5 at.% Ga	110	43

*Source of data: Mungsantisuk et al. [20]

detailed study on Fe-27.5 at.% Ga was done by Jayaraman et al. [9] and they reported elastic constants of different phases. For all the Fe-Ga alloys, the reported modulus values are several times larger than Terfnol-D [17, 36-38]. These studies suggest that Fe-Ga alloys have a very good combination of mechanical and magnetostrictive properties [2-4, 20, 40] and are able to provide large force deliveries at smaller strains.

2.4.2 Fe-Mo Alloys

As mentioned earlier, the discovery of large magnetostriction in Fe-Ga alloys led to increased efforts towards enhancing magnetostriction values in ductile α-Fe based alloys using low-cost non- rare-earth additions. Additions of elements with half-filled d shells in their ground state electronic configuration with Fe were investigated by Thuanboon [11]. He studied the effect of adding Group VI B elements, Cr, Mo and W, which have half filled d-shells in their ground state electronic configuration. The ground state electronic configuration of Mo is [Kr] $4d^5$ $5S^1$, and its atomic raddi is 1.36 Å [24]. Ground state electronic configuration of Fe is [Ar] $3d^6$ $4s^2$, and its atomic raddi is 1.24 Å [24]. Addition of Mo in Fe changes the Fe-Fe spacing and creates strain in the lattice. Magnetoelastic coupling which is the source of magnetostrictive strain is very sensitive to the interatomic spacing.

The Fe rich portion of Fe-Mo phase diagram is shown in Figure 2.8 [35]. Mo has a solubility up to 24.4 at.% in Fe at 1449 °C. The solubility of Mo decrease rapidly as temperature decreases. At room temperature, it is less than 3 at.%. Propensity for forming a second phase is higher in Fe-Mo alloys with higher Mo contents. Various ordered second phases (R, μ and λ) can form during cooling from high temperature.

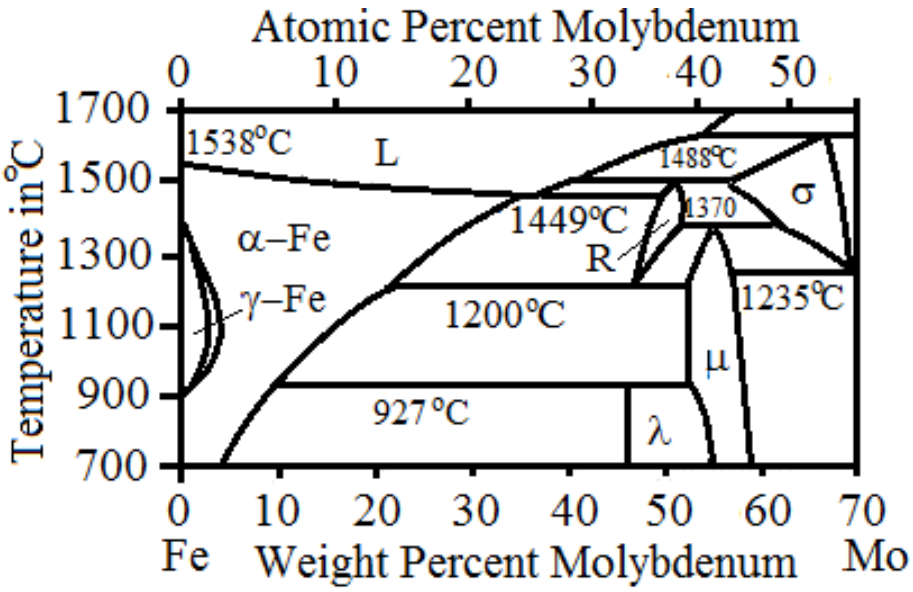

Figure 2.8 Fe rich portion of Fe-Mo phase diagram [35].

(Used with the kind permission of ASM International)

The influence of Mo in the ternary Fe-Ga-Mo alloy on the (100) disc sample was reported by Restorff et al. [15]. This work suggests that addition of Mo to Fe-Ga decreases the magnetostriction of the alloy. Magnetostriction of Fe- 13at.% Ga -2.7 at.% Mo is 40% lower than the Fe-15.7 at.% Mo. The Fe-10.2 at.% Ga-4.8 at.% Mo ternary alloy also shows a more negative λ_{111} value (-22 ppm).

Garside [12] studied the effect of partial substitution of Ga with Mo in Fe-20 at.% Ga using various alloy single crystals. The study reports that Ga substitution with Mo in Fe- (20-x) at.% Ga- x at.% Mo (x= 5,10) decreased the magnetostriction value with increasing Mo content. The magnetostriction (3/2 λ_{100}) of Fe-10 at.% Ga-10 at.% Mo annealed single crystal sample is 116 ppm, which is more than 70% lower than that of the annealed and quenched Fe-20 at.% Ga single crystal.

Hall had earlier studied the effect of Mo on Fe in the composition range of 2.18-4.35 at.% Mo [46]. He measured magnetostriction using (001)- and (011)-oriented single crystal disc samples at room temperature using the strain gage method. He observed that the magnetostriction value increases with an increase in Mo content, and the maximum saturation magnetostriction value is about 39.3×10^{-6} in Fe-4.35 at.% Mo. Thuanboon et al. observed in their study that Group VI B elements Cr, Mo, and W provided a large increase in the magnetostriction of Fe. They studied magnetic and mechanical properties of single crystals of two Fe-Mo compositions, Fe-15 at.% Mo and Fe-17.5 at.% Mo. The study reported a (3/2) λ_{100} value of 123×10^{-6} for Fe-15 at.% Mo [17] which is six times that observed in pure Fe (about 20×10^{-6}) [31]. On increasing Mo content to 17.5 at.%, the saturation magnetostriction (3/2) λ_{100} decreased to 75×10^{-6} [10]. The saturation magnetization also decreased from 164 emu/gm

(Fe-15 at.% Mo) to 155 emu/gm (Fe-17.5 at.% Mo). This reduction in saturation magnetization in Fe-17.5 at.% Mo suggests the presence of nonmagnetic second phase particle in the alloy [10]. These results also suggests that strain generated due to presence of the second phase has a significant effect on magnetostriction.

In this work, (i) the influence of well-defined dislocation arrays in a single crystal bcc Fe based solid solution phase on magnetostriction and (ii) the effect of Mo addition on magnetostriction of Fe have been examined. The first part examines the strain modulations in the lattice arising from two different sets of dislocation arrays introduced by controlled deformation along [100] and [126] directions. The second part of the work examines the role of coherent second phases that likely form in Fe-Mo alloys at higher Mo contents.

CHAPTER 3

EXPERIMENTAL PROCEDURE

3.1 Alloy Preparation and Single Crystal Growth

Alloy ingots of Fe-20 at% Ga alloy were prepared using high-purity elements in a high vacuum arc-melting furnace. Alloy ingots were melted several times to ensure homogeneity. The alloy was cast to a rod form by allowing the metal to flow into a 12.5 mm diameter cylindrical cavity inside a copper block with a thick alumina insulation sleeve. A schematic diagram of the casting set up is shown in Figure 3.1.

Single crystal of this alloy was grown using a seedless vertical Bridgman growth process. The vacuum arc-melted and cast rods were loaded into a closed-one end alumina tube, which was then connected to a vacuum pumping system and an ultra-high-purity (UHP) argon source in a standard Bridgeman growth system. The tube was evacuated and backfilled with UHP argon. The furnace was set at the predefined temperature to ensure complete melting of the alloy. The tube is then moved down the temperature gradient in a 2-zone furnace at a controlled rate of 3 mm/h using a stepper motor drive. As the tube moved through the temperature gradient region, solidification of the melt started from the bottom end of the tube. Directionally-grown (DG) single crystal rod of Fe-20 at. % Ga was obtained. A schematic of the single crystal growth system is shown in Figure 3.2.

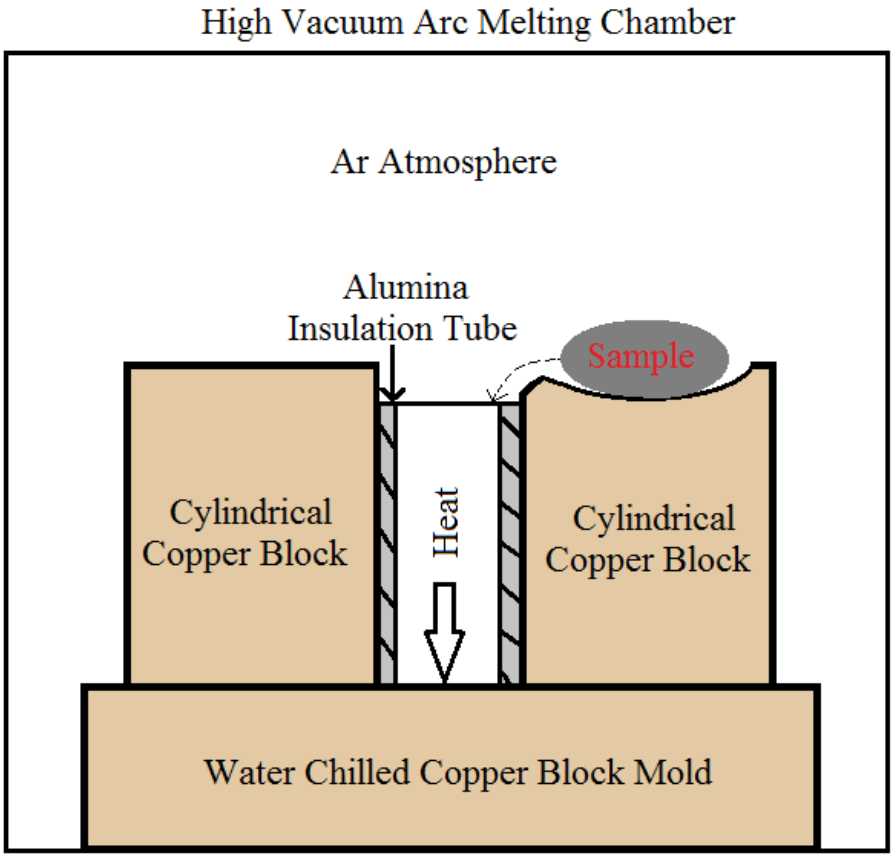

Figure 3.1 A schematic of the set up for directional solidification and casting.

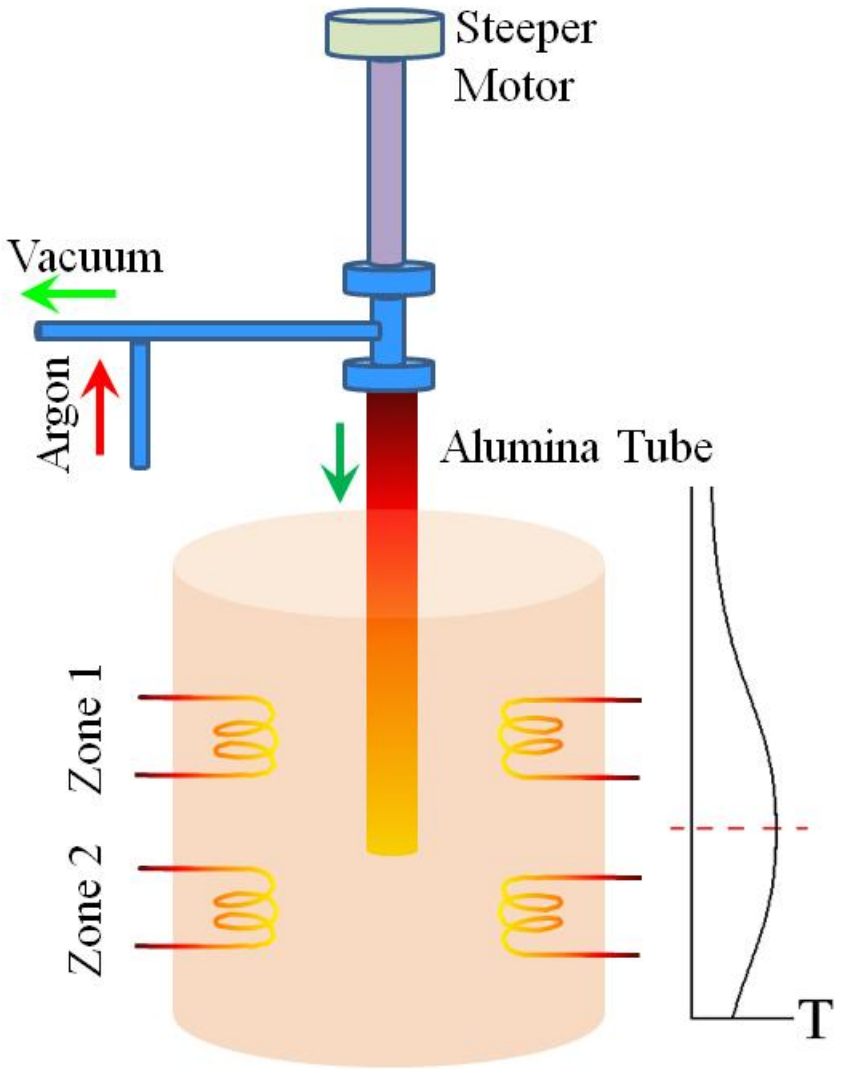

Figure 3.2 A schematic illustration of the directional growth set up.

In a similar way, Fe-5 at.% Mo, Fe-10at.% Mo and Fe-20at.% Mo DG single crystal rods were obtained. Crystal growth rate for these alloys was 22.5 mm/h.

3.2 Determination of Single-Crystal Sample Orientations Using X-Ray Diffraction

A single crystal was cut out from the DG rod and its characterization was done using a Siemens® D5000 x-ray diffractometer and Cu Kα radiation. Theta - 2 theta scans were carried out to obtain the 2 θ value for the (200), (211), (220) and (310) peaks. The 2 θ value obtained was then used for rocking curve scans. Rocking curve scans along with phi scans and detector scans were used to determine the single crystal orientation. This information was used for cutting and polishing the sample. After each step of polishing, rocking curve and phi scans were done to determine the crystal orientation.

Two [126]-oriented samples,8.93 x 9.52 x 19.48 mm^3 and 7.85 x 7.6 x 20.85 mm^3 in size, were prepared with the top and bottom faces that were ~21° from <200> direction. The other four faces were perpendicular to the top and bottom faces. Sample surfaces were metallographically ground and polished flat down to 0.05 μm alumina finish. Two [001]-oriented single crystal samples, 9.7 x 5.35 x 4.75 mm^3 and 9.33 x 6.52 x 5.93 mm^3 in size, were prepared with the faces oriented within 0.5 degree off the <100> direction. Sample surfaces were polished down to 0.05 μm alumina finish.

For λ_{100} measurements, [001]-oriented single crystals of Fe-5 at.% Mo, Fe-10 at.% Mo and Fe-20 at.% Mo were prepared with the faces oriented with in 0.50 off the <100> direction. The dimensions of the [001]-oriented Fe-5 at.% Mo, Fe-10 at.% Mo

and Fe-20 at.% Mo single crystals were 5.8 x 7.2 x 9.65 mm^3, 5.85 x 7.4 x 10.25 mm^3, and 5.9 x 8.75 x 12.7 mm^3 respectively.

For λ_{111} measurements, Fe-5 at.% Mo, Fe-10 at.% Mo and Fe-20 at.% Mo single crystal samples having [211], [220] and [111] faces were prepared. The [211] and [220] faces were within 0.5° off from the desired orientation. The [111] faces are <1° off from the <111> direction.

3.3 Annealing of the Single Crystal Sample

The oriented single crystal samples obtained after several cutting and polishing steps were sealed in quartz vials. Before sealing, the vials were evacuated and partially back-filled with UHP argon gas. Samples were heated to a temperature in the α-phase region corresponding to the given sample composition. Samples were kept there for two hours and then quenched rapidly in cold water. Fe-Ga and Fe-Mo phase diagrams are shown in Figure 2.7 and 2.8, respectively [35]. Annealing temperatures for various alloys are shown in Table 3.1.

3.4 Compression Test and Acoustic Signal Collection

The crystals were deformed to a predetermined stain values to introduce a controlled amount of defects. An Instron® 4505 compression testing machine was used for the compression test. A schematic illustration of the test set up is shown in Figure 3.3.

The [001]-oriented single crystal was deformed along [001] direction. The sample was deformed in two stages: (i) a 0.75% strain was first introduced and then (ii)

Table 3.1

Annealing temperatures used for various alloy single crystals

Alloy	Annealing Condition
Fe-20 at.% Ga	1150 °C for 2 h
Fe-5 at.% Mo	1150 °C for 2 h
Fe-10 at.% Mo	1200 °C for 2 h
Fe-20 at.% Mo	1400 °C for 2 h

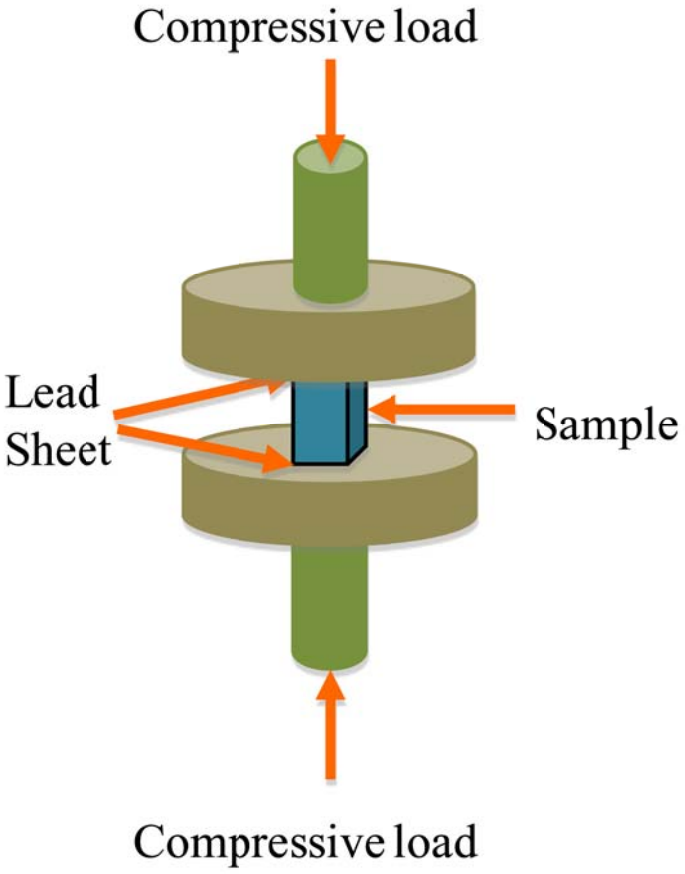

Figure 3.3 A schematic illustration of the compressive test set up.

a 3.4% strain was introduced on the top of previous strain. A strain rate of 5.18×10^{-5}/s was used for the deformation.

Compression was done along [126] direction for the [126]-oriented samples. A strain rate of 5.56×10^{-5}/s was used for the deformation. Deformation was stopped when the slip lines appeared and this appearance was accompanied by an acoustic emission.

Acoustic emission signals were collected using a SE150M High performance acoustic emission sensor (Dunegan Engineering Co., Inc.) attached to the test fixture and connected to the data acquisition system. Data were collected using both a Nicolet 310 storage oscilloscope and National Instrument data accusation system. Signals were collected at a rate of 1 point/μs in the oscilloscope and 20 points/ms in the data acquisition system consisting of a National Instruments high speed data acquisition board and LabView program.

3.5 Magnetostriction Measurements

The magnetostriction coefficient (3/2) λ_{100} measurements for [001]-oriented single crystals were made in all stages, (i) in the as-grown, (ii) after annealing and (iii) after deformation. A full bridge technique was used with an active strain gage attached to the sample and three dummy gages attached to a Bi rod, which has coefficient of thermal expansion similar to Fe. A schematic of the magnetostriction measurement set up is shown in Figure 3.4. Magnetostriction measurements were made using a strain gage attached along the [001]-direction on the 9.7×5.35 mm^2 face. The measurements were made with magnetic field applied (i) parallel to [001] direction (Figure 3.5, Configuration 1) and (ii) parallel to [010] direction (Figure 3.5, Configuration 2).

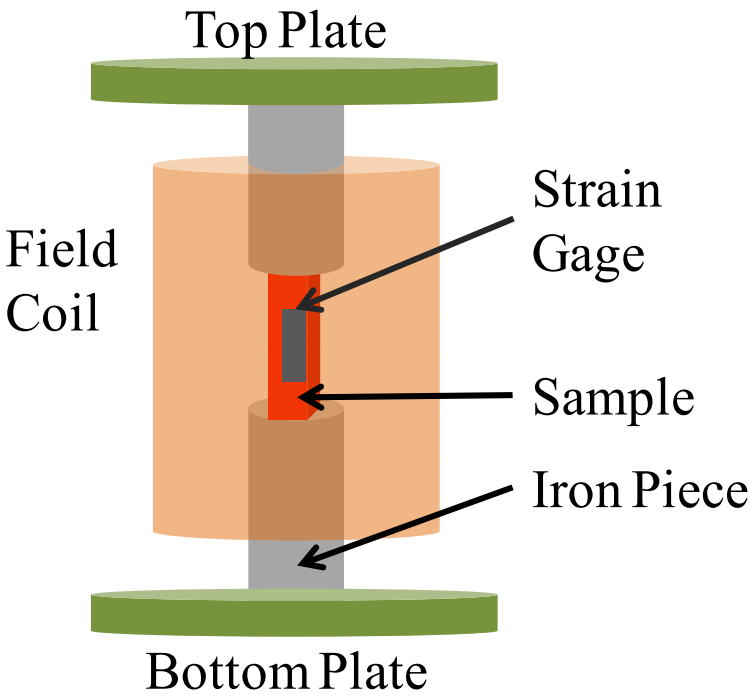

Figure 3.4 A schematic of magnetostriction measurement set up.

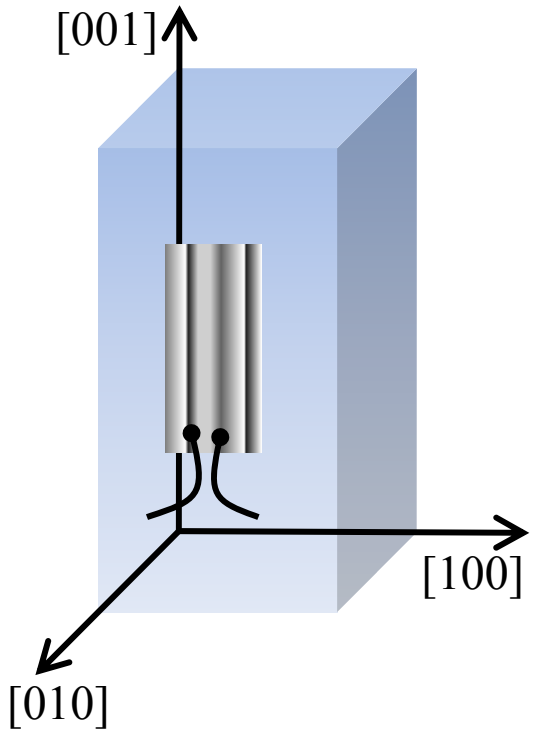

Measurement Configuration 1

Field Direction: [001]

Strain Measurement Direction: [001]

Measurement Configuration 2

Field Direction: [010]

Strain Measurement Direction: [001]

Figure 3.5 Magnetostriction measurement configurations for [001]-oriented crystal.

Signals corresponding to the applied magnetic field and the magnetostriction were collected using an IOTECH® ADC 488/16A data acquisition system and an IOTECH® MUX 488/16SC signal conditioning multiplexer unit.

The magnetostrictive strain measurements were made on the [126]-single crystal samples in the as-grown condition, after annealing and after plastic deformation to various strain levels. The strain gage was attached on the same face and at the same position on the sample for all the measurements. In the case of a [126]-oriented single crystal, the first set of measurements were made by attaching the strain gage longitudinally parallel to [126] direction on face 1 (9.52 x 19.48 mm^2 face) (Figure 3.6 a). The strain measurements were made with magnetic field applied (i) parallel to [126] for $\lambda_{//}$ (Figure 3.6 a, Configuration 1); (ii) parallel to $[\overline{20}13]$ (Figure 3.6 a, Configuration 2) and (iii) parallel to $[03\bar{1}]$ (Figure 3.6 a, Configuration 3) for $\lambda_{\perp}$. A second set of measurements were also made by attaching the strain gage parallel to $[03\bar{1}]$ on face 1 (9.52 x 19.48 mm^2 face) (Figure 3.6 b). The strain measurements were made with magnetic field applied (i) parallel to $[03\bar{1}]$ for $\lambda_{//}$ (Figure 3.6 b, Configuration 4); (ii) parallel to $[\overline{20}13]$ (Figure 3.6 b, Configuration 5) and (iii) parallel to [1 2 6] for $\lambda_{\perp}$ (Figure 3.6 b, Configuration 6). The differences in the magnetostrictive strains $\lambda_{//}$ and $\lambda_{\perp}$ were compared for the various sample conditions viz. as-grown, as-annealed and after deformation.

Magnetostriction coefficients λ_{111} of Fe-5 at.% Mo, Fe-10 at.% Mo and Fe-20 at.% Mo were also measured. For λ_{111} measurement, single crystal samples having [211], [220] and [111]-oriented faces were prepared. In the case of Fe-5 at.% Mo and

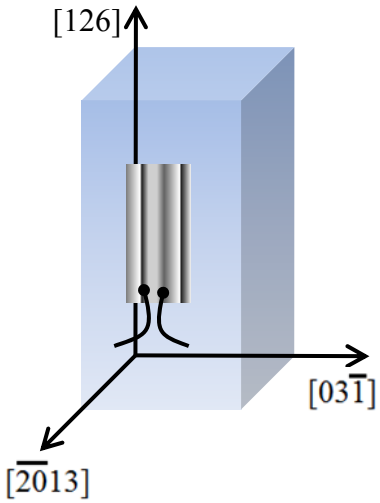

(a)

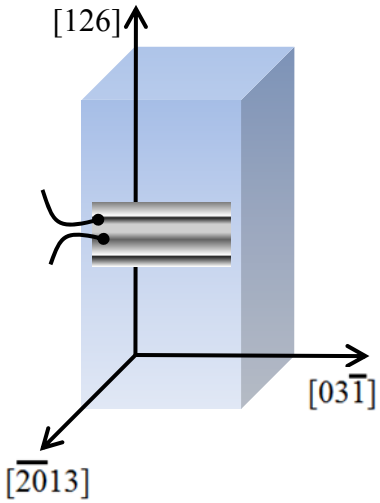

(b)

Measurement Configuration 1

Field Direction: [126]

Strain Measurement Direction: [126]

Measurement Configuration 2

Field Direction: [$\bar{2}$0 1 3]

Strain Measurement Direction: [126]

Measurement Configuration 3

Field Direction: [03 $\bar{1}$]

Strain Measurement Direction: [126]

Measurement Configuration 4

Field Direction: [03 $\bar{1}$]

Strain Measurement Direction: [03 $\bar{1}$]

Measurement Configuration 5

Field Direction: [$\bar{2}$0 1 3]

Strain Measurement Direction: [03 $\bar{1}$]

Measurement Configuration 6

Field Direction: [126]

Strain Measurement Direction: [03 $\bar{1}$]

Figure 3.6 Magnetostriction measurement configurations for [126]-oriented crystal.

Fe-20 at.% Mo single crystals, the strain gage was attached on the [211]-oriented face, and for Fe-10 at.% Mo single crystal the strain gage was attached on the [220]-oriented face, along the [111] direction. Strain was measured along the [111]-direction.

For Fe-5 at.% Mo and Fe-20 at.% Mo $\lambda_{//}$ measurements were made by applying the field along the [111] direction (Figure 3.7 Configuration 1), and the $\lambda_{\perp}$ measurement was made by applying the field along $[1\bar{1}0]$ direction (Figure 3.7 Configuration 2).

In the case of Fe-10 at.% Mo $\lambda_{//}$, measurement was made by applying the field along [111] direction (Figure 3.8 Configuration 1), and the $\lambda_{\perp}$ measurement was made by applying the field along $[1\bar{2}1]$ (Figure 3.8 Configuration 2). Measurements were made both in the as-grown condition and after annealing. The measured values were used to calculate λ_{111} for those alloys.

3.6 Magnetization Measurements

Magnetization measurements of Fe-5 at.% Mo, Fe-10 at.%Mo and Fe-20 at.% Mo as cast samples were made using high-vacuum arc-melting furnace. Small samples, around 2x2x2 mm^3 in size, were cut from the cast rod for magnetization measurements. Magnetization measurements were performed at room temperature using a Lakeshore® Model 7307 vibrating sample magnetometer with Lakeshore® Model 735 VSM control electronics and a Lakeshore® Model 450 Gaussmeter. A maximum field applied during these measurements was 10 kG.

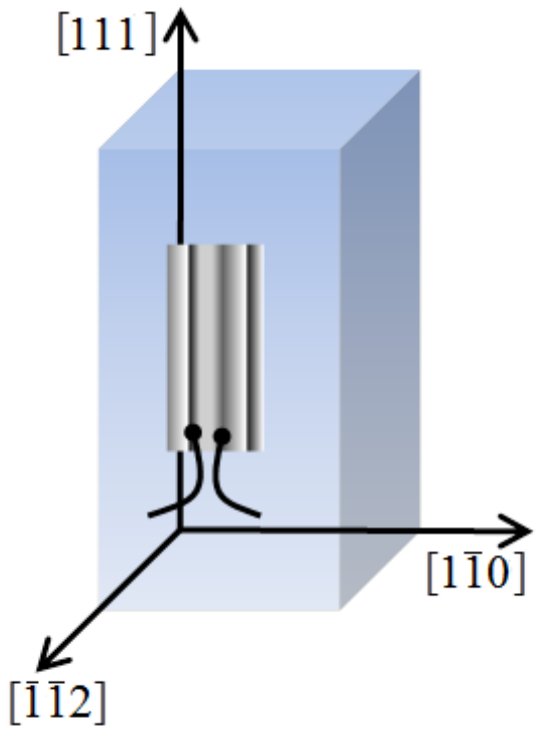

Measurement Configuration 1

Field Direction: [111]

Strain Measurement Direction: [111]

Measurement Configuration 2

Field Direction: [1 $\bar{1}$ 0]

Strain Measurement Direction: [111]

Figure 3.7 Magnetostriction measurement configurations for λ_{111} measurement of Fe-5 at.% Mo and Fe-20 at.% Mo.

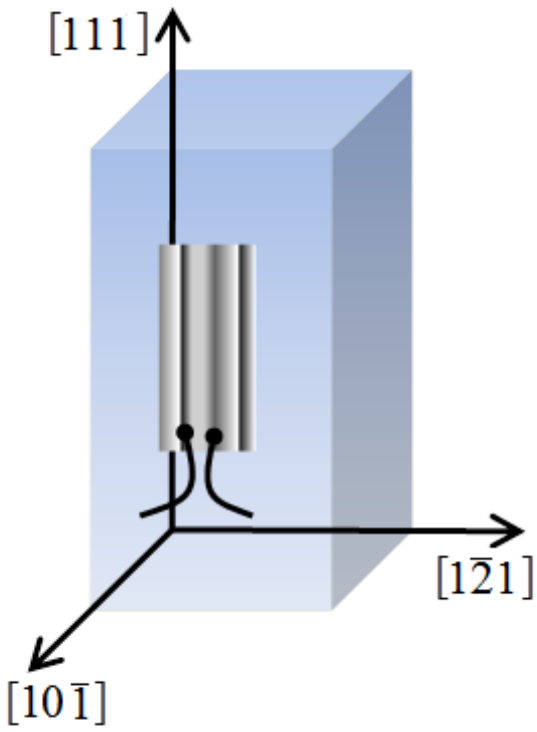

Measurement Configuration 1

Field Direction: [111]

Strain Measurement Direction: [111]

Measurement Configuration 2

Field Direction: [1$\bar{2}$1]

Strain Measurement Direction: [111]

Figure 3.8 Magnetostriction measurement configurations for λ_{111} measurement of Fe-10 at.% Mo.

3.7 TEM Sample Preparation

TEM samples of deformed [001]-oriented, [126]-oriented Fe-20 at.% Ga samples and a Fe-20 at.% Ga LTA sample were prepared. Slices were cut from the single crystal samples and then polished to bring down the thickness to within the range of 120 μm to 220 μm. The surface was finished with 1 μm diamond paste. The polished sample was then used for cutting 3 mm discs. The 3 mm discs were electropolished using an electrolyte consisting of perchloric acid, ethylene glycol monobutyl ether, ethanol and water to obtain samples with electron transparent regions for TEM examination. Before TEM examination, transparency of sample was checked in NovaNao SEM using the STEM mode. TECNAI F20 sTEM in the Electron Microscopy Center User Facility at the Argonne National Laboratory was used for TEM examination.

CHAPTER 4

RESULTS AND DISCUSSION

4.1 Deformation Studies in [001] and [126]-Oriented Single Crystals

4.1.1 Orientation of [001] Single Crystal Sample

Preparation of oriented single crystal samples involves very critical and laborious iterations of crystal orientation and polishing steps. The (200) rocking curve x-ray diffraction scans were obtained from all the six faces. The 2 θ value obtained from θ-2 θ scan for the (200) peak is 64.15. The θ-2 θ scan for Fe-20at.% Ga directionally grown sample is shown in Figure 4.1.

A rocking curve scan obtained from one of the sample faces after polishing is shown in Figure 4.2. For the rocking curve scan, the detector was fixed at 2 θ = 64.15° with respect to the source and the sample was rotated about the diffractometer axis with the angle between the sample surface and the incident beam indicated by the symbol ω. The intensity peak in the (002) rocking curve scan intensity indicates the position of the sample surface for which the (002) plane of the sample satisfies the Bragg condition and the (θ-ω) is the deviation of the sample surface normal from the <001> direction. The ω value for the peak in the plot is 32.02 suggesting the scanned sample surface normal deviation of 0.02 degree from the <001> direction. All other faces were also oriented

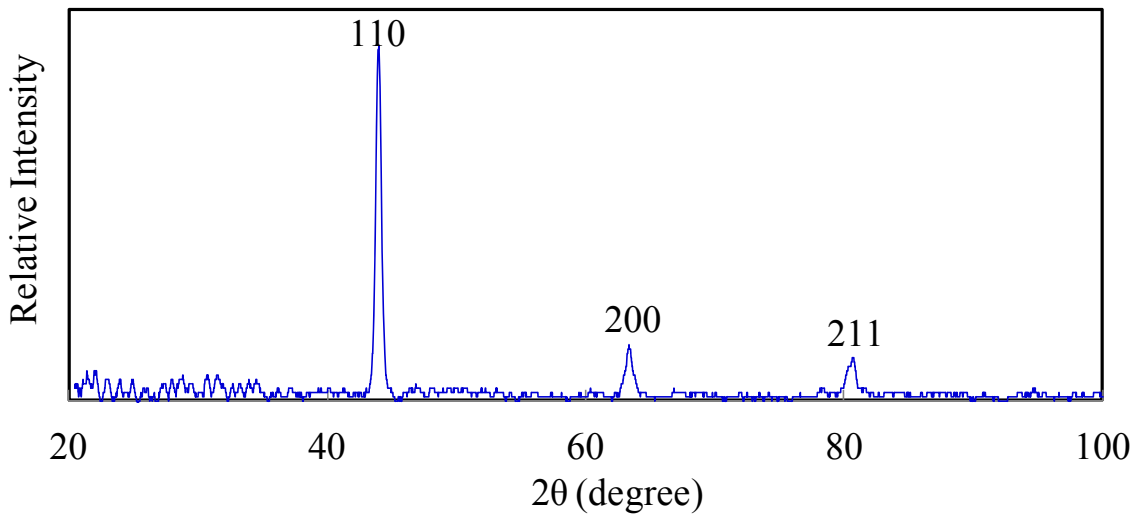

Figure 4.1 X-ray diffraction pattern of Fe-20 at.% Ga directionally grown single crystal.

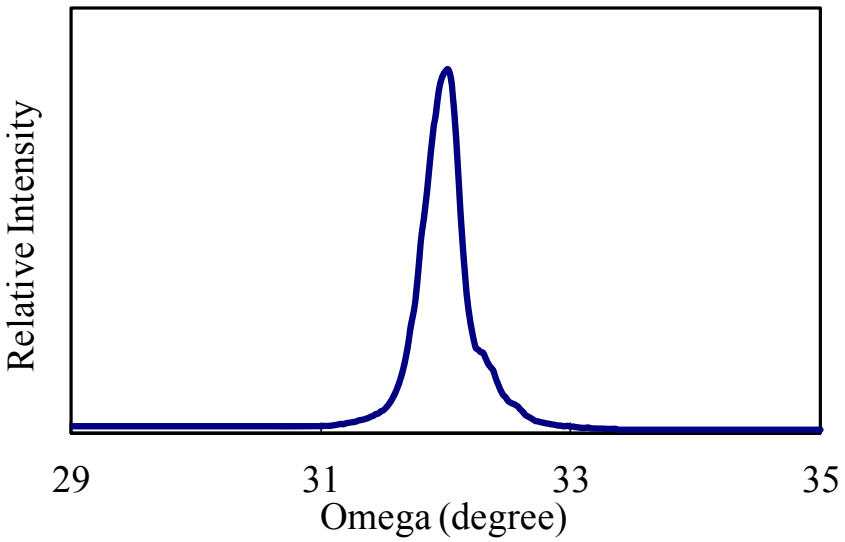

Figure 4.2 Rocking curve scan corresponding to (001) peak for one of the six faces of [001]-oriented single crystal.

well within 0.25 degree from the <001> direction. A pole figure of the sample with [001]-load axis is shown in Figure 4.3.

4.1.2 Orientation of [126] Single Crystal Sample

The (200), (211) and (310) x-ray diffraction rocking curve scans were done to identify the orientation of the top and bottom faces and thus define the deformation direction. Figure 4.4 shows the rocking curve scans corresponding to the (200) peak for the bottom crystal face. For the (200) rocking curve scan, the detector was fixed at $2\theta = 64.26°$ with respect to the source, and the sample was rotated about the diffractometer axis with the angle between the sample surface and the incident beam indicated by the symbol ω. The intensity peak in the (200) rocking curve scan indicates the position of the sample surface for which the (002) plane of the sample satisfies the Bragg condition and the $(\theta-\omega)$ is the deviation of the sample surface normal from the <001> direction. The ω value for the peak in the plot is 10.86° suggesting the scanned sample surface normal deviation of 21.24° from <001> direction. The rocking curve peak in Figure 4.4 shows an asymmetry, and this likely arises from the asymmetric reflection geometry in the case of a [126]-oriented crystal. Other possible sources of asymmetry in diffraction peaks are $K\alpha_1$ and $K\alpha_2$ emission profile asymmetry (dominant in peaks corresponding to $2\theta > 90°$) and horizontal and axial beam divergences [47-49]. From the (310) rocking curve, the deviation of the top surface normal from [310] direction is 9.75°.

Though only rocking curve scans corresponding to two sets of planes, say (200) and (310), are needed, an additional rocking curve scan corresponding to (211) was also done for an additional confirmation of orientation of the top and bottom faces. For the

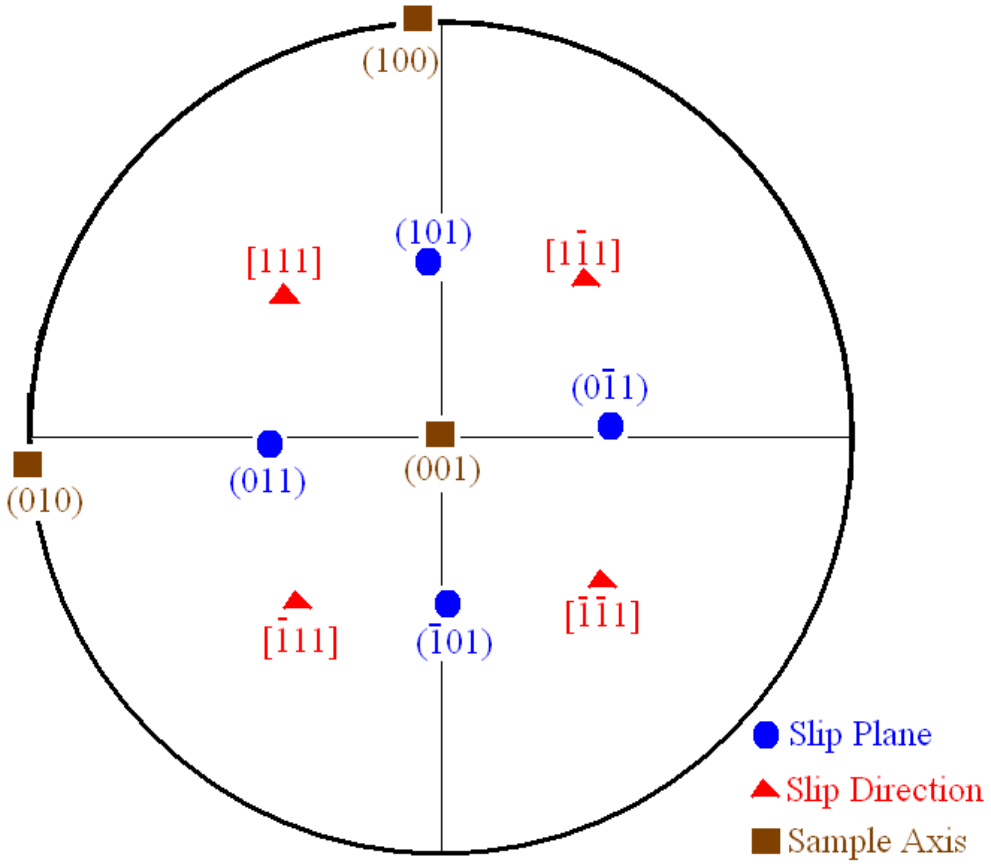

Figure 4.3 Pole figure showing the deformation direction and operative slip system for the [001]-oriented single crystal.

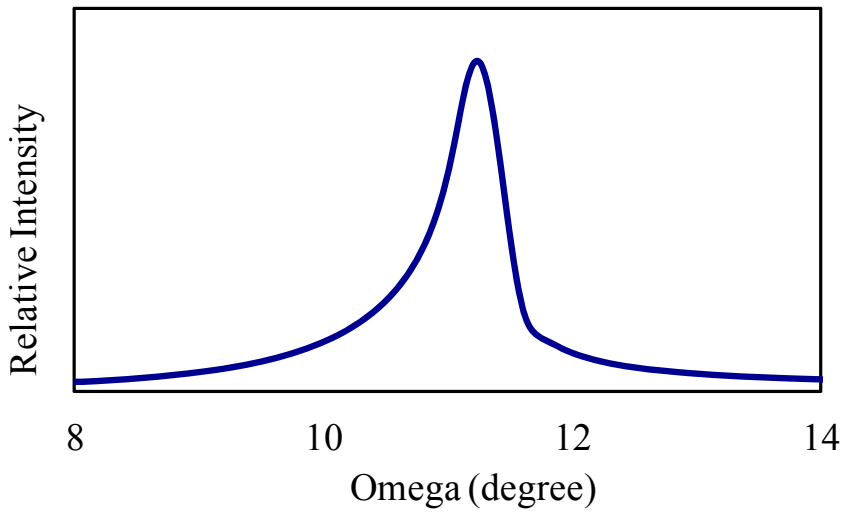

Figure 4.4 The (200) rocking curve for the bottom face of [126]-oriented single crystal.

other four faces normal to the top and bottom face, (200) and (310) rocking curve scans were performed to identify the face-normal directions. Orientations of all the faces are shown in Table 4.1 and Figure 4.5.

4.1.3 Deformation of a [001]-Oriented Single Crystal

High levels of dislocations were then introduced by applying a controlled amount of deformation. Compressive deformation was carried out in two steps. In the first step, a plastic strain of 0.75% was introduced, and 3.4% additional strain was introduced in the second step. Compressive deformation of the sample was applied along the [001] direction of the crystal. The engineering stress-strain plots of the compression steps are shown in Figures 4.6a and 4.6b. Slip lines observed using an optical microscope on one of the lateral sample surfaces after the first deformation step is shown in Figure 4.6c.

Schmid factors were calculated from the orientation data for the sample and are shown in Table 4.2. Due to the high symmetry of this configuration, the deformation along [001] activates multiple slip along eight slip systems. A schematic of the eight operative different slip systems are shown in Figure 4.7.

4.1.4 Deformation of a [126]-Oriented Single Crystal

Dislocations were introduced after annealing by applying a controlled amount of deformation to the [126]-oriented crystal. Based on the orientation of the crystal, Schmid factors were calculated for the various operative slip systems when the crystal is compressively deformed along the [126] axis. Table 4.3 shows the eight slip systems

Table 4.1

Measured orientation of a [126] single crystal

Face	Deviation from the nearest <002> direction	Deviation from the nearest <310> direction
Top and bottom face	21.24 °	9.75 °
Face 1 and Face 3	19.87 °	9.50 °
Face 2 and Face 4	13.28 °	8.40 °

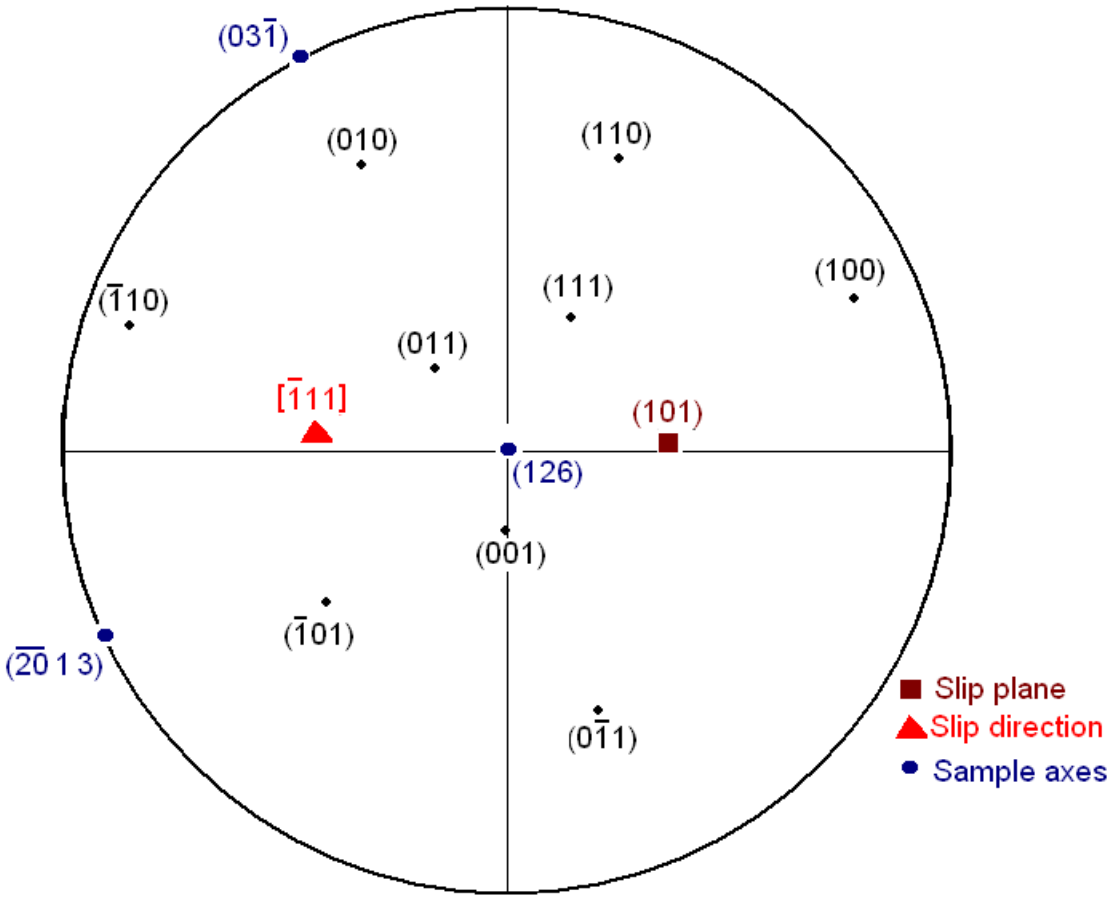

Figure 4.5 Pole figure showing the deformation direction and operative slip system of [126]-oriented single crystal.

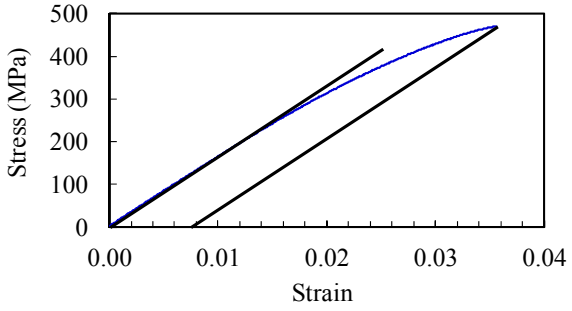

(a)

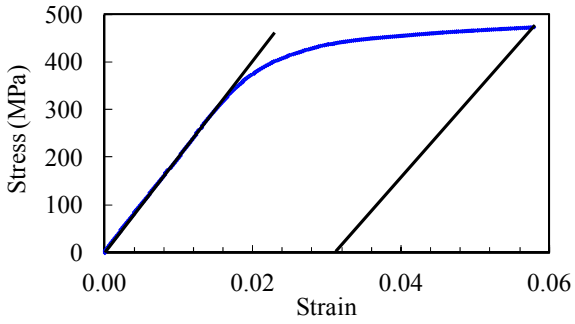

(b)

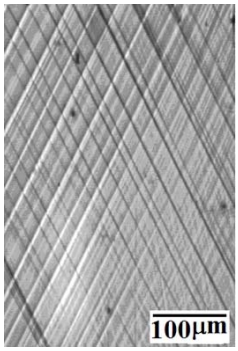

(c)

Figure 4.6 Compression test of the Fe-20 at. % Ga [001] oriented single crystal (a) stress-strain curve for the first deformation step resulting in 0.75% plastic strain, (b) stress-strain curve for the second deformation step resulting in 3.4% additional plastic strain and (c) optical microscope image of crystal surface after 0.75% plastic strain.

Table 4.2

Calculated Schmid factors for eight slip systems

of a [001]-oriented single crystal

Plane	λ	Direction	θ	cosθcosλ
(011)	45.00	$[1\,\bar{1}\,1]$	54.7	0.409
$(0\,\bar{1}\,1)$	45.00	[111]	54.7	0.409
(101)	44.95	$[\bar{1}\,11]$	54.77	0.408
(101)	44.95	$[\bar{1}\,\bar{1}\,1]$	54.77	0.408
$(\bar{1}\,01)$	45.05	$[1\,\bar{1}\,1]$	54.7	0.408
$(\bar{1}\,01)$	45.05	[111]	54.7	0.408
$(0\,\bar{1}\,1)$	45.00	$[\bar{1}\,11]$	54.77	0.408
(011)	45.00	$[\bar{1}\,\bar{1}\,1]$	54.77	0.408

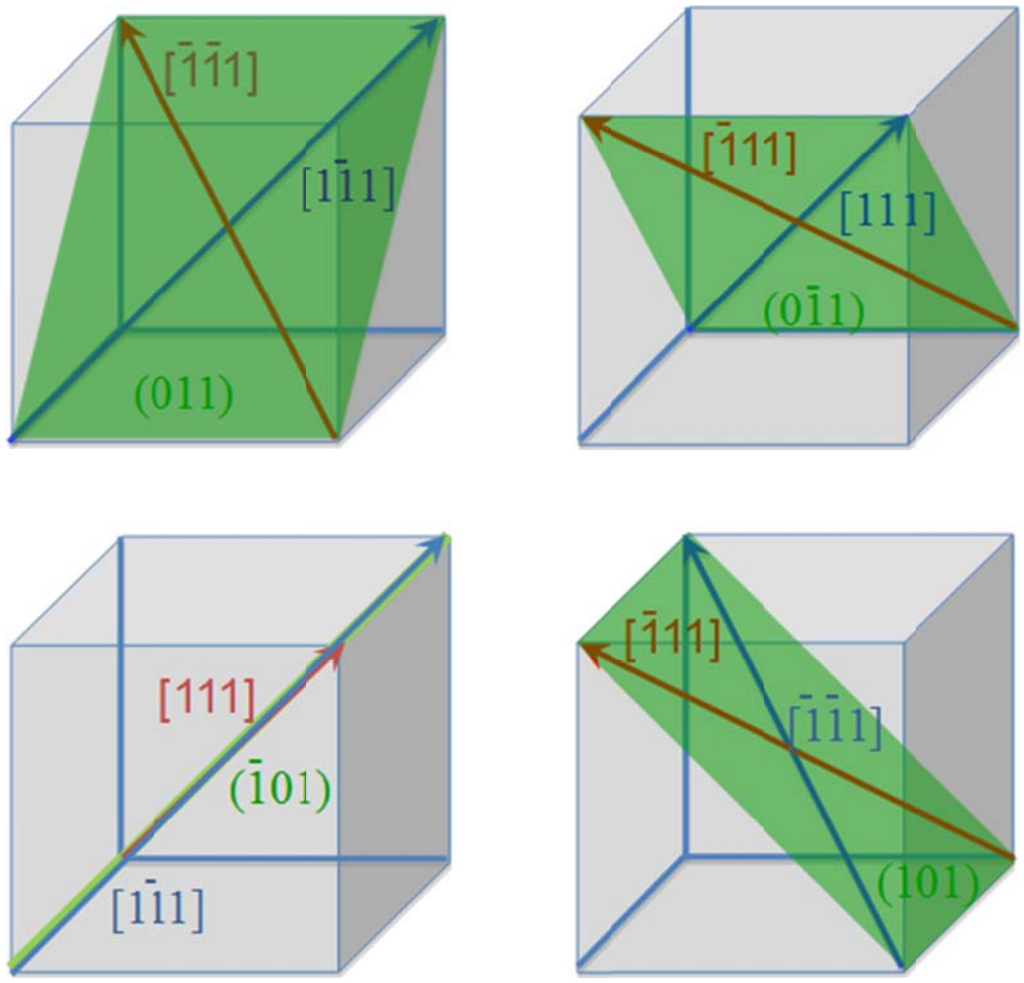

Figure 4.7 Schematic of eight different slip system in [001]-oriented Fe-20 at.% Ga single crystal while deform along [001] direction.

Table 4.3

Calculated Schmid factors based on measured orientation data for various slip systems of a [126]-oriented single crystal

Plane	λ	Direction	θ	Cos θ Cos λ
(101)	39.38	$[\bar{1}\,1\,1]$	50.86	0.4879
$(\bar{1}\,0\,1)$	56.48	[111]	35.75	0.4482
(011)	27.93	$[1\,\bar{1}\,1]$	63.21	0.3982
$(0\,\bar{1}\,1)$	63.79	$[\bar{1}\,1\,1]$	50.86	0.2788
$(\bar{1}\,0\,1)$	56.48	$[1\,\bar{1}\,1]$	63.21	0.2489
(101)	39.38	$[\bar{1}\,\bar{1}\,1]$	74.31	0.2090
(110)	70.65	$[1\,\bar{1}\,1]$	63.21	0.1493
$(\bar{1}\,1\,0)$	83.65	$[\bar{1}\,\bar{1}\,1]$	74.31	0.0299

with corresponding Schmid factors. This shows that slip will occur only on the $(101)[\bar{1}\,1\,1]$ slip system during the initial deformation. Schematic of the operative slip system during initial deformation is shown in Figure 4.8. The sample was compressively deformed along the [126] direction at a strain rate of 5.56 x 10^{-5} /s. The corresponding engineering stress versus strain plot is shown in Figure 4.9. Deformation was stopped when the slip lines appeared, and this appearance was accompanied by acoustic emission and a small drop in stress. During the deformation carried out, only one set of slip systems was operative and one set of parallel slip lines was observed on the faces. Figure 4.10 shows the low magnification optical image of slip lines observed on the sample faces after the compression test. If the loading were to continue, crystal rotation will occur with the slip plane normal moving away from the applied stress direction [11, 50]. Beyond a certain strain level, the crystal rotation would result in the operation of a second slip system as well. The deformation level shown in Figure 4.9 and the consequent crystal rotation is so small or negligible, that only a single slip system is operative during the deformation step in this work.

4.1.4.1 Acoustic Signal Emitted During the Deformation of [126]-Oriented Single Crystal

Acoustic emission signals were emitted at the onset of slip band formation during the deformation of the first [126]-oriented crystal. To collect and analyze these signals, deformation of a second [126]-oriented Fe-20 at.%Ga single crystal was carried out with a SE150M high performance acoustic emission sensor attached to the test fixture and connected to both an oscilloscope and a LabView data acquisition system.

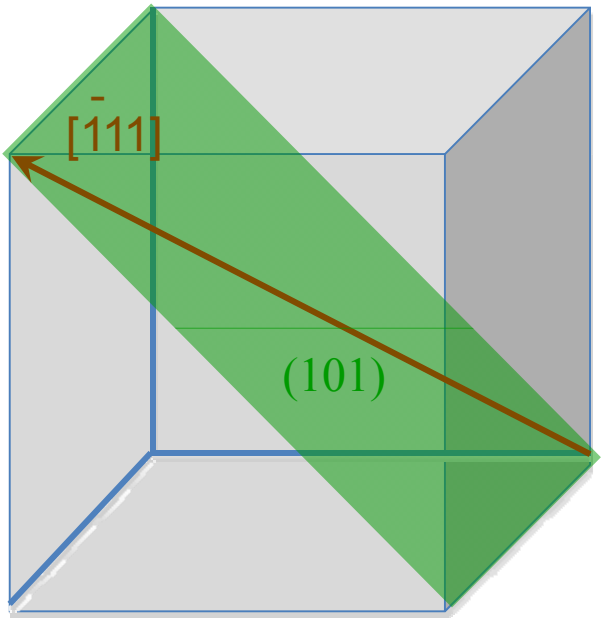

Figure 4.8 Operative slip system during initial deformation in [126]-oriented Fe-20 at.% Ga single crystal.

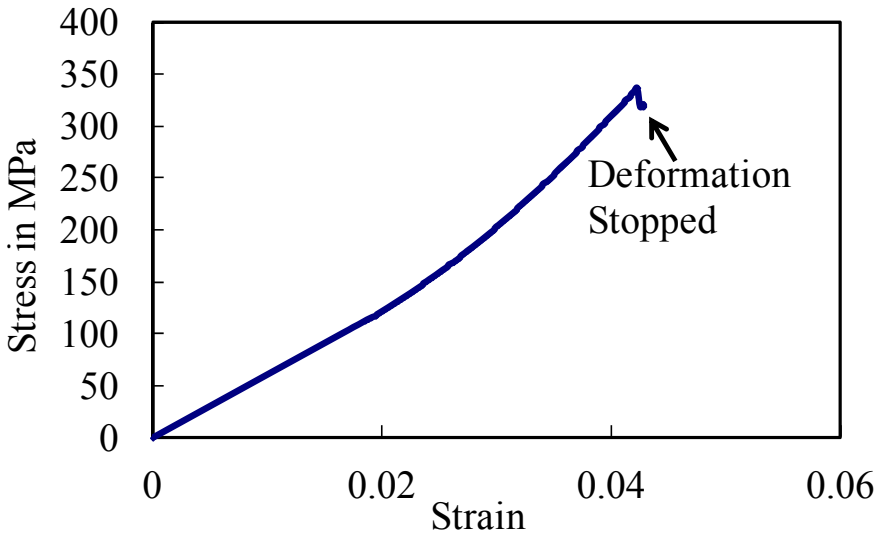

Figure 4.9 Compressive stress versus strain plot of [126]-oriented Fe-20 at.% Ga single crystal.

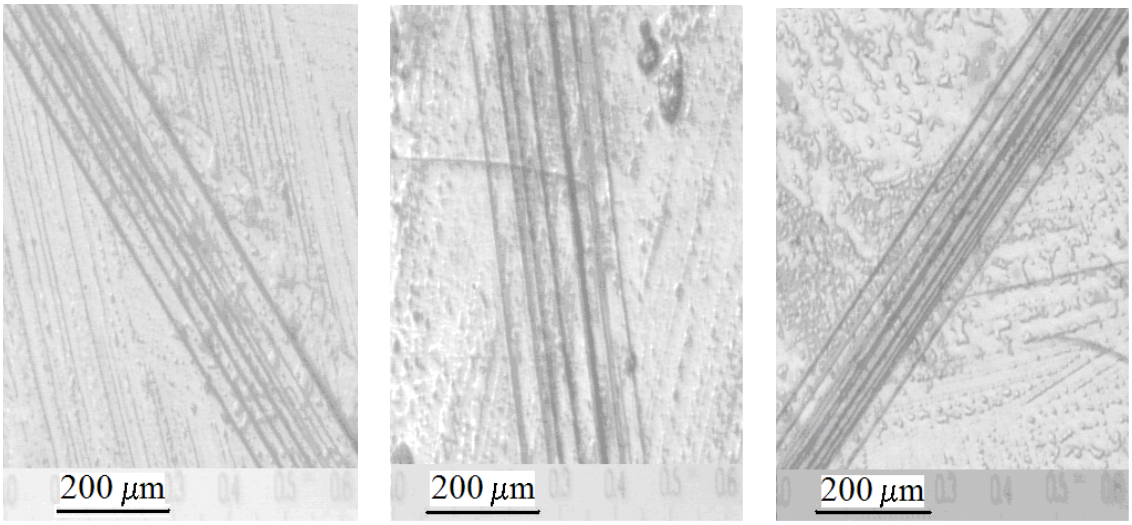

(a) (b) (c)

Figure 4.10 Optical micrographs showing the slip lines on (a) side face 1 (b) side face 2 and (c) side face 3 after the deformation of the [126]-oriented Fe-20 at.% Ga single crystal.

Multiple emission events were observed when the single crystal was deformed. The National Instrument data accusation system was used to collect the signal continuously from beginning to end of the compression test. Figure 4.11 shows a 400 ms time duration acoustic emission signal containing the peak signal collected by National Instrument data acquisition system. This also indicates the low noise level of the system and the high intensity of the signal. Figure 4.12 shows the initial portion of the acoustic signal collected by the Nicolet oscilloscope. The signal collection and storage in the oscilloscope is limited to 4000 μs. The signal collected in the oscilloscope from 300 μs before the onset of the emission event to 3700 μs after the onset of the emission event (trigger point) was stored. Each of these signals corresponds to events occurring during the formation of a slip band. To confirm the acoustic signal was generated due to the slip process, the compression testing machine was loaded to 2000 kg (load at which first slip band formation occurred in the [126]-oriented crystal) and the compression plate was tapped. The characteristic of the signals generated by taping (machine noise) is different from the acoustic signals collected during the compression test indicating that the signal resulted from the slip band formation.

4.1.5 Magnetostriction Measurement

4.1.5.1 Magnetostriction Measurements in [001]-Oriented Single Crystal

Prior to annealing and deformation of the sample, base-line magnetostriction measurements were performed. Figure 4.13a and 4.13b show magnetostrictive strains $\lambda_{parallel}$ and $\lambda_{perpendicular}$ along the [001] direction versus applied magnetic field curves

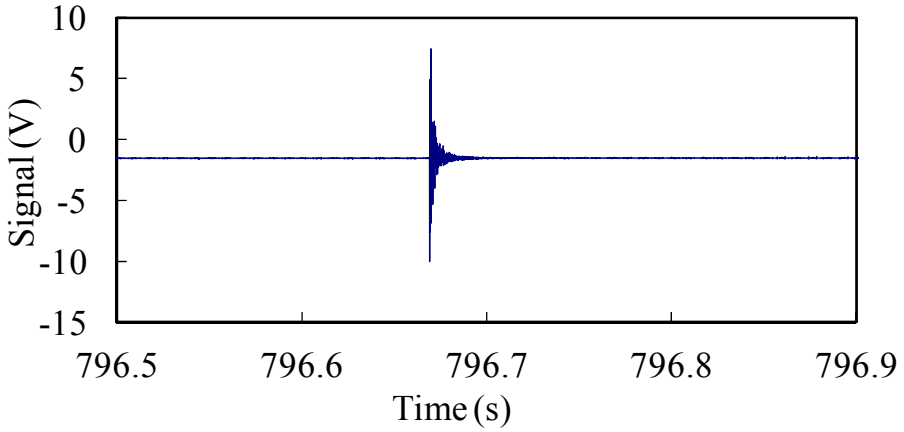

Figure 4.11 Acoustic emission signal collected by the National Instrument data accusation system from one of the emission events during compression test.

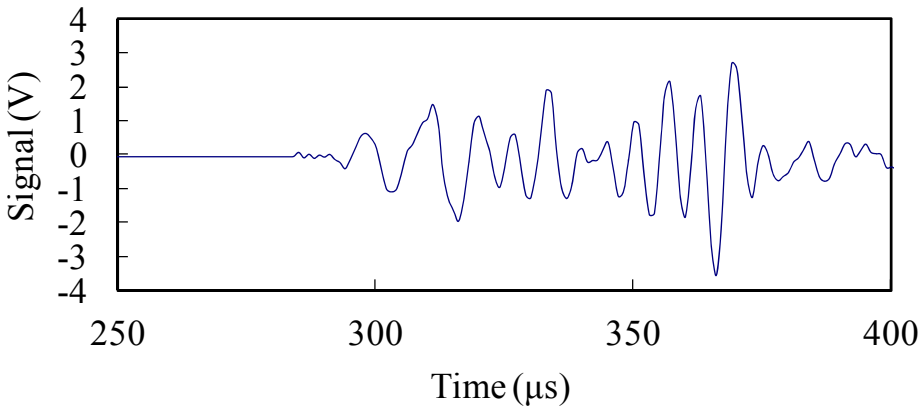

(b)

Figure 4.12 Initial portion of acoustic emission signal captured by oscilloscope.

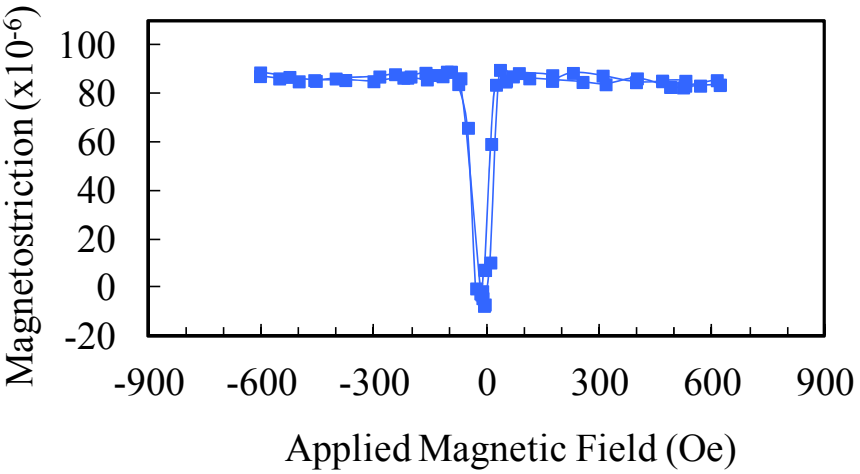

(a)

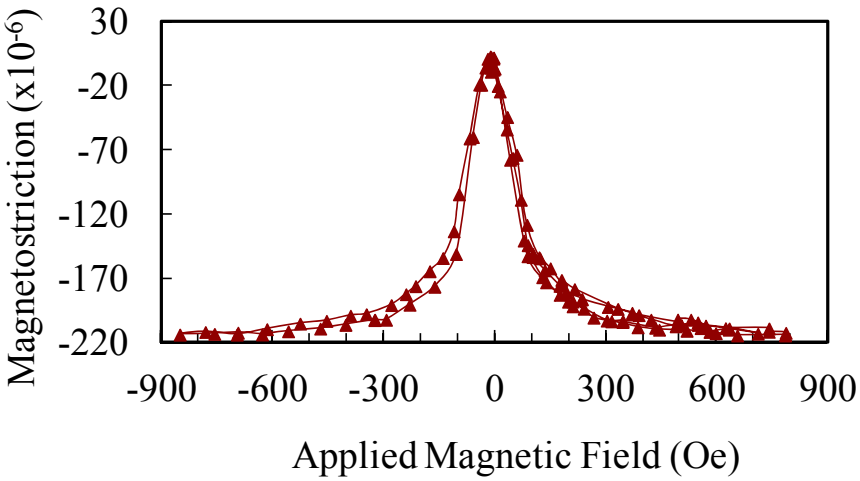

(b)

Figure 4.13 Applied magnetic field vs. magnetostriction in a [001]-oriented Fe-20 at.% Ga single crystal in the as-grown condition; (a) applied magnetic field parallel to [001] direction and (b) applied magnetic field parallel to [010] direction. Strain measured along [001] direction.

with magnetic field applied parallel to [001] and transverse to [001] directions respectively. The ($\lambda_{parallel}$ - $\lambda_{perpendicular}$) gives the (3/2) λ_{100} for the as-grown sample. The (3/2) λ_{100} obtained in this condition was 312 x 10^{-6}. The sample was annealed at 1150 °C for 2 h and the magnetostriction measurements were carried out after this annealing step. Figures 4.14a and 4.14b show magnetostrictive strains $\lambda_{parallel}$ and $\lambda_{perpendicular}$ along the [001] direction versus applied magnetic field curves with magnetic field applied parallel to [001] and transverse to the [001] directions respectively. The (3/2) λ_{100} obtained after the annealing step was 362 x10^{-6}, which is a large enhancement compared to the as-grown condition.

Magnetostriction measurements carried out after the first stage of deformation of [001]-oriented single crystal. The magnetostriction constant (3/2) λ_{100} obtained from strains $\lambda_{parallel}$ and $\lambda_{perpendicular}$ measured along the [001] direction with magnetic field applied parallel to [001] and transverse to [001] directions respectively (Figure 4.15a and 4.15b) after 0.75 % deformation was 355 x 10^{-6}. This is a small reduction from the value obtained in the annealed crystal.

Further compressive deformation was carried out along the [001] direction of the crystal to obtain a total plastic strain level 4.15 % (=0.75% + 3.4%). The engineering stress-strain plot of this compressive deformation is shown in Figure 4.6b. More slip lines were observed on the lateral sample surfaces. Figure 4.16a and 4.16b show magnetostrictive strains $\lambda_{parallel}$ and $\lambda_{perpendicular}$ along [001] direction versus applied magnetic field curves with magnetic field applied parallel to [001] and transverse to [001] directions respectively, for [001]-oriented Fe-20 at.% Ga single crystal after 4.15 % deformation. The (3/2) λ_{100} value obtained after this stage of

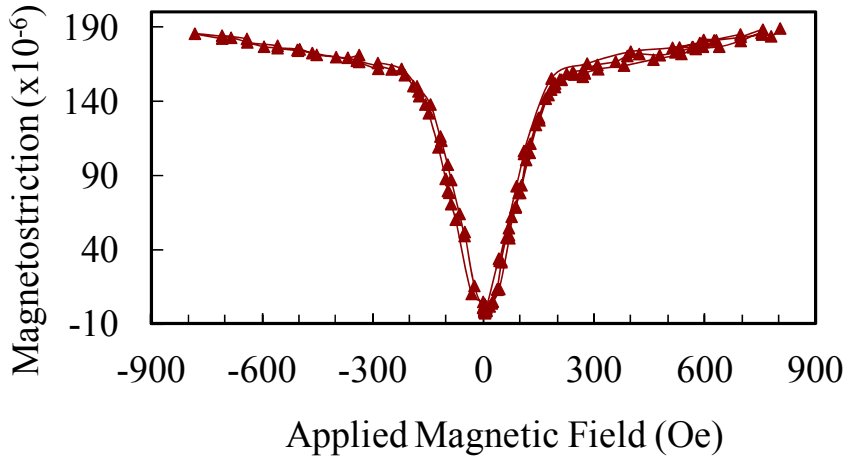

(a)

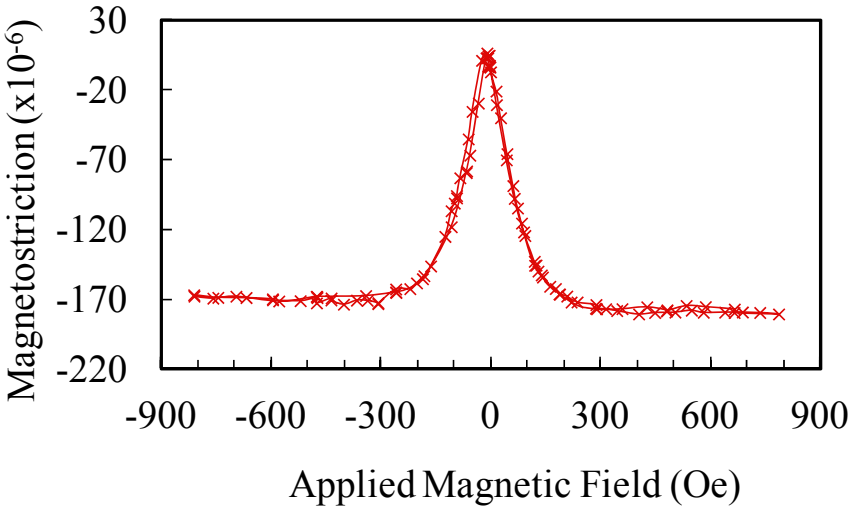

(b)

Figure 4.14 Applied magnetic field vs. magnetostriction in a [001]-oriented Fe-20 at.% Ga single crystal after annealing; (a) applied field parallel to [001] direction and (b) applied magnetic field parallel to [010] direction. Strain measured along [001] direction.

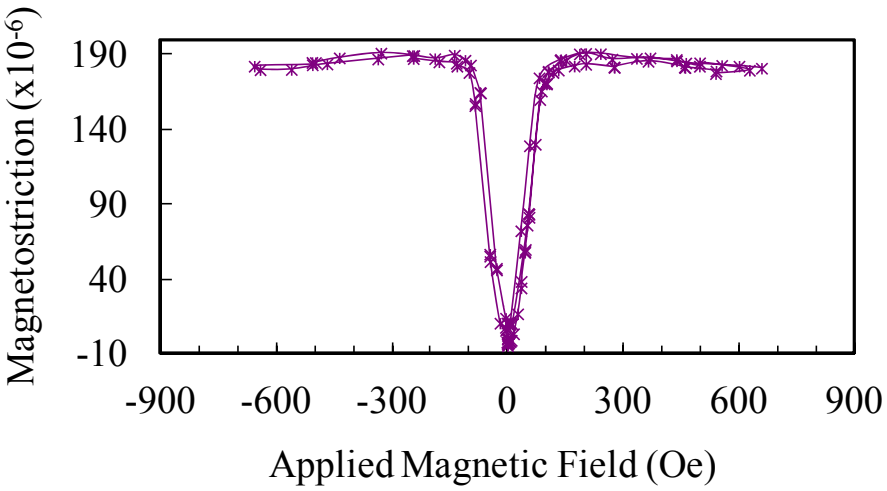

(a)

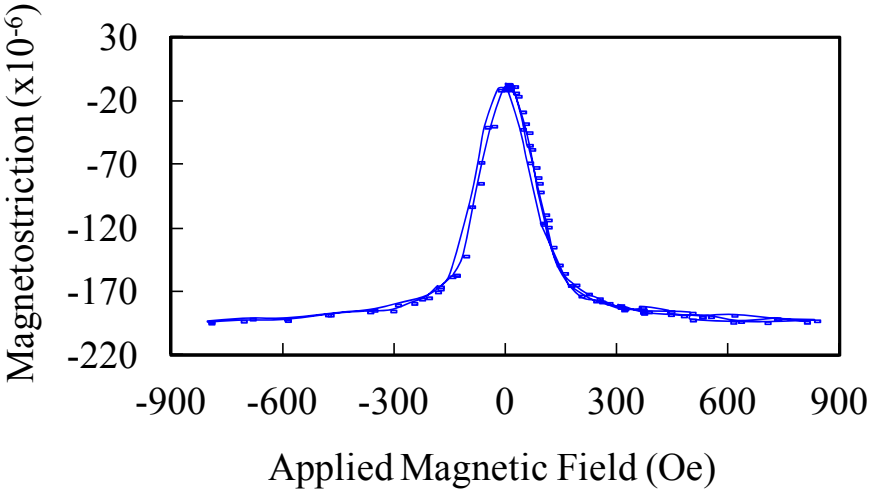

(b)

Figure 4.15 Applied magnetic field vs. magnetostriction in a [001]-oriented Fe-20 at.% Ga single crystal after 0.75% deformation; (a) applied field parallel to [001] direction and (b) applied magnetic field parallel to [010] direction. Strain measured along [001] direction.

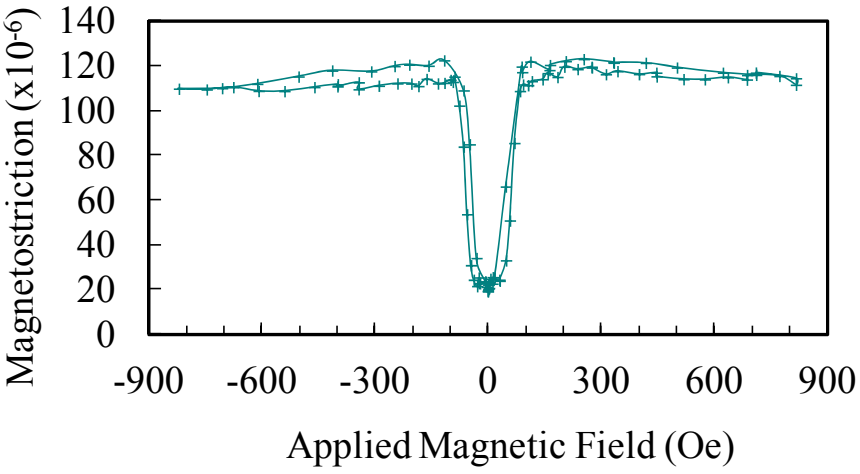

(a)

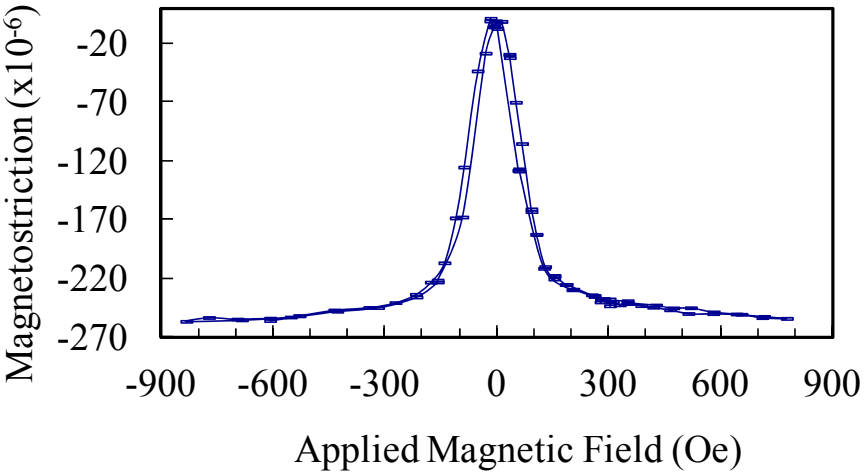

(b)

Figure 4.16 Applied magnetic field vs. magnetostriction in a [001]-oriented Fe-20 at.% Ga single crystal after 4.15% deformation; (a) applied field parallel to [001] direction and (b) applied magnetic field parallel to [010] direction. Strain measured along [001] direction.

deformation was 342 x10^{-6}. This suggests a further reduction in magnetostrictive strain due to increase in the deformation. The changes in magnetostriction after annealing and after deformation are summarized in Figure 4.17.

4.1.5.2 Magnetostriction Measurement in

[126]-Oriented Single Crystal

Prior to annealing and deformation of the sample, base-line magnetostriction measurements were performed on the [126] single crystal in the as-grown condition. Figure 4.18a shows the magnetostrictive strains $\lambda_{parallel}$ ($\lambda_{//}$) measured along the [126] direction as a function of magnetic field applied parallel to [126]. Figure 4.18b shows the magnetostrictive strain $\lambda_{perpendicular}$ ($\lambda_{\perp}$) measured along [126] as a function of magnetic field applied along the $[\overline{20}1\,3]$ transverse direction. The (3/2) λs or ($\lambda_{//} - \lambda_{\perp}$) obtained in this condition was 236 x 10^{-6}.

The sample was annealed at 1150 °C for 2 h and magnetostriction measurements were carried out after this annealing step. Figure 4.19a shows the magnetostrictive strains $\lambda_{parallel}$ ($\lambda_{//}$) measured along the [126] direction in the annealed Fe-20 at.% Ga single crystal as a function of magnetic field applied parallel to [126]. Figure 4.19b shows the magnetostrictive strain $\lambda_{\perp}$ measured along [126] direction as a function of magnetic field applied along $[\overline{20}1\,3]$ transverse direction in the annealed sample. The ($\lambda_{//} - \lambda_{\perp}$) obtained after annealing was 343 x10^{-6}, which is a large enhancement compared to the as-grown condition. This increase is mainly attributed to the homogenization of the alloy.

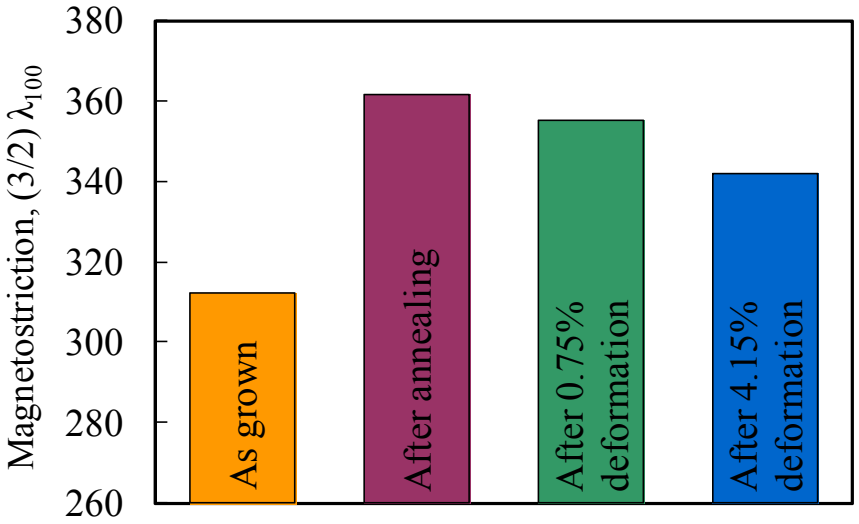

Figure 4.17 Magnetostriction constant (3/2) λ_{100} values plotted as a function of sample history in [001]-oriented Fe-20 at.% Ga single crystals.

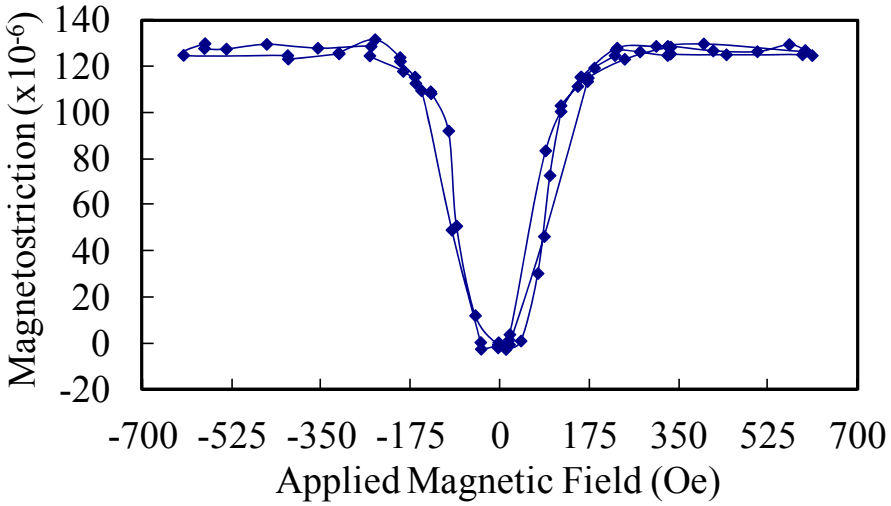

(a)

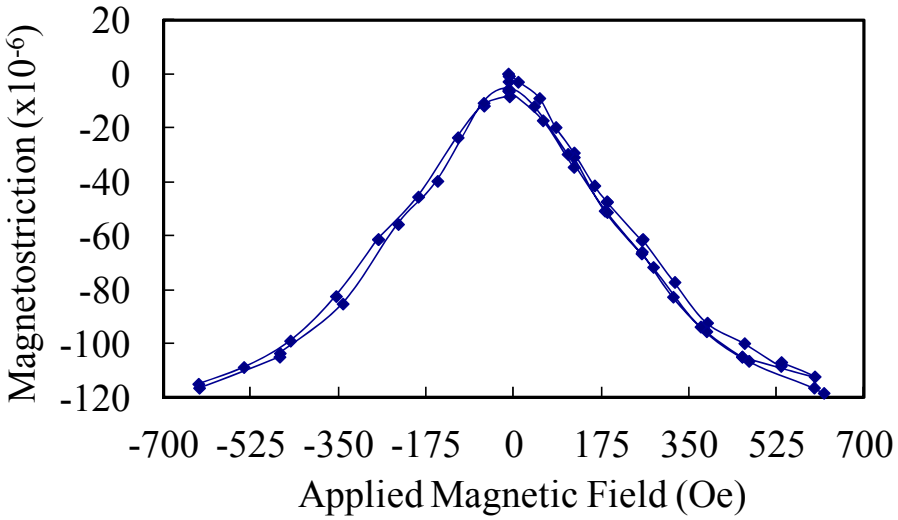

(b)

Figure 4.18 Applied magnetic field vs. magnetostriction in a [126]-oriented Fe -20 at.% Ga single crystal in the as-grown condition (a) magnetostrictive strains $\lambda_{//}$ measured along the [126] direction as a function of magnetic field applied parallel to [126], and (b) magnetostrictive strain $\lambda_{\perp}$ measured along [126] as a function of magnetic field applied along the $[\overline{20}\,1\,3]$ that is transverse to the [126] direction.

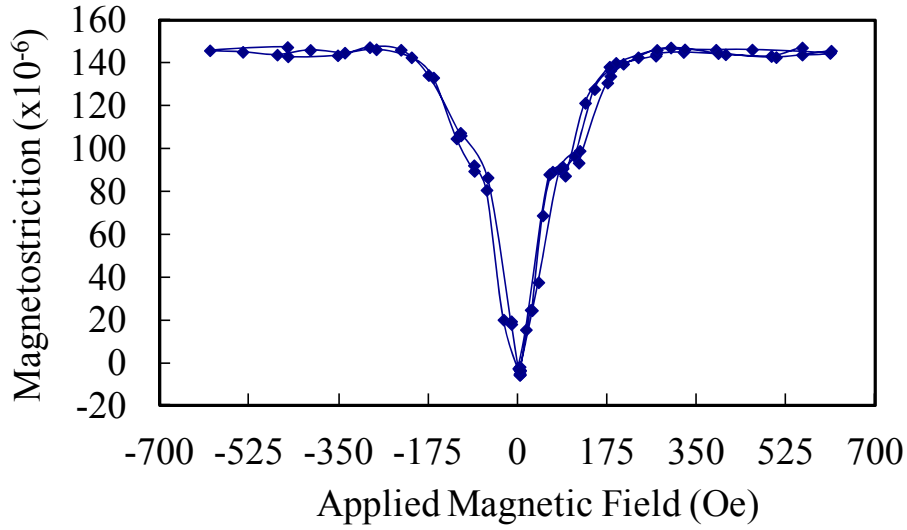

(a)

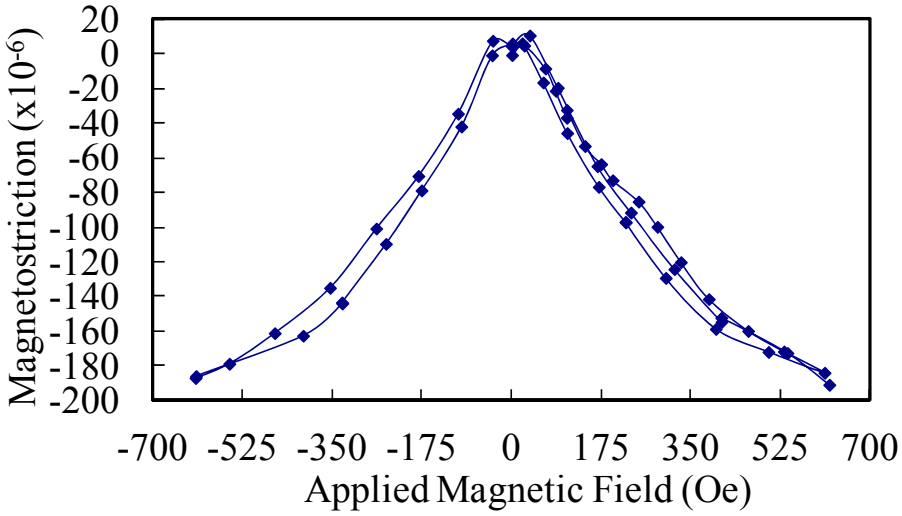

(b)

Figure 4.19 Applied magnetic field vs. magnetostriction in a [126]-oriented Fe -20 at.% Ga single crystal after annealing (a) magnetostrictive strains $\lambda_{//}$ measured along the [126] direction as a function of magnetic field applied parallel to [126], and (b) magnetostrictive strain $\lambda_{\perp}$ measured along [126] as a function of magnetic field applied along the $[\overline{20}13]$ that is transverse to the [126] direction.

The sample was then deformed by compression. Sample was deformed till the first appearance of slip lines as described earlier. Magnetostriction was measured after deformation with strain gage attached on the same face. Figure 4.20a shows the magnetostrictive strains $\lambda_{//}$ measured along the [126] direction as a function of magnetic field applied parallel to [126]. Figure 4.20b shows the magnetostrictive strain $\lambda_{\perp}$ measured along [126] as a function of magnetic field applied along the $[\overline{20}13]$ transverse direction. The $(\lambda_{//} - \lambda_{\perp})$ obtained after the deformation step was 187 $x10^{-6}$, which is a dramatic drop from that obtained in the annealed condition.

A bar chart of $(\lambda_{//} - \lambda_{\perp})$ values as a function of sample history is shown in Figure 4.21. A drastic drop in magnetostriction after only a slight plastic deformation is clearly observed. The dislocation densities in as-grown and annealed single crystals are not expected to be significantly different and well below $10^6/cm^2$. The large enhancement in magnetostriction after the annealing step likely arises from homogenization and stress-relief and minimization of internal stresses arising from ordered second phase regions. The dislocation densities are expected to increase by several orders of magnitude after plastic yielding and further increase with increasing deformation.

A drastic (nearly 50%) drop in magnetostriction is observed in the sample subjected to a small plastic strain caused by slip on only one slip system. The nature of strain modulation introduced by the dislocation arrays formed by the operation of only one slip system will be spatially asymmetric. For example, with the slip planes evenly spaced, the normal stress acting normal to the edge dislocation line and parallel to the slip plane direction will oscillate between tensile and compressive stress as one move along a direction normal to the slip plane. With only a single slip system operating, this

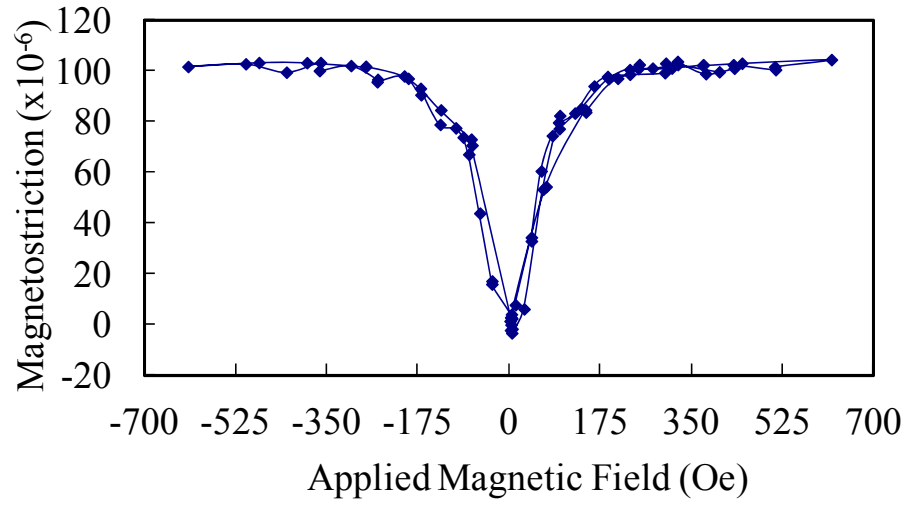

(a)

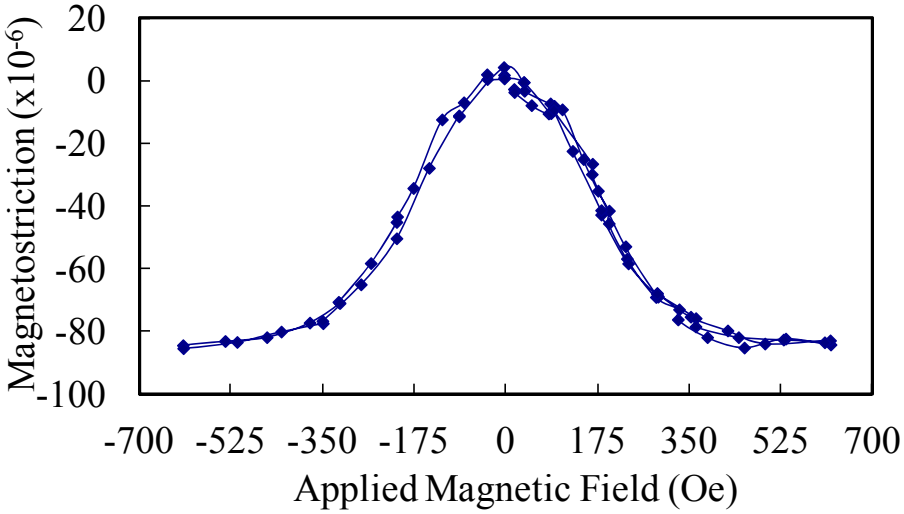

(b)

Figure 4.20 Applied magnetic field vs. magnetostriction in a [126]-oriented Fe-20 at.% Ga single crystal after deformation along [126] direction (a) magnetostrictive strains $\lambda_{//}$ measured along the [126] direction as a function of magnetic field applied parallel to [126], and (b) magnetostrictive strain $\lambda_{\perp}$ measured along [126] as a function of magnetic field applied along the $[\overline{20}\,1\,3]$ that is transverse to the [126] direction.

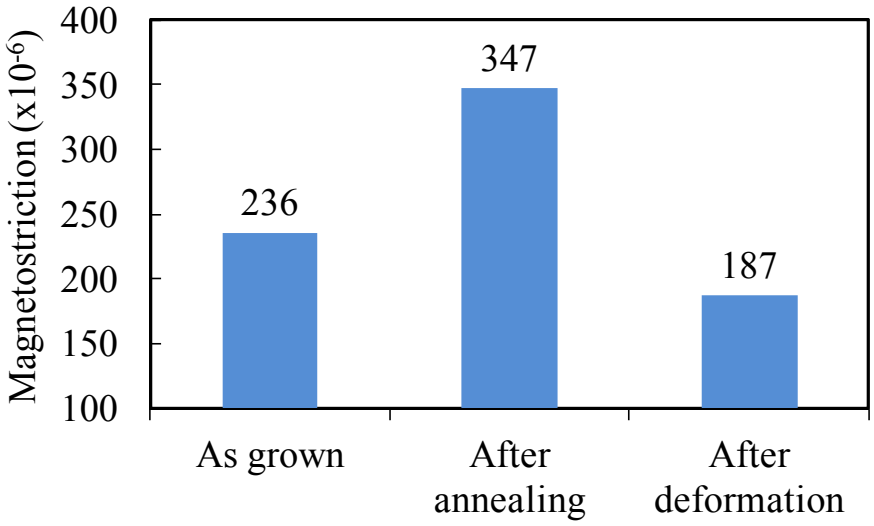

Figure 4.21 Magnetostriction (3/2) λ_s in [126]-oriented Fe-20 at.% Ga single crystal as a function of sample history.

oscillatory stress with wavelength equal to the slip plane spacing will have a finite oscillatory stress component along the [001] crystal direction. The strain modulates the local atomic spacing and it could be the origin of the strong influence on magnetostriction as the magnetoelastic coupling in the lattice depends on the interatomic spacing. In contrast, in the case of deformation along [001] direction in a [001]-oriented crystal, the drop in magnetostriction even after a much larger deformation is relatively small as shown in Figure 4.17. The engineering stress versus strain plot and the slip line patterns observed are shown in Figure 4.6. In this case, eight different slip systems were operative during deformation, and the nature of defect distribution is highly symmetric.

Magnetostriction measurements were also made by attaching strain gages along a $[0\,3\,\bar{1}]$ direction transverse to [126] direction (Figure 3.7b). As mentioned earlier in the case of strain gage attached along the longitudinal [126] direction the magnetostriction value measured increased after annealing and decreased sharply after deformation. However, in the case of strain gage attached along the transverse direction (perpendicular to previous measurement direction) the measured saturation magnetostrictive strain value shows an increase after deformation from a value of 257 x 10^{-6} to 297 x 10^{-6}. This is consistent with the anisotropic nature of strain modulation generated after deformation.

The results suggest that besides dislocation density, the nature of strain modulation introduced by the dislocation arrays has a strong influence on the magnetostrictive behavior of magnetostrictive alloys. TEM analyses of structure before and after deformation using a second sample are presented in the next section.

4.1.6 TEM Examination of Annealed and Deformed Fe-Ga Samples

As the samples needed for TEM examination would destroy the sample on which magnetostriction measurements were made, a second set of Fe-20 at.% Ga single crystal samples deformed along [001] and [126] directions were prepared. For reference, [001]-oriented as-annealed Fe-20 at.% Ga single crystal sample was used. TEM examination of the Fe-20 at.% Ga long term annealed (LTA) sample, and deformed [001]-oriented and [126]-oriented Fe-20 at.% Ga samples were carried out at the Electron Microscopy Center at Argonne National Laboratory using a TECNAI F20 sTEM.

Figure 4.22 shows the TEM bright field image of Fe-20 at.% Ga LTA sample and the diffraction pattern of the same area is shown in Figure 4.23. Image contains bend contours and thickness fringes. But no dislocations were seen in the sample. Based on the x-ray diffraction studies in Fe-Ga alloys, nanoscale coherent second phase regions are expected in this alloy sample. However, due to the strong ferromagnetic nature of the sample and relatively larger sample thickness in the regions, resolution needed for lattice imaging of these nanoscale coherent regions could not obtained during this study. This will be attempted again after preparing better samples.

TEM samples prepared from a second [001]-oriented Fe-20 at.% Ga crystal deformed to ~4% plastic strain (about same as the first crystal) was examined next. This sample was expected to show slip occurring on multiple slip system. Figure 4.24 shows bright field transmission electron microscopy image. Figure 4.25 shows diffraction pattern of the same area with (001) zone axis. Figure 4.24 clearly shows that several slip

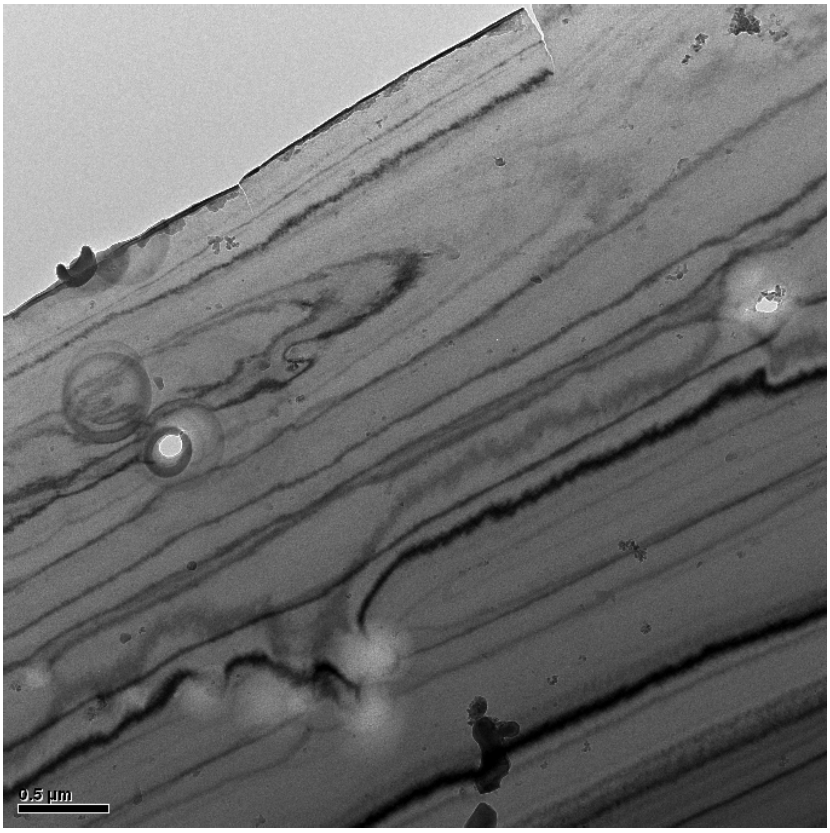

Figure 4.22 Bright-field TEM image of Fe-20 at.% Ga LTA sample.

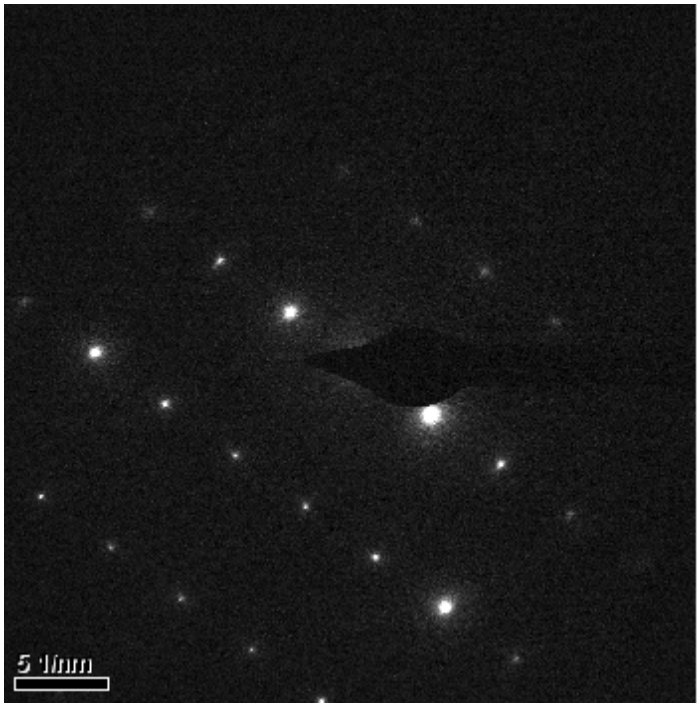

Figure 4.23 Selected area diffraction pattern of Fe-20 at.% Ga LTA sample with (001) zone axis.

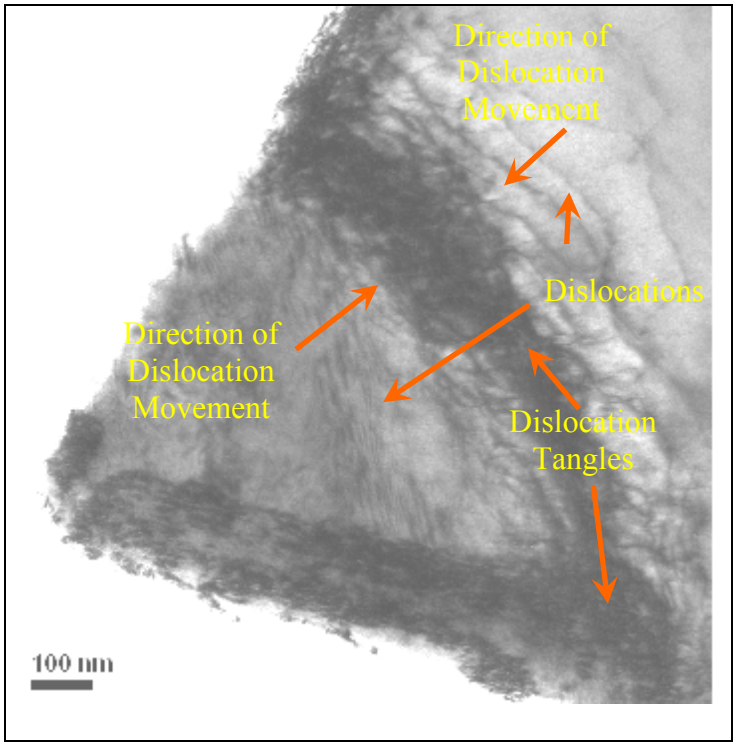

Figure 4.24 Bright-field TEM image of Fe-20 at.% Ga [001]-oriented plastically deformed sample.

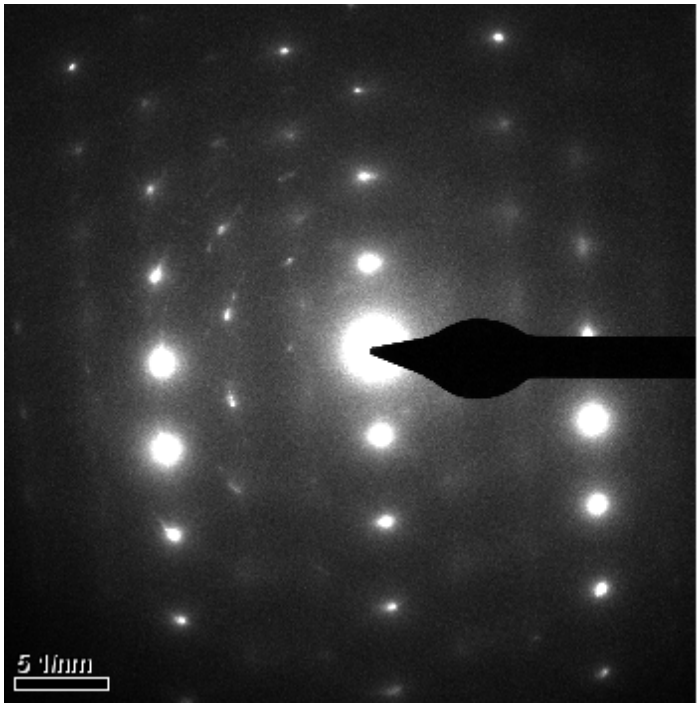

Figure 4.25 Selected area diffraction pattern of TEM bright field image of Fe-20 at.% Ga [001]-oriented plastically deformed sample with (001) zone axis.

systems were operational during the deformation process as expected. Dislocation arrays on different slip planes are visible in Figure 4.24. Intersection of dislocations moving on these slip planes and forming dislocation tangles are clearly seen in this figure.

A bright field TEM image of [126]-oriented sample plastically deformed to 1 % strain is shown in Figure 4.26 and the diffraction pattern of the same area with (001) zone axis is shown in Figure 4.27. Figure 4.26 shows single set of dislocation arrays illustrative of operation of only one slip system. This image also shows some contrasts due to the bend and thickness contours. Burgers vector for the [126]-oriented deformed sample could not be calculated due to the limitation of tilting of the TEM sample in the microscope. To calculate the Burgers vector the images had to be take using different zone axes. The (011) is ~27° off from the (126) plane and rotating the magnetic sample more than 20° was not recommended in the TECNAI F20.

4.2 Effect of Mo on Magnetostriction of Fe

4.2.1 Orientation of [001] Single Crystal Samples

The θ-2 θ scan for Fe-5 at.% Mo is shown in Figure 4.28. The 2 θ value obtained from θ-2 θ scan for (200) peak is 64.66° for Fe-5 at.% Mo. The (200) rocking curve x-ray diffraction scans were obtained from all the six faces. Figure 4.29 shows the rocking curve scan obtained from one of the sample faces of Fe-5 at.% Mo. For the rocking curve scan, the detector was fixed at 2 θ = 64.66° with respect to the source and the sample was rotated about the diffractometer axis with the angle between the sample surface and the incident beam indicated by the symbol ω. The intensity peak in the

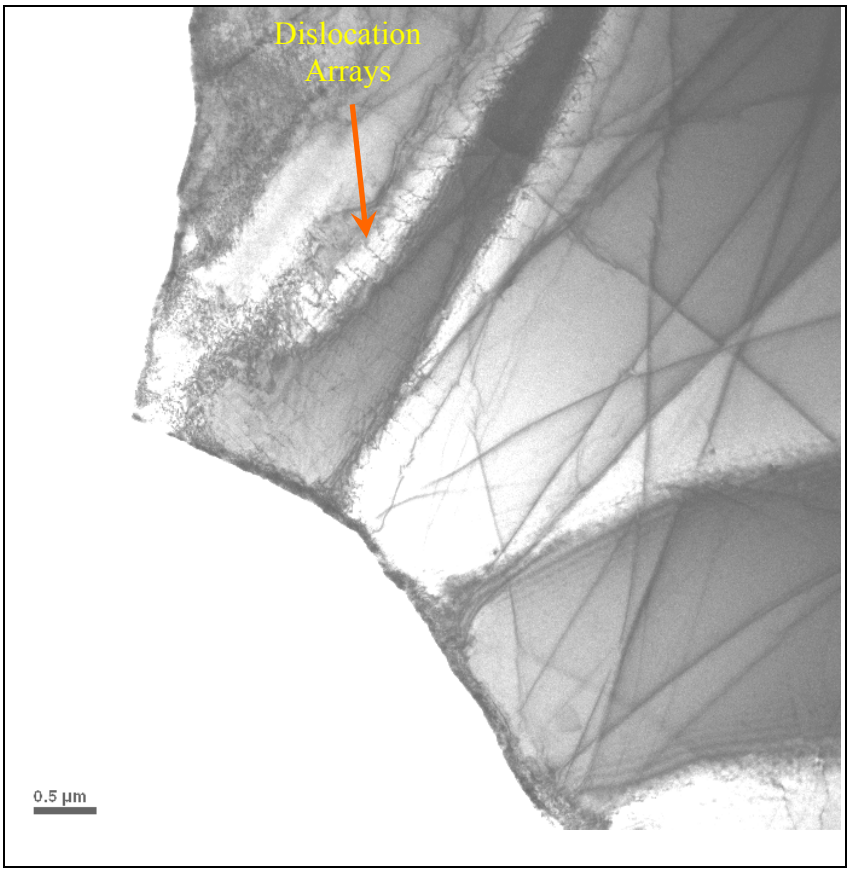

Figure 4.26 Bright-field TEM image of Fe-20 at.% Ga [126]-oriented plastically deformed sample showing slip on only one slip system.

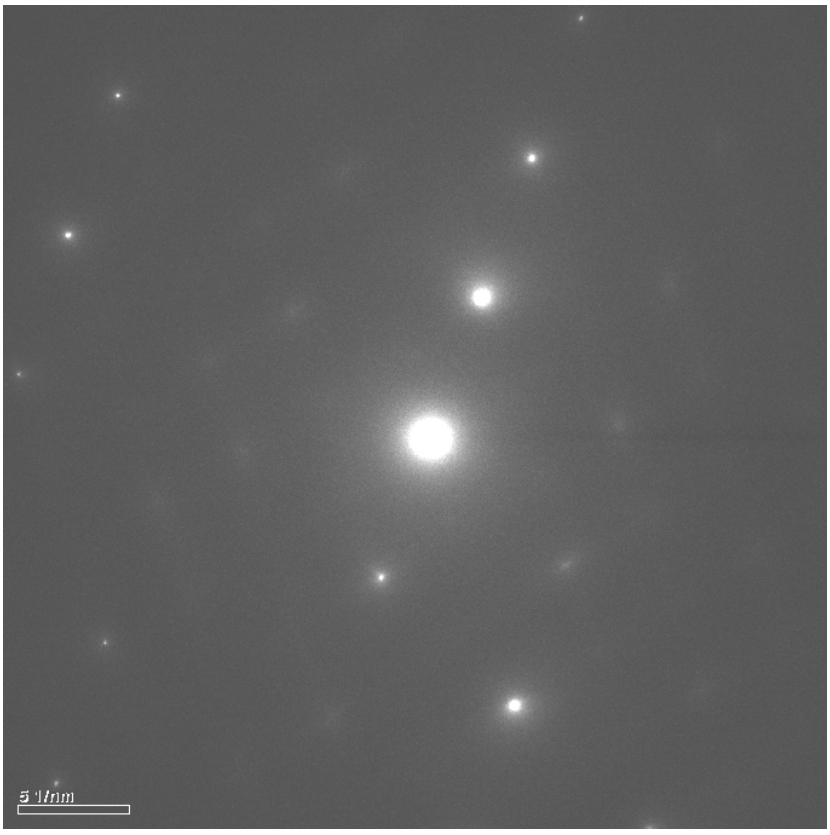

Figure 4.27 Selected area diffraction pattern of Fe-20 at.% Ga [126]-oriented plastically deformed sample corresponding to the area shown in Figure 4.26.

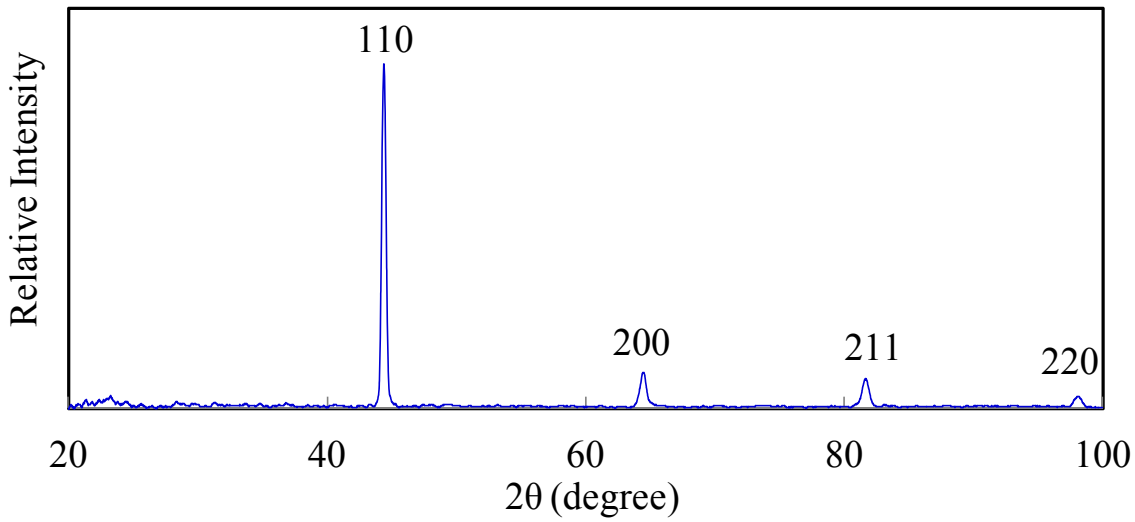

Figure 4.28 X-ray diffraction pattern of Fe-5 at.% Mo directionally grown single crystal.

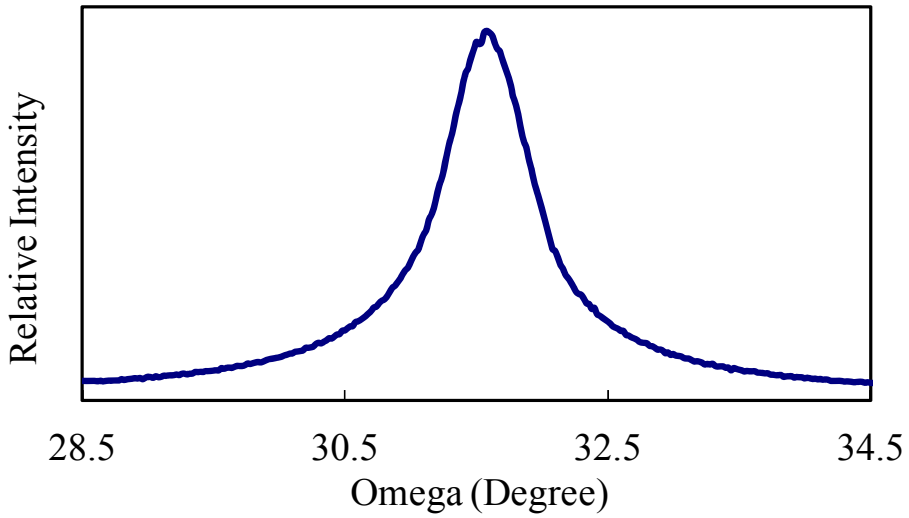

Figure 4.29 Rocking curve scan for one of the six-faces for Fe-5 at.% Mo single crystal.

(002) rocking curve scan intensity indicates the position of the sample surface for which (002) plane of the sample satisfies the Bragg condition and the (θ-ω) is the deviation of the sample surface normal from <001> direction. The ω value for the peak in the plot is 31.96 suggesting the scanned sample surface normal deviation of 0.37 degree from the <100> direction. All other faces were also oriented to well within 0.5 degree from the <100> direction.

The θ-2 θ scan for Fe-10 at.% Mo is shown in Figure 4.30 and (002) rocking curve scan for one of the faces is shown in Figure 4.31. In this case, the 2 θ value is 64.28° and ω is 31.92°. That gives a (θ-ω) value of 0.22°. This suggests that the scanned face is 0.22° from the <100> direction. All the other faces were also polished to within 0.5° from the nearest <100> direction.

In a similar way, orientation of [001] Fe-20 at.% Mo single crystal sample was determined. The θ-2 θ scan for this sample is shown in Figure 4.32. All the faces are polished to within 0.5° from <100> direction.

4.2.2 Orientation of Single Crystal Samples for λ_{111} Measurement

The (211) crystal face of a bcc crystal contains [111] and [220] crystal directions. For Fe-5 at.% Mo and Fe-20 at.% Mo single crystal samples, single crystals with (211) orientation were first cut followed by cutting and polishing of the {220} and {111} faces normal to the (211) face. The (220) and (211) rocking curve scans were obtained from all the six faces of the single crystal samples for λ_{111} measurement to ensure that the crystal faces were well within 1 degree from the desired orientation. The

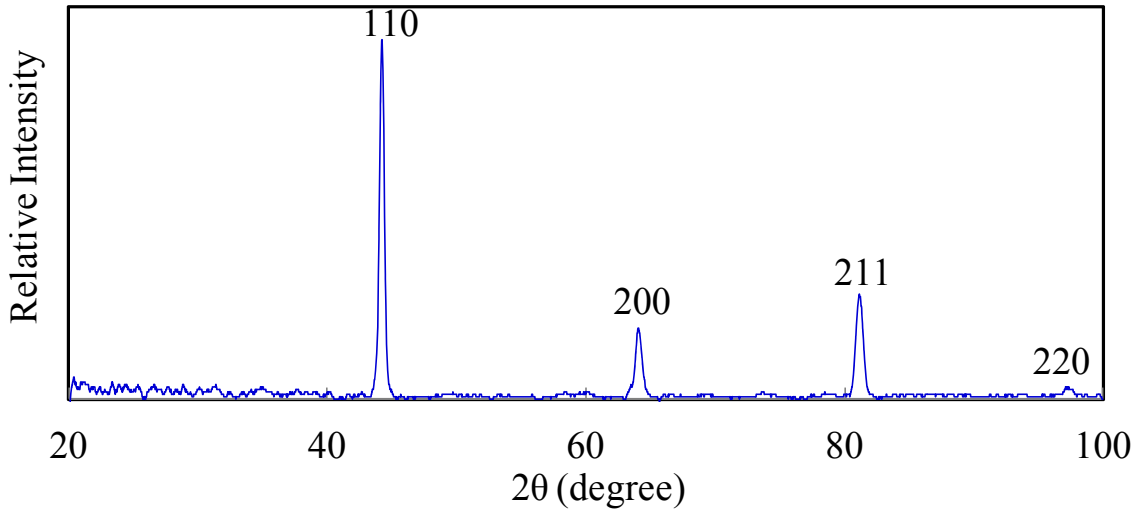

Figure 4.30 X-ray diffraction pattern of Fe-10 at.% Mo directionally grown single crystal.

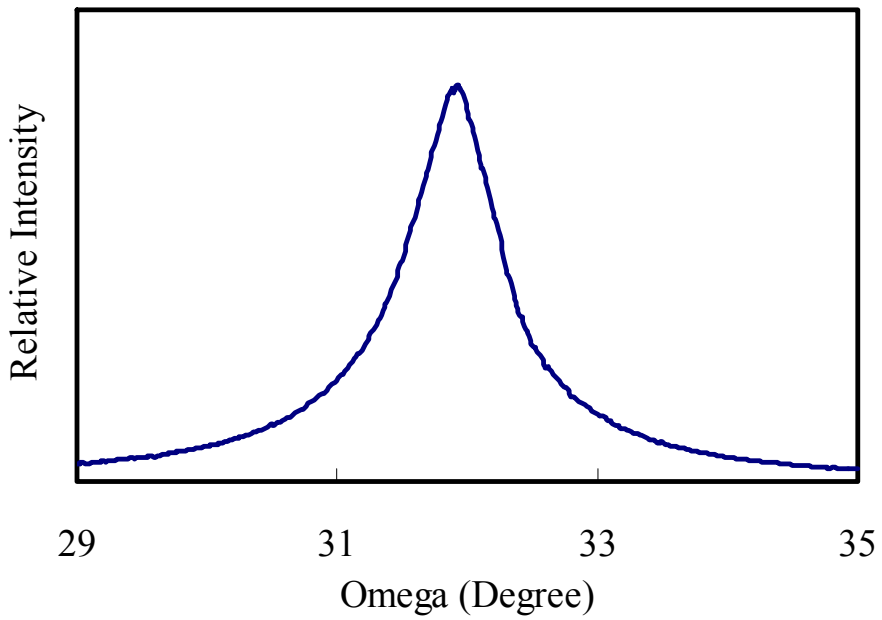

Figure 4.31 Rocking curve scan for one of the six-faces for Fe-10 at.% Mo single crystal.

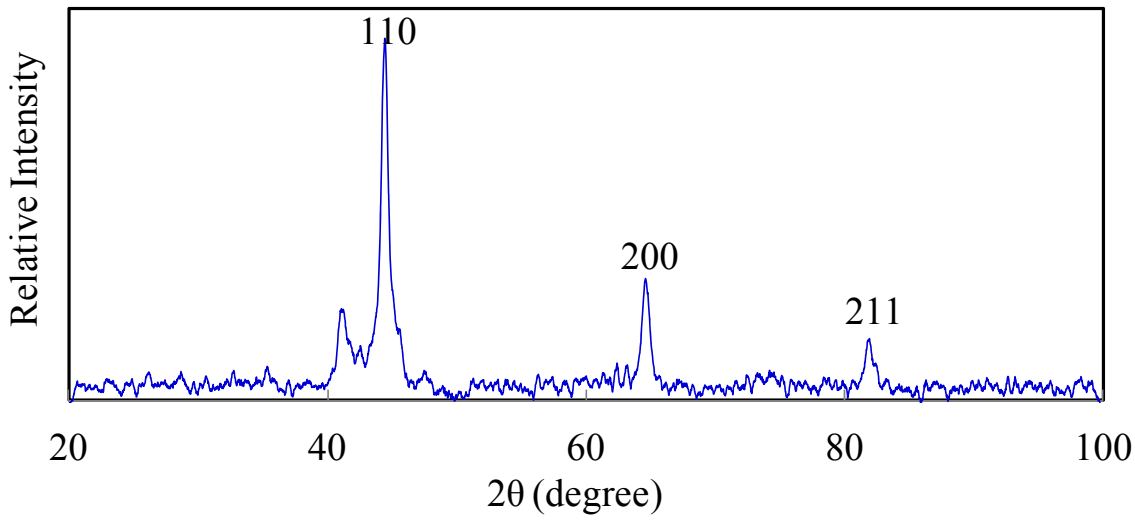

Figure 4.32 X-ray diffraction pattern of Fe-20 at.% Mo directionally grown single crystal.

2 θ value obtained from θ-2 θ scan for the (211) peak is 81.79 for Fe-5 at.% Mo. Figure 4.33 shows the rocking curve scan obtained from one of the sample faces of Fe-5 at.% Mo. For the rocking curve scan, the detector was fixed at 2 θ = 81.79° with respect to the source and the sample was rotated about the diffractometer axis with the angle between the sample surface and the incident beam indicated by the symbol ω. The intensity peak in the (211) rocking curve scan indicates the angular position of the sample surface for which (211) plane of the sample satisfies the Bragg condition and the (θ-ω) is the deviation of the sample surface normal from <211> direction. The ω value for the peak in the plot is 40.73 suggesting the scanned sample surface normal deviation of 0.17° from the nearest <211> direction. A (310) rocking curve scan was also carried out and the sample surface normal was determined to be 24.97° away from the nearest <310>.

Using both (211) and (310) orientation data, crystal orientation was completely characterized and the orientation of (111) plane and the [111] direction on the (211) face were determined. Figure 4.34 shows the pole figure corresponding to [111]-oriented face of Fe-5 at.% Mo sample based on the orientation data, and this indicates that the sample face is less than 1° from the nearest <111>. The face perpendicular to the (211) and (111) is (220). These faces were also polished to within 0.5° from <220> direction.

For the Fe-10 at.% Mo single crystal sample, single crystal with (220) orientation was first cut followed by cutting and polishing of the {211} and {111} faces normal to the (220) face. The θ-2 θ scan for Fe-10 at.% Mo alloy sample (Figure 4.30) shows that the 2 θ value for the (220) peak is 97.44°. The detector was fixed at the 2 θ

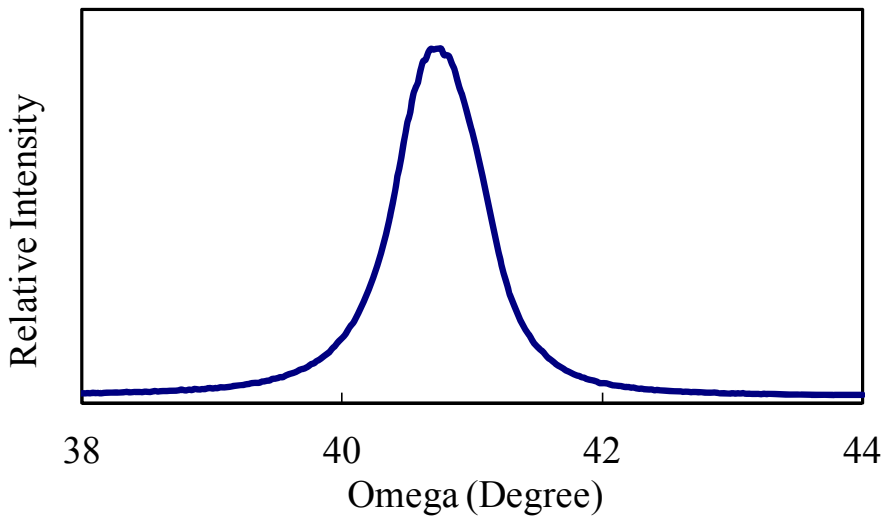

Figure 4.33 Rocking curve scan for [211]-oriented face of the Fe-5 at.% Mo single crystal.

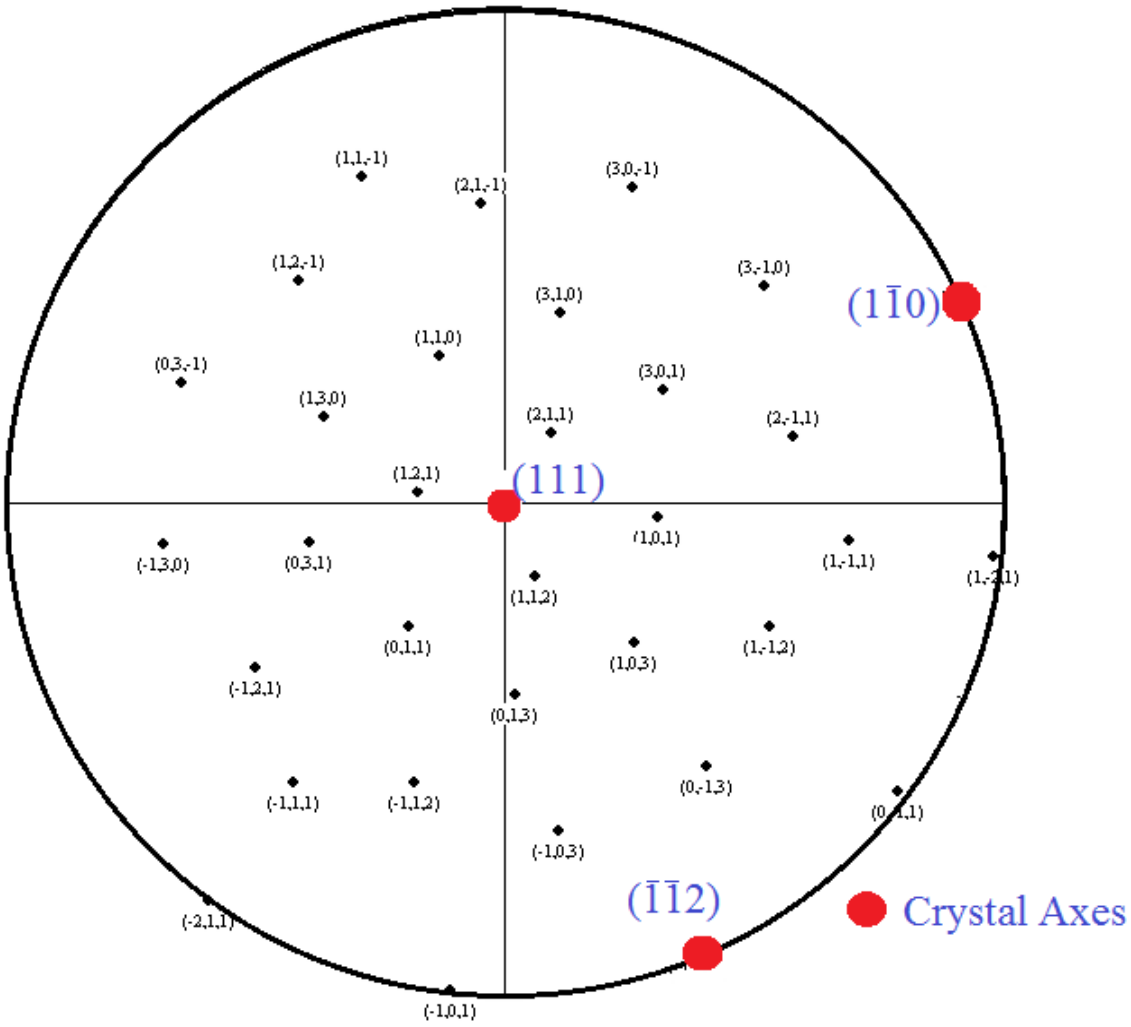

Figure 4.34 Pole figure illustrating the directions in the plane (around the perimeter) and normal to (at the center) [111]-oriented faces of Fe-5 at.% Mo single crystal.

value and (220) rocking curve scan was done. The (220) rocking curve scan for one of the faces is shown in Figure 4.35. The ω value is 48.68° that gives that (θ-ω) = 0.04°. This suggests that the scanned face is within 0.04° from the <220> direction. The (310) rocking curve scan was also done and the direction of {111} planes was determined. The [111]-oriented faces were polished with in 1° from the <111> direction. The pole figure for [111]-oriented Fe-10 at.% Mo single crystal sample is similar as that of Fe-5 at.% Mo sample (shown in Figure 4.34). The other face perpendicular to the (220) and (111) is (211). The (211) faces were also polished to within 0.5° from <211> direction.

The [211]-oriented Fe-20 at.% Mo sample was prepared in a similar way as Fe-5 at.% Mo sample. This crystal had [211]-oriented big faces and the two perpendicular faces are oriented in the [220] and [111] directions. The (211) rocking curve scan is shown in Figure 4.36. This figure indicates that the scanned face is 0.06° off from the nearest <211> direction.

4.2.3 Magnetostriction Measurement

4.2.3.1 λ_{100} Measurement

Prior to annealing the sample base-line magnetostriction measurements were performed in oriented Fe-5 at.%, Fe-10 at.% and Fe-20 at.% single samples. The ($\lambda_{parallel}$ - $\lambda_{perpendicular}$) gives the (3/2) λ_{100} for the as-grown sample. The samples were then annealed at various temperatures (Chapter 3, Table 3.1) in the α-phase region for 2 h and the magnetostriction measurements were carried out after this annealing step.

Figure 4.37 shows the (a) $\lambda_{parallel}$ and (b) $\lambda_{perpendicular}$ measurements for the as-grown Fe-5 at.% Mo. In this condition, (3/2) λ_{100} for Fe-5 at.% Mo is 112 x 10^{-6}. After

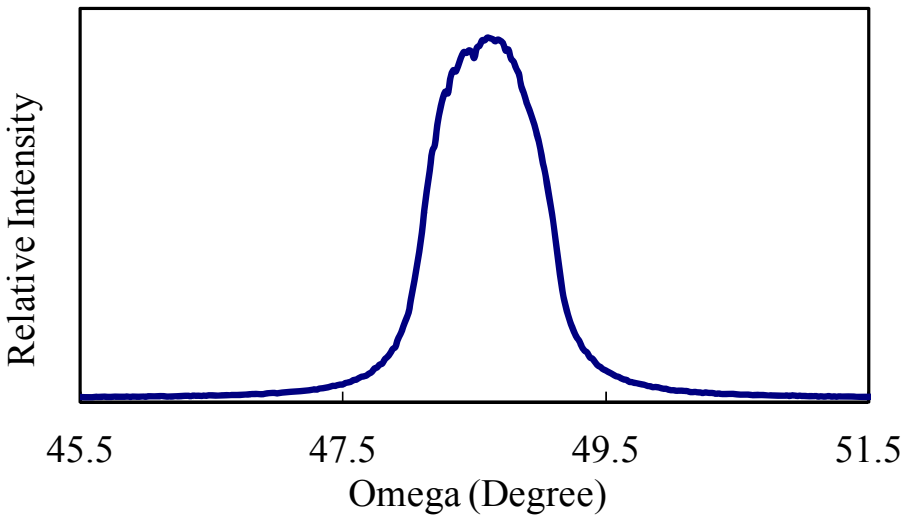

Figure 4.35 Rocking curve scan for [220]-oriented face of the Fe-10 at.% Mo single crystal.

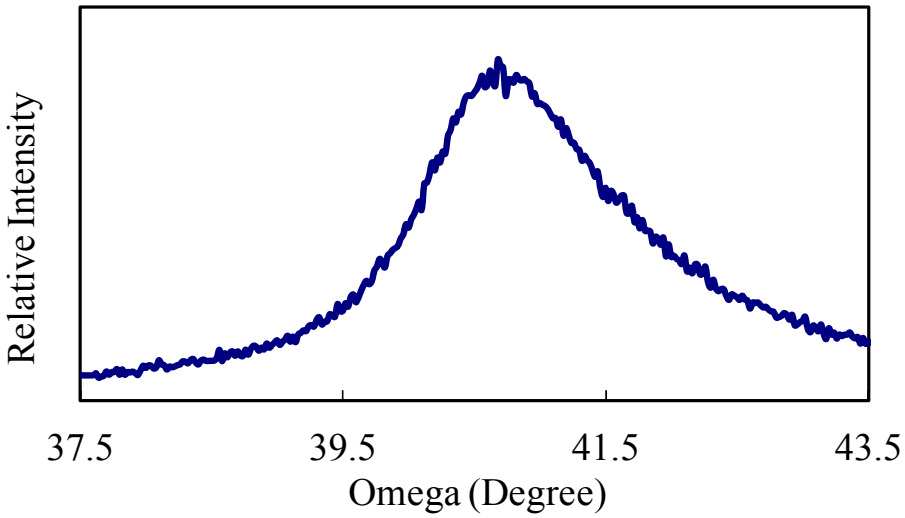

Figure 4.36 Rocking curve scan for [211]-oriented face of the Fe-20 at.% Mo single crystal.

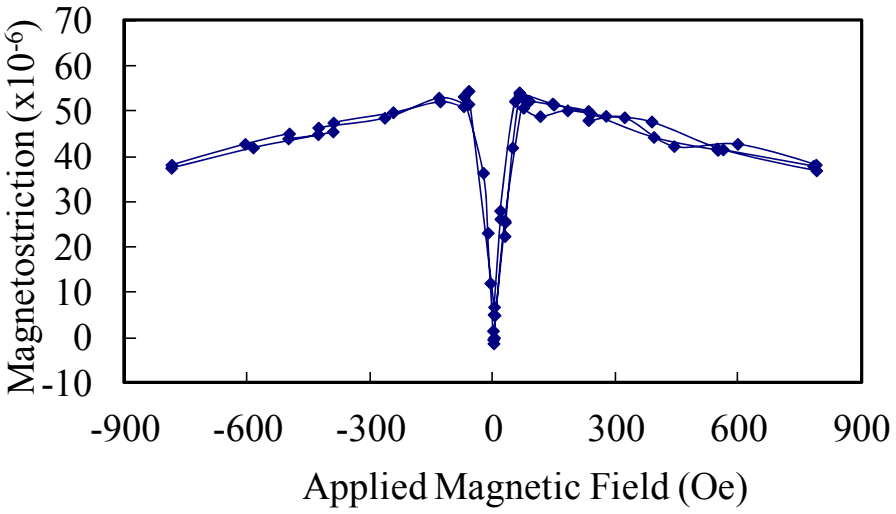

(a)

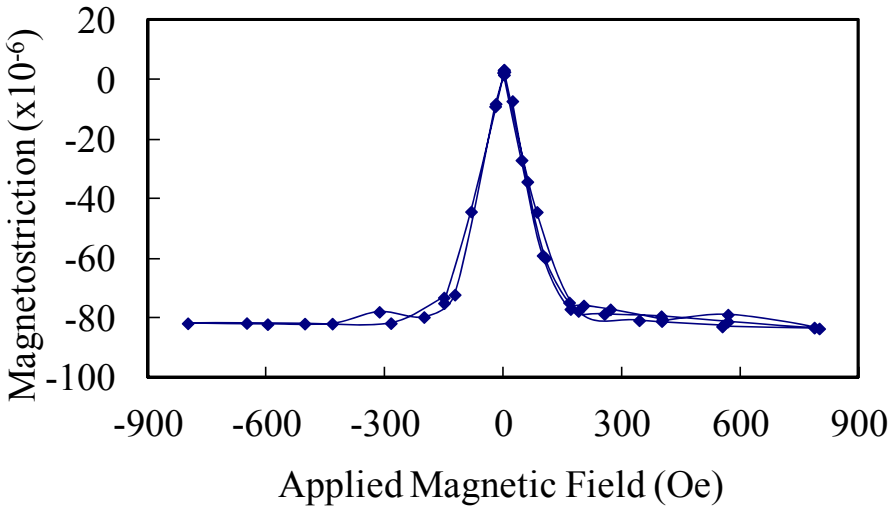

(b)

Figure 4.37 Applied magnetic field vs. magnetostriction in a [001]-oriented Fe-5 at.% Mo single crystal in as-grown condition; (a) applied field parallel to [001] direction and (b) applied magnetic field parallel to [010] direction. Strain measured along [001] direction.

annealing there is no change in the (3/2) λ_{100} for Fe-5 at.% Mo as shown in Figure 4.38. This is due to lesser propensity of this alloy to form a second phase on cooling.

Figure 4.39 shows the (a) $\lambda_{parallel}$ and (b) $\lambda_{perpendicular}$ measurements for the as-grown Fe-10 at.% Mo. In the as-grown condition, the (3/2) λ_{100} for Fe-10 at.% Mo is 108 x 10^{-6}. Figure 4.40a shows the $\lambda_{parallel}$ and 4.40b shows the $\lambda_{perpendicular}$ measurements after annealing. The difference between the two gives the (3/2) $\lambda_{100.}$ After annealing (3/2) λ_{100} for Fe-10 at.% Mo is 137 x 10^{-6}. This is also the highest reported magnetostriction value among all Fe-Mo alloys.

Figure 4.41a shows the $\lambda_{parallel}$ and 4.41b shows the $\lambda_{perpendicular}$ measurement for the Fe-20 at.% Mo as-grown single crystal sample. The (3/2) λ_{100} for this alloy in the as-grown condition is 53 x10^{-6}. After annealing, the value increased to 110 x10^{-6} (Figure 4.42). This large enhancement in magnetostriction can be attributed to homogenization and stress-relief and minimization of internal stresses arising from ordered second phase.

The (3/2) λ_{100} obtained for Fe-Mo samples in the as-grown and annealed conditions are shown in Table 4.4. The values obtained after annealing are shown in Figure 4.43. There is a rapid increase in magnetostriction with Mo addition till 10 at.%. The rate of increment is high till 5 at.% and then it decreases. With Mo additions to Fe above 10 at.%, the magnetostriction value decreases slowly. At higher Mo contents, the propensity for the formation of a second phase is increased. Presence of a second phase creates strain in the lattice and decrease magnetostriction after 10 at.% Mo.

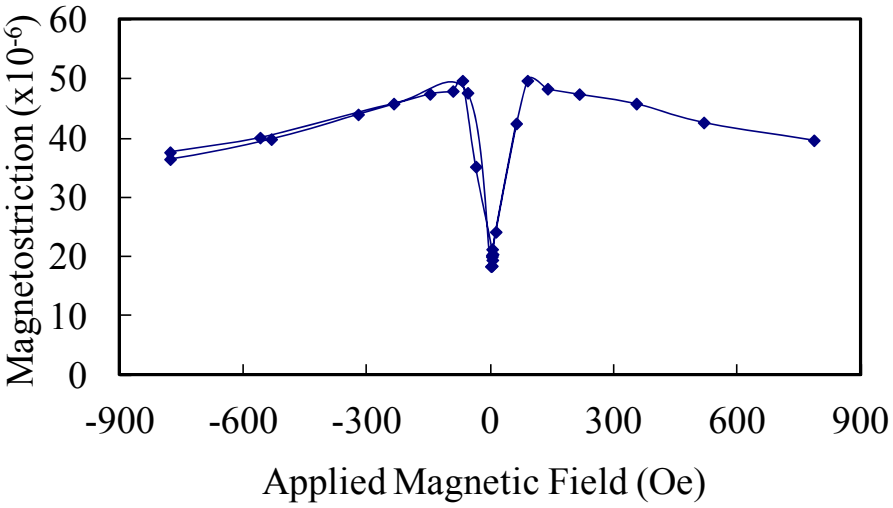

(a)

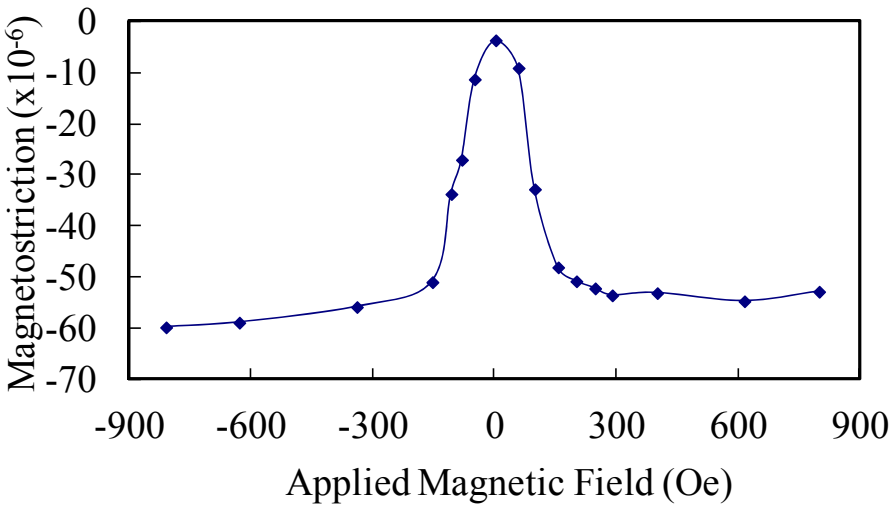

(b)

Figure 4.38 Applied magnetic field vs. magnetostriction in a [001]-oriented Fe-5 at.% Mo single crystal in after annealing treatment; (a) applied field parallel to [001] direction and (b) applied magnetic field parallel to [010] direction. Strain measured along [001] direction.

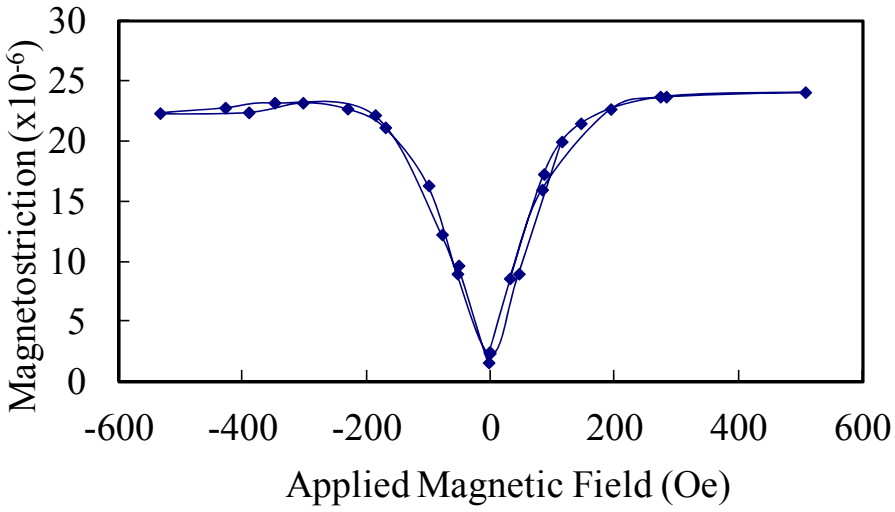

(a)

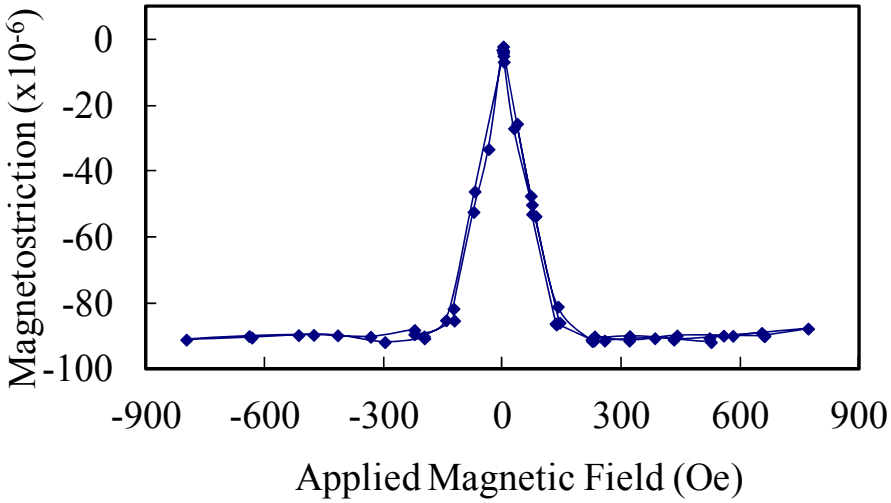

(b)

Figure 4.39 Applied magnetic field vs. magnetostriction in a [001]-oriented Fe-10 at.% Mo single crystal in as-grown condition; (a) applied field parallel to [001] direction and (b) applied magnetic field parallel to [010] direction. Strain measured along [001] direction.

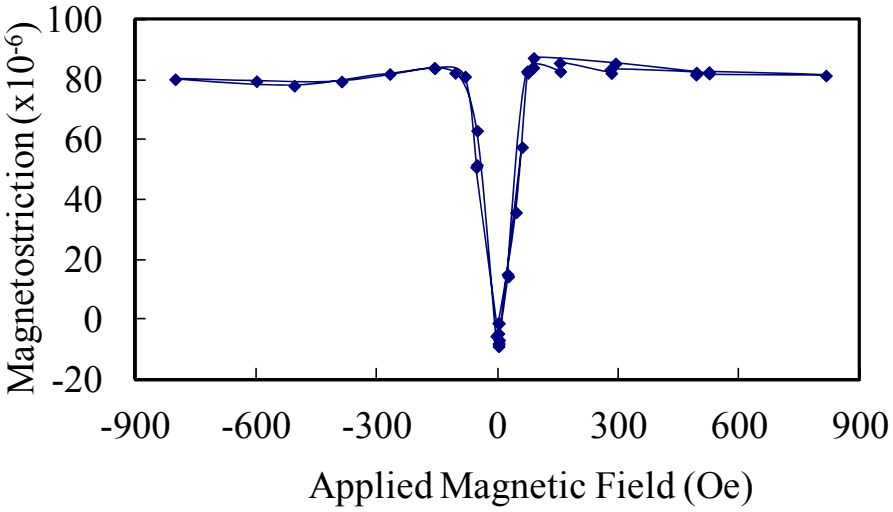

(a)

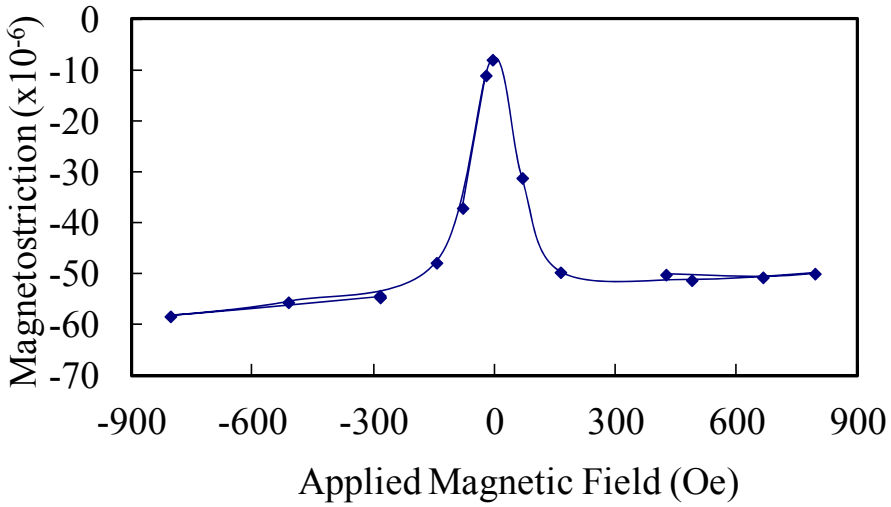

(b)

Figure 4.40 Applied magnetic field vs. magnetostriction in a [001]-oriented Fe-10 at.% Mo single crystal in after annealing treatment; (a) applied field parallel to [001] direction and (b) applied magnetic field parallel to [010] direction. Strain measured along [001] direction.

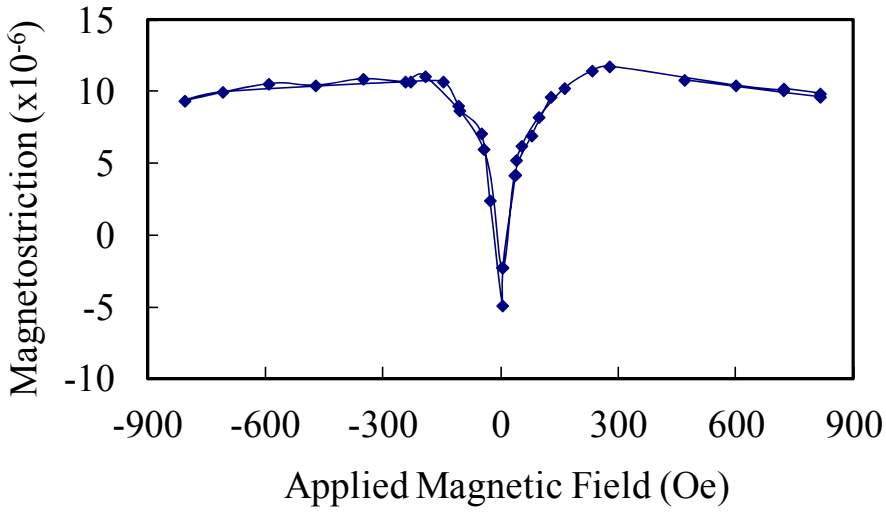

(a)

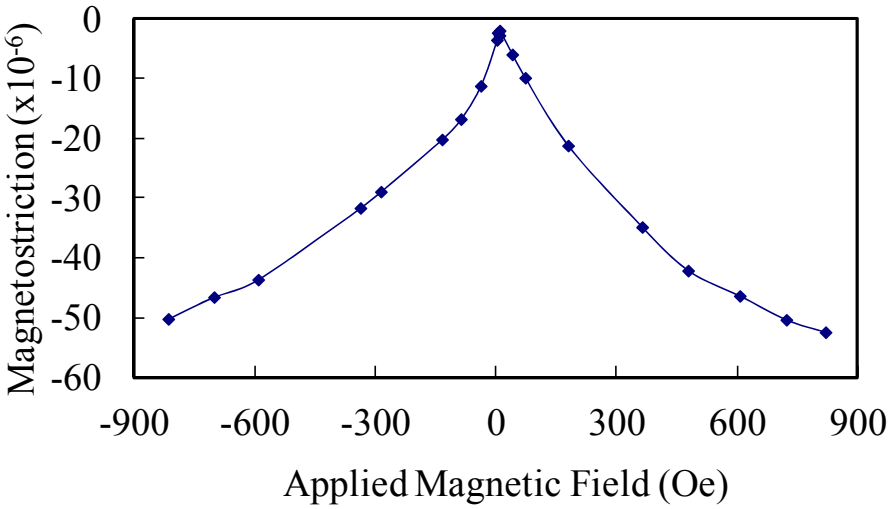

(b)

Figure 4.41 Applied magnetic field vs. magnetostriction in a [001]-oriented Fe-20 at.% Mo single crystal in as-grown condition; (a) applied field parallel to [001] direction and (b) applied magnetic field parallel to [010] direction. Strain measured along [001] direction.

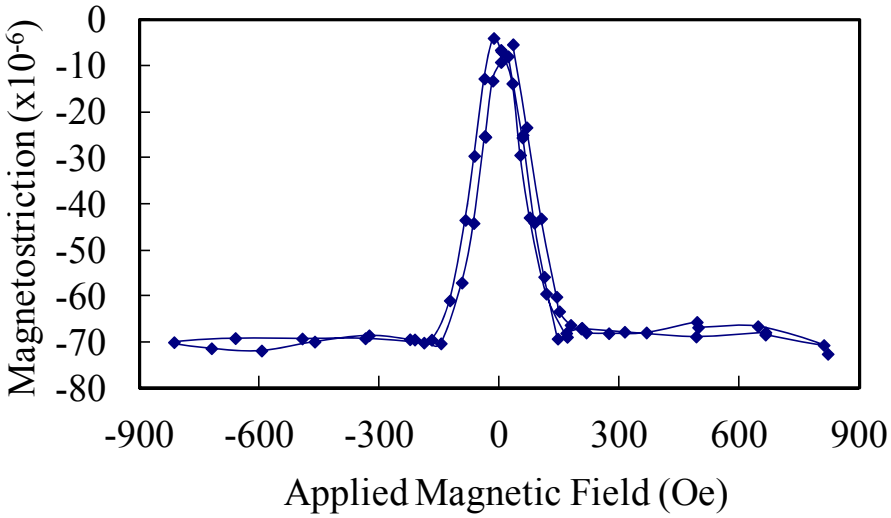

(a)

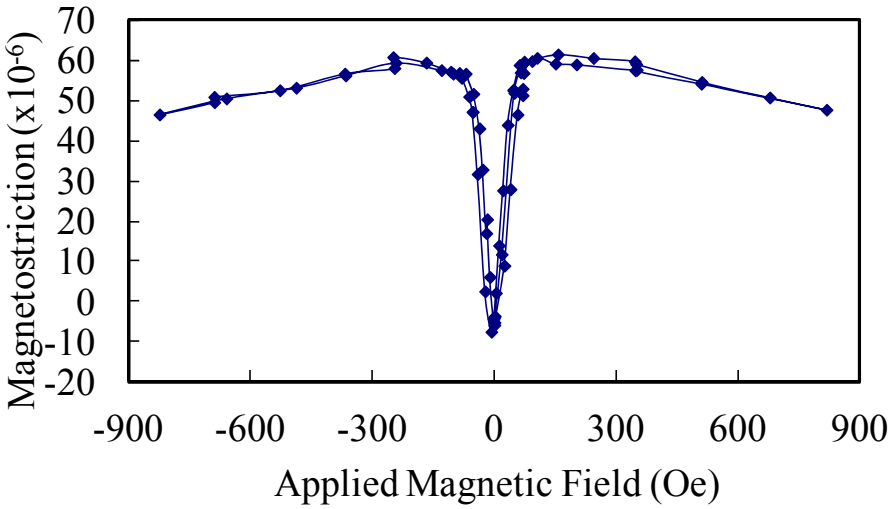

(b)

Figure 4.42 Applied magnetic field vs. magnetostriction in a [001]-oriented Fe-20 at.% Mo single crystal in after annealing treatment; (a) applied field parallel to [001] direction and (b) applied magnetic field parallel to [010] direction. Strain measured along [001] direction.

Table 4.4

Magnetostriction measured for various [001]-oriented Fe-Mo single crystals in the as-grown and annealed condition

At.% Mo	$(3/2)\ \lambda_{100}$ Magnetostriction ($x10^{-6}$)	
	As-grown	After Annealing
5	112	112
10	108	137
20	53	110

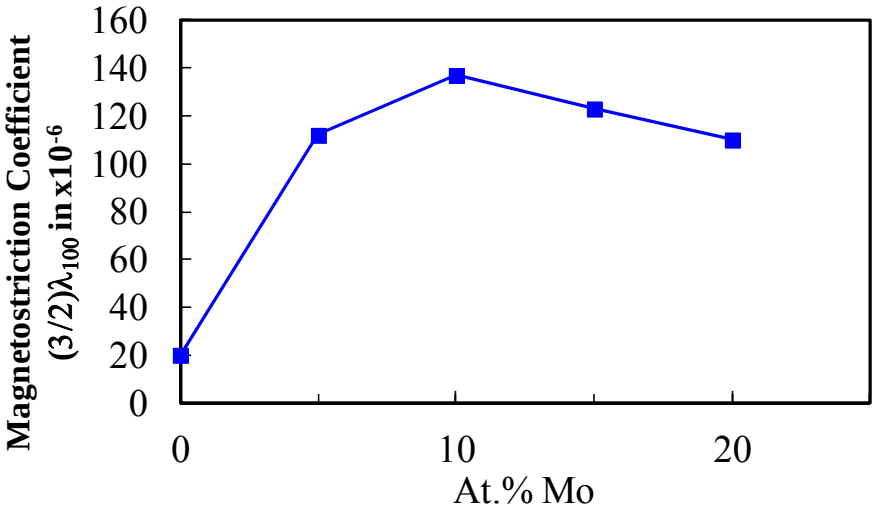

*Fe-15 at.% Mo Source data: Thuanboon [11].

Figure 4.43 (3/2) λ_{100} for Fe-Mo alloy single crystals as a function of Mo content.

4.2.3.2 λ_{111} Measurement

As mentioned in the Chapter 2 Section 2.2, the λ_{100} and λ_{111} are material and its structure dependent constants and are used to obtain magnetostriction in various crystal directions and in polycrystalline materials. This section presents results from λ_{111} constant measurements in Fe-Mo alloys examined in this study. Magnetostriction measurements were made in both the as-grown condition and after annealing in the α-phase region for two hours as shown in Chapter 3 Table 3.1.

The λ_{111} measurement in Fe-5 at.% Mo was made by attaching strain gage on the [211]-oriented face (Figure 3.7). Figure 4.44a and 4.44b show magnetostrictive strains $\lambda_{parallel}$ and $\lambda_{perpendicular}$ along [111] direction versus applied magnetic field curves with magnetic field applied parallel to [111] and parallel to $[1\bar{1}0]$ directions respectively. The ($\lambda_{parallel}$ - $\lambda_{perpendicular}$) gives the (3/2) λ_{111} for the as-grown sample. The (3/2) λ_{100} obtained for Fe-5 at.% Mo in this condition was -23 x 10^{-6}. The Fe-5 at.% Mo sample was then annealed at 1150 °C for 2 h and the magnetostriction measurements were carried out after this annealing step. Figure 4.45a and 4.45b show magnetostrictive strains $\lambda_{parallel}$ and $\lambda_{perpendicular}$ along [111] direction versus applied magnetic field curves with magnetic field applied parallel to [111] and parallel to $[1\bar{1}0]$ directions respectively. The (3/2) λ_{111} obtained after the annealing for Fe-5 at.% Mo was -30 x10^{-6}.

In the case of Fe-10 at.% Mo alloy single crystals, λ_{111} measurement was made by attaching the strain gage on the [220]-oriented face (Figure 3.8). The $\lambda_{parallel}$ measurement was made by applying the magnetic field parallel along [111] direction and $\lambda_{perpendicular}$ measurement was made by applying the magnetic field parallel to $[1\bar{2}1]$

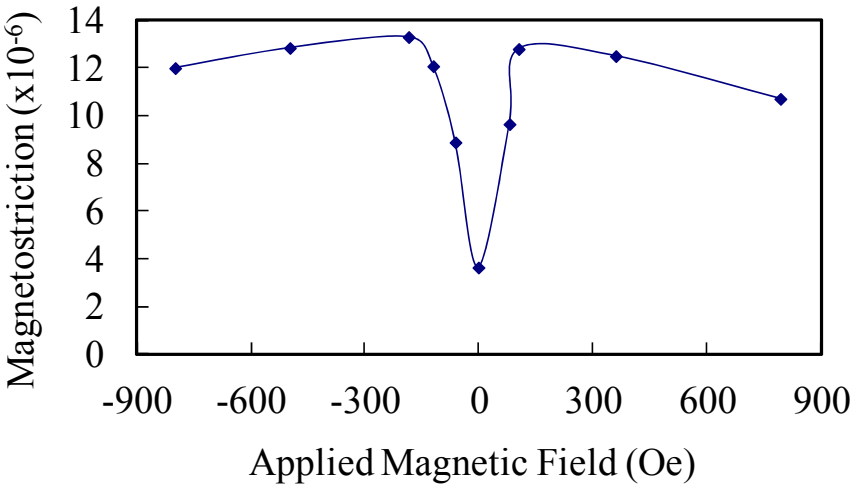

(a)

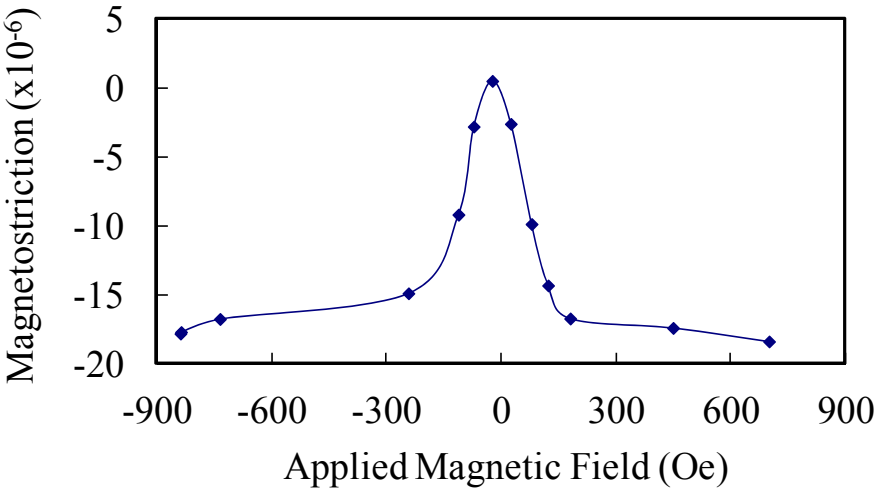

(b)

Figure 4.44 Applied magnetic field vs. magnetostriction in a [211]-oriented Fe-5 at.% Mo single crystal in as-grown condition; (a) applied field parallel to [111] direction and (b) applied magnetic field parallel to $[1\bar{1}0]$ direction. Strain measured along [111] direction.

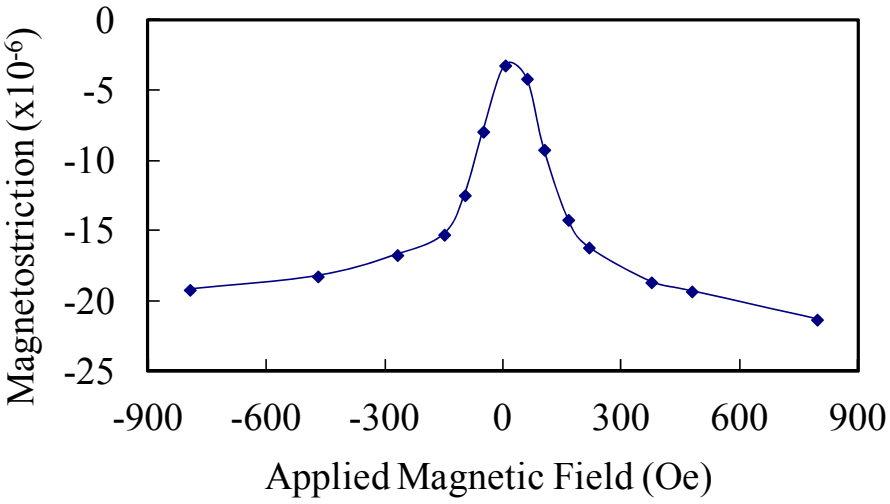

(a)

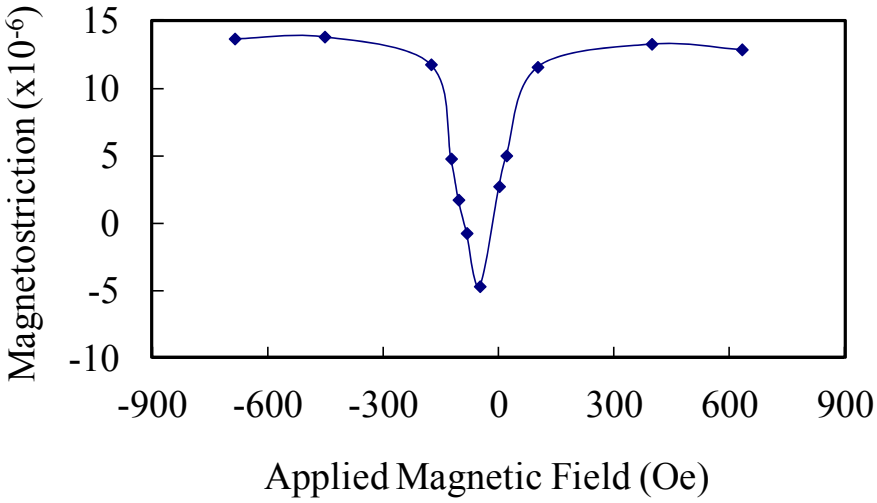

(b)

Figure 4.45 Applied magnetic field vs. magnetostriction in a [211]-oriented Fe-5 at.% Mo single crystal after annealing treatment; (a) applied field parallel to [111] direction and (b) applied magnetic field parallel to $[1\bar{1}0]$ direction. Strain measured along [111] direction.

direction. The ($\lambda_{parallel}$ - $\lambda_{perpendicular}$) gives the (3/2) λ_{111} for the as-grown sample. The (3/2) λ_{111} obtained for Fe-10 at.% Mo in this condition was -31 x 10^{-6}. The Fe-10 at.% Mo alloy sample was then annealed at 1200 °C for 2 h and the magnetostriction measurements were carried out after this annealing step. The (3/2) λ_{111} obtained after the annealing step for Fe-10 at.% Mo was -18 x10^{-6}.

The λ_{111} measurement for Fe-20 at.% Mo sample was made in a way that is similar to the measurement in the Fe-5 at.% Mo alloy single crystal. The strain gage was attached on the [211]-oriented face (Figure 3.7). The $\lambda_{parallel}$ measurement was made by applying magnetic field parallel along [111] direction and $\lambda_{perpendicular}$ measurement was made by applying magnetic field parallel to $[1\bar{1}0]$ direction. The ($\lambda_{parallel}$ - $\lambda_{perpendicular}$) gives the (3/2) λ_{111} for the as-grown sample. The (3/2) λ_{111} obtained for Fe-20 at.% Mo in this condition was -16 x 10^{-6}. The Fe-20 at.% Mo sample was then annealed at 1400 °C for 2 h and the magnetostriction measurements were carried out after this annealing step. The (3/2) λ_{111} obtained for Fe-20 at.% Mo in this condition was -52 x 10^{-6}.

Table 4.5 shows a summary of λ_{111} values obtained for Fe-Mo alloys. Figure 4.46 shows the λ_{111} values obtained for Fe-Mo alloys after annealing. The λ_{111} becomes more positive with increase in Mo content till Fe-10 at.% Mo and then decreases.

4.2.4 Magnetization Measurement

Figure 4.47-4.49 show the magnetization curves of as-cast Fe-Mo alloys obtained using the vibrating sample magnetometer. The measured saturation magnetization values for Fe-5 at.% Mo, Fe-10 at.% Mo and Fe-20 at.% Mo samples are

Table 4.5

Summary (3/2) λ_{111} measured in Fe-Mo alloys

At.% Mo	(3/2) λ_{111} Magnetostriction ($x10^{-6}$)	
	As-grown	After Annealing
5	-23	-30
10	-31	-18
20	-16	-52

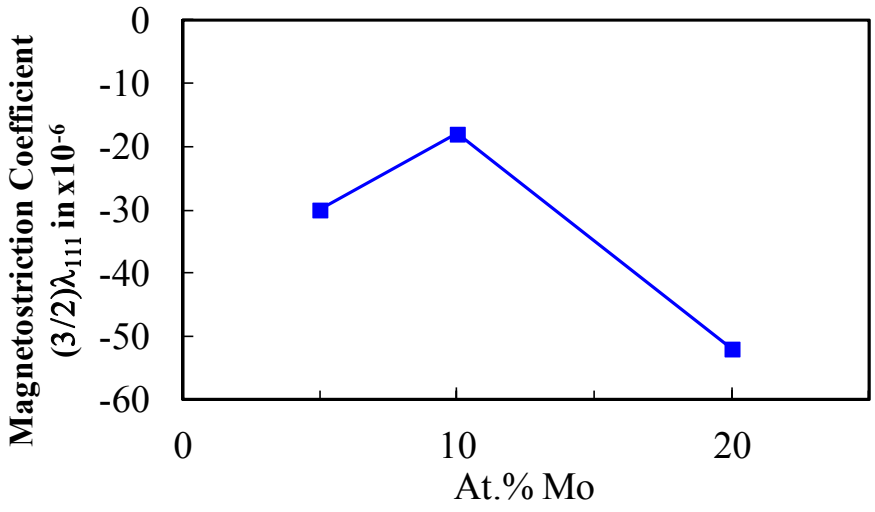

Figure 4.46 (3/2) λ_{111} for Fe-Mo alloy single crystals as a function of Mo content.

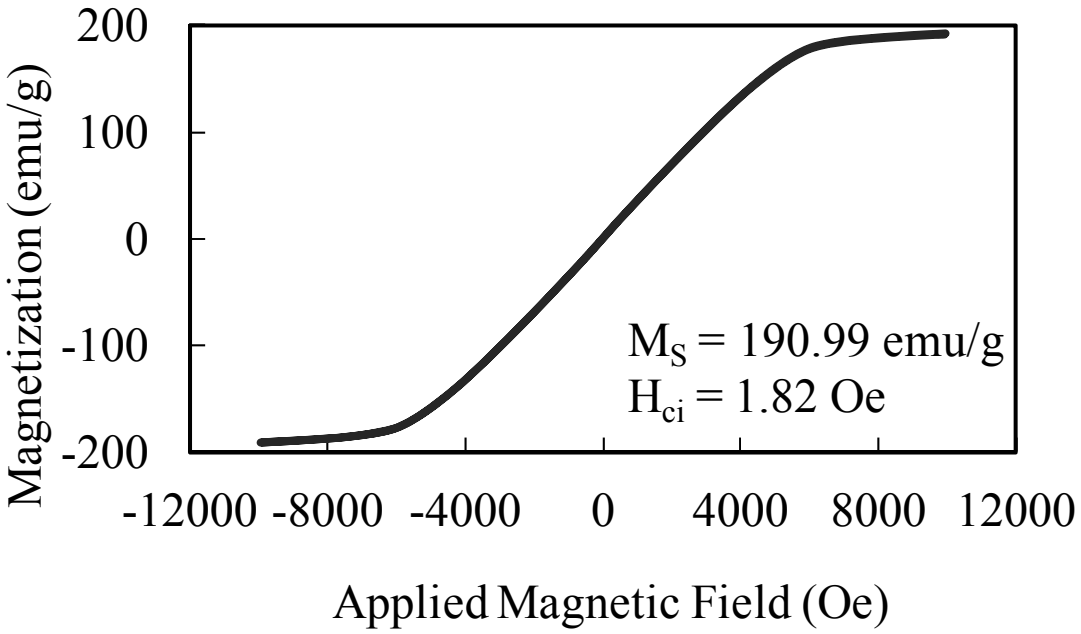

Figure 4.47 Magnetization curve for Fe-5 at.% Mo as-cast sample.

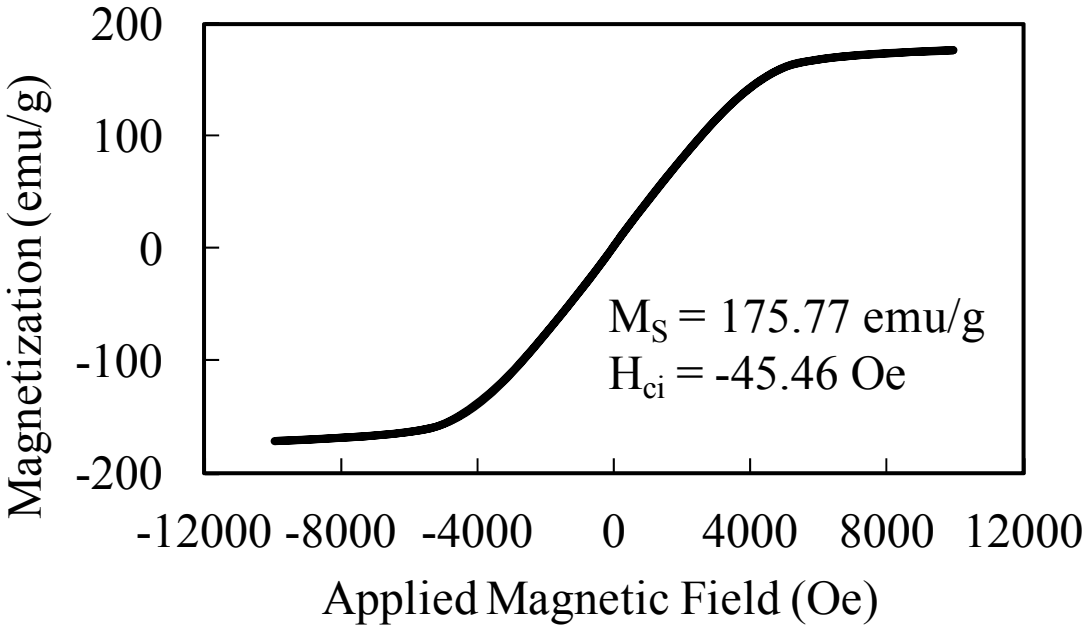

Figure 4.48 Magnetization curve for Fe-10 at.% Mo as-cast sample.

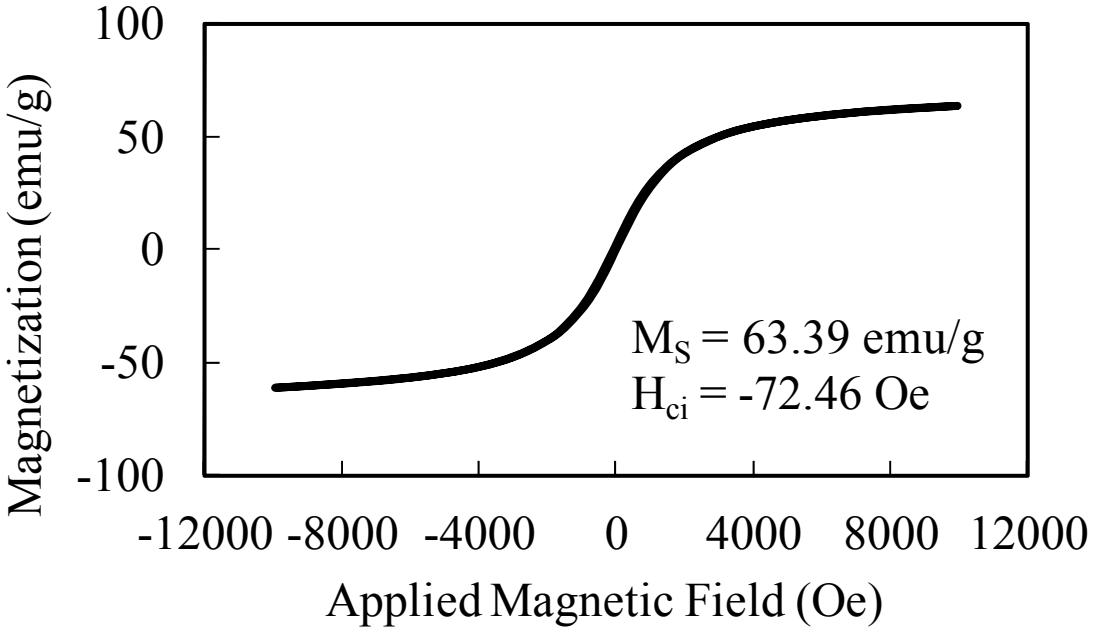

Figure 4.49 Magnetization curve for Fe-20 at.% Mo as-cast sample.

shown in Table 4.6. As the amount of Mo increases in these alloys, saturation magnetization decreases. This is attributed to decrease in the ferromagnetic content in the alloy. At high Mo contents, magnetization drops rapidly and this is indicative of the presence of increasing amounts of nonmagnetic second phase in the alloy [1, 22-23].

Table 4.6

Magnetization measured in as-cast samples of Fe-Mo alloys

At.% Mo	Magnetization (emu/g)
5	191
10	176
15	163
20	63

*Fe-15 at.% Mo Source data: Thuanboon [11]

CHAPTER 5

CONCLUSIONS

Single crystals of Fe-20 at.% Ga were grown using Vertical Bridgman growth technique. Single crystal samples of [001] and [126] orientation were prepared. Two different dislocation array configurations were introduced through controlled deformation in [100] and [126] directions of these oriented single crystal samples. Magnetostriction measurements were made in as-grown condition, after annealing and after deformation.

Magnetostriction measurements show a large decrease in magnetostriction after even a slight deformation with only a single slip system operative as in the case of [126]-oriented sample deformation. Magnetostriction values showed a much lower decrease even with large deformation for the case of [001]-oriented crystal deformation, where eight different slip systems were operative and the strain distributions are symmetric. TEM images also confirm that during the deformation of a [001]-oriented sample multiple slip systems were operative and in the case of [126]-oriented deformed sample a single slip system was operative. No second phase regions were observed in the TEM images but the possible presence of nanoscale coherent second phase regions could not be ascertained due to limitations on resolution during the examination of this strong ferromagnetic sample. From this work it is clear that besides dislocation density,

the nature of strain modulation introduced by the dislocation arrays has a strong influence on the magnetostrictive behavior of magnetostrictive alloys. This fundamental understanding of the role of defects on the magnetostrictive behavior in Fe-based alloys is a major contribution to the field and will be important in the design of low-cost rare-earth free alloys having combination of very good magnetostrctive and mechanical properties.

Single crystals of Fe-5 at.% Mo, Fe-10 at.% Mo and Fe-20 at.% Mo were prepared using the vertical Bridgman growth technique. Single crystal samples having [001] orientation were prepared. As the solubility of Mo in Fe is very low at room temperature (<3 at.%), abundant second phases are expected in the higher Mo content alloys. Magnetostriction values were measured in the [001]-oriented samples in the as-grown condition and after annealing. These measurements show that there is a large increase in magnetostriction of Fe after Mo addition.

Magnetostriction increases till 10 at.% Mo additions and then decreases. The (3/2) λ_{100} measured in Fe-10 at.% is 137 x 10^{-6} and this is the highest reported value for a Fe-Mo alloy single crystals examined until this date. The decrease in magnetostriction after 10 at.% Mo is likely due to the presence of the second phase in higher Mo content alloys. XRD data suggests the presence of a second phase in the Fe-Mo alloys. High resolution TEM analysis is needed to quantify the amount and type of the second phases present in these alloys. The lowering of magnetostriction at higher amount Mo content in Fe-Mo alloys suggest that strain generated due to the second phase also has a large impact on the magnetostriction of magnetostrictive alloys.

The (3/2) λ_{111} measurements in Fe-5 at.% Mo, Fe-10 at.% Mo and Fe-20 at.% Mo single crystals were made. Measurement after annealing shows that λ_{111} value becomes more positive in Fe-10 at.% Mo as compared to Fe-5at.% Mo and then at Fe-20 at.% Mo it goes more negative. This behavior is similar to the variation of λ_{100} values in these alloys. The λ_{111} values of Fe-5 at.% Mo, Fe-10 at.% Mo and Fe-20 at.% Mo alloy single crystals obtained here are the first reported data in this alloy system.

Saturation magnetization values of Fe-5 at.% Mo, Fe-10 at.% Mo and Fe-20 at.% Mo samples were measured using as-cast polycrystalline samples. The measured data show that as the amount of Mo increases in the alloy magnetization reduces and there is a drastic drop in magnetization in Fe-20 at.% Mo sample. This also suggests that large amount of nonmagnetic second phase was present in the alloy.

REFERENCES

1. B. D. Cullity, *Introduction to Magnetic Materials*, 2nd ed, Wiley-IEEE Press, Hoboken/Piscataway, NJ, 2009.

2. S. Guruswamy, N. Srisukhumbowornchai, A.E. Clark, J.B. Restorff , and M. Wun-Fogle, "Strong, ductile, and low field magnetostrictive alloy based on Fe-Ga," *Scripta Mater.*, vol. 43, no. 3, pp. 239-244, 2000.

3. N. Srisukhumbowornchai and S. Guruswamy, "Large magnetostriction in directionally solidified FeGa and FeGaAl alloys," *J. Appl. Phys.*, vol. 90, pp. 5680-5688, 2001.

4. N. Srisukhumbowornchai and S. Guruswamy, "Influence of ordering on the magnetostriction of Fe–27.5 at.% Ga alloys," *J. Appl. Phys.*, vol. 92, pp. 5371-5379, 2002.

5. S. Guruswamy, T. V. Jayaraman, R. P. Corso. Garside, and S. Thuanboon, "Short range ordering and magnetostriction in Fe–Ga and other Fe alloy single crystals," *J. Appl. Phys.*, vol. 104, 113919-1-8, 2008.

6. A. E. Clark, M Wun Fogle, J B Restorff, T. A Lagrasso, J R Cullen, "Effect of Quenching on the Magnetostriction of $Fe_{1-x}Ga_x(0.13 < x < 0.21)$," *IEEE Transactions on Magnetics*, vol. 37, pp. 2678-2680, 2001.

7. T. A. Lograsso, A. R. Ross, D. L. Schlagel, A. E. Clark, M. Wun-Fogle, "Structural transformations in quenched Fe–Ga alloys," *J. Alloys and Compounds*, vol. 350, pp. 95-101, 2003.

8. S. Bhattacharya, J.R. Jinschek, A. Khachaturyan, H. Cao, J.F. Li, and D. Viehland, "Observation of nano-dispersed DO_3 phase nanostructures in highly magnetostrictive Fe-19%Ga Galfenol alloys," *Phys. Rev. B*, vol. 77, 104107-1-6, 2008.

9. T.V. Jayaraman, R.P. Corson, and S.Guruswamy, "Ordering, magnetostriction, and elastic properties in Fe-27.5 at.% Ga alloy single crystals," *J. Appl. Phys*., vol. 102, 053905-1-7, 2007.

10. S. Thuanboon, G. Garside, and S. Guruswamy, "Large low-field magnetostriction in Fe–W and Fe–Mo alloy single crystals," *J. Appl. Phys.*, vol. 104, 013912-1-8, 2008.

11. S. Thuanboon, "Magnetic, Magnetostrictive and Elastic Behaviors of Fe-Binary Alloys", Ph.D. Dissertation, University of Utah, Salt Lake City, UT, 2008.

12. G. Garside, "Probing Local Atomic Structure of Magnetostrictive Iron-Based Single Crystals," Ph.D. Dissertation, University of Utah, Salt Lake City, UT, 2010.

13. G. Garside, C. Ren, B. Saha, M. Ramanathan, and S. Guruswamy, "Magnetostrictive Behavior of Fe-W Alloy Single Crystals," *TMS Annual Meeting, Symposium: Magnetic Materials for Energy Applications,* San Diego, CA, 2011.

14. A.E.Clark, J.B. Restorff, M. Wun-Fogle, K.B. Hathaway, T.A. Lograsso, M. Huang, E. Summers, "Magnetostriction of ternary Fe-Ga-X (X=C,V,Cr,Mn,Co,Rh) alloys," *J. Appl. Phys.* , vol. 101, 09C507, 2007.

15. J.B. Restorff, M. Wun-Fogle, A.E. Clark, T.A. Lograsso, A.R. Ross, D.L. Schlagel, "Magnetostriction of ternary Fe-Ga-X alloys (X=Ni, Mo, Sn, Al)," *J. Appl. Phys.*, vol. 91, no. 10, pp. 8825-8827, 2002.

16. Y. Zhou, B.W. Wang, S.Y. Li, Z.H. Wang, W.M. Huang, S.Y. Cao, W.P. Huang, "The magnetostriction of Fe-(18-x) at% Ga-x at% Al ($3 \leq x \leq 13.5$) alloys," *Journal of Magnetism and Magnetic Materials*, vol. 322, pp. 2104–2107, 2010.

17. N. Srisukhumbowornchai, "Development of Highly Magnetostrictive Fe-Ga and Fe-Ga-Al Alloys", Ph.D. Dissertation, University of Utah, Salt Lake City, UT, 2001.

18. J. P. Hirth, *Theory of Dislocations*, John Wiley, NY, 1982.

19. M. Rhee, J.S. Stolken, V.V. Bulatov, T.D. Rubia, H.M. Zbib, and J.P. Hirth, "Dislocation stress fields for dynamic codes using anisotropic elasticity: Methodology and analysis," *Mat. Sci. and Eng.*, vol. A309, no. 10, pp. 288-293, 2001.

20. P. Mungsantisuk, "Magnetostriction and Texture Development in Binary and Ternary FeGa-Based Alloys", Ph.D. Dissertation, University of Utah, Salt Lake City, UT, 2005.

21. R.P. Corson, "Processing and Magnetostriction Studies in Binary Alloys", Ph.D. Dissertation, University of Utah, Salt Lake City, UT, 2005.

22. L. J. Dykstra, *Nonferromagnetic Precipitate in a Ferromagnetic Matrix*, Magnetism and Metallurgy 2, edited by A. E. Berkowitz and E. Kneller, Academic NY, 1969.

23. S. Mishra and P. A. Beck, *Atomic Order-Disorder Information From Magnetic Data,* Int. Symp. on Order-Disorder Transform in Alloys, Tuebingen, W Ger many, 1974.

24. R.C. O'Handley, *Modern Magnetic Materials*, Wiley, NY, 2000.

25. D Hull and D J Bacon, *Introduction to Dislocations*, Pergamon Press, Oxford, 1984.

26. G. E. Dieter, *Mechanical Metallurgy*, McGrew-Hill Book Company, NY, 1988.

27. J. A. Matthews, *Acoustic Emission*, Gordon and Breach Science Publishers, NY, 1983.

28. *Acoustic Emission*, Symposium presented at the December committee week, American Society for Testing and Materials, Bal Harbor, FL, 1971.

29. F. R. N. Nabarro, *Theory of Crystal Dislocation*, Clarendon Press, Oxford, 1967.

30. A. Clark and K. Halhway, "*Physics of Giant Magnetostriction*", *Handbook of Giant Magnetostrictive Materials*, G. Engdahl, Ed., Academic Press, San Diego, CA, 2000.

31. E.Tremolet, *Magnetostriction Theory and Application of Magnetoelasticity*, CRC Press, Boca Raton, FL, 1993.

32. Z.N. Bolycheva, M.M. Borodkina, and V.L. Sandomirskaya, "Texture and magnetic properties of Fe-Al magnetostriction alloys," *Fiz. Metal. Metalloid,* vol. 19, p. 152, 1965.

33. R. C. Hall, "Magnetostriction of aluminum-iron single crystals in region of 6 to 30 atomic percent aluminum," *J. Appl. Phys.*, vol. 28, p. 707, 1957.

34. J. Emsley, *The Elements*, 2nd ed., Clarendon Press, Oxford, UK, 1991.

35. ASM Hand Book, *Alloy Phase Diagrams*, Vol. 3, ASM International, 1992.

36. A. E. Clark, J B Restorff, M Wun Fogle, T. A Lagrasso, D. L. Schlagel, "Magnetostrictive Properties of Body-Centered Cubic Fe-Ga and Fe-Ga-Al Alloys," *IEEE Transactions on Magnetics*, vol. 36, no. 5, pp. 3238-3240, 2000.

37. J. R. Cullen, A. E. Clark, M. Wun-Fogle, J. B. Restorff, T. A. Lograsso, "Magnetoelasticity of Fe–Ga and Fe–Al alloys," *Journal of Magnetism and Magnetic Materials*, vol. 226-230, pt. 1, pp. 948-949 , 2001.

38. G.D Liu, X.F. Dai; Z.H. Liu, J.L. Chen and, G.H. Wu, "Structure, magnetostriction, and magnetic properties of melt-spun Fe-Ga alloys," *J. Appl. Phys.*, vol. 99, p. 093904-1-5, 2001.

39. S. Guruswamy, P. Mungsantisuk, D. Barker, "Deformation behavior and texture development during the thermomechanical processing of Fe-15 At.% Ga alloys containing NbC," *MPMD Sixth Global Innovations Proceedings - Trends in Materials and Manufacturing Technologies for Transportation Industries and Powder Metall. Research and Development in the Transportation Industry*, TMS Annual Meeting, San Francisco, CA, 2005.

40. R. A. Kellogg, A.M. Russell, T.A. Lograsso, A.B. Flatau, A.E. Clark and M. Wun-Fogle, "Tensile properties of magnetostrictive iron–gallium alloys," *Acta Materialia*, vol. 52, pp. 5043-5050, 2004.

41. X. Zhao, N. Mellors, D.G. Lord, "Magnetomechanical performance of directionally solidified Fe-Ga alloys," *J. Appl. Phys.*, vol. 101, 09C513, 2007.

42. R. A. Kellogg, A.B. Flatau, A.E. Clark, M. Wun-Fogle and T.A. Lograsso, "Texture and grain morphology dependencies of saturation magnetostriction in rolled polycrystalline $Fe_{83}Ga_{17}$," *J. Appl. Phys.*, vol. 93(10), pp. 8495-8497, 2003.

43. J. Atulasimha, A.B. Flatau, "Experimental actuation and sensing behavior of single-crystal iron-gallium alloys," *Journal of Intelligent Material Systems and Structures*, vol. 19, pp. 1371-1381, 2008.

44. S. Datta, J. Atulasimha, A.B. Flatau, "Figures of merit of magnetostrictive single crystal iron–gallium alloys for actuator and sensor applications," *Journal of Magnetism and Magnetic Materials*, vol. 321, pp. 4017-4031, 2009.

45. Q. Xing, Y. Du, R.J. McQueeney, T.A. Lograsso, "Structural investigations of Fe–Ga alloys: Phase relations and magnetostrictive behavior," *Acta Materialia*, vol. 56, v 4536-4546, 2008).

46. R. C. Hall, "Single-Crystal Magnetic Anisotropy and Magnetostriction Studies in Iron-Base Alloys," *J. Appl. Phys.*, vol. 31, p.1037, 1960.

47. B. D. Cullity and S. R. Stock, *Elements of X-Ray Diffraction,* Prentice Hall, Inc., Upper Saddle River, NJ, 2001.

48. L.V. Azaroff, *Elements of X-Ray Crystallography*, McGrew Hill, NY, 1968.

49. C. Suryanarayana and M. G. Norton, *X-Ray Diffraction: A Practical Approach,* Plenum Press, NY, 1998.

50. R. S. Rai, S. Guruswamy, K. T. Faber, and J. P. Hirth, "Defects and mechanical properties: Dislocation structures in in-doped and undoped GaAs deformed at 700-1100C," *Philosophical Magazine A*, vol. 60, no. 3, pp. 339-353, 1989.